論文 / 著書情報
Article / Book Information

題目(和文)	
Title(English)	Ka-Band CMOS Active Phased-Array Transmitters for Power-Efficient Small-Satellite System
著者(和文)	YOUDongwon
Author(English)	Dongwon You
出典(和文)	学位:博士(学術), 学位授与機関:東京工業大学, 報告番号:甲第12585号, 授与年月日:2023年9月22日, 学位の種別:課程博士, 審査員:岡田 健一,白根 篤史,廣川 二郎,德田 崇,伊藤 浩之,藤井 威生
Citation(English)	Degree:Doctor (Academic), Conferring organization: Tokyo Institute of Technology, Report number:甲第12585号, Conferred date:2023/9/22, Degree Type:Course doctor, Examiner:,,,,,
学位種別(和文)	博士論文
Type(English)	Doctoral Thesis

Ka-Band CMOS Active Phased-Array Transmitters for Power-Efficient Small-Satellite System

by

Dongwon You

A Ph. D. dissertation submitted in partial satisfaction of the requirements for the degree of

Electrical and Electronic Engineering

in the

School of Engineering

of

Tokyo Institute of Technology

Supervised by

Prof. Kenichi Okada

Assoc. Prof. Atsushi Shirane

Summer 2023

To my family,

Acknowledgment

Throughout my doctoral studies, I have spent more than five years in the Okada-lab, and this thesis represents the most challenging work I have undertaken during this time. The research process was demanding, requiring extensive time and effort to transform initial ideas into a coherent and rigorous study. Each idea required careful consideration and thorough examination to ensure that any potential issues or problems were addressed. Implementation was also a significant challenge, necessitating numerous verification processes to ensure accuracy and reliability. Through it all, I could not have accomplished this work without the invaluable help and support of my supervisor and lab mates.

Above all, I wish to express my deepest gratitude to Professor Kenichi Okada, my supervisor. I am indebted to him for providing me with the opportunity to explore my career direction and for his unwavering support throughout my studies. Despite his busy schedule, Okada-sensei always made himself available to offer guidance and advice when I faced difficulties. He was always generous with his time and resources, and his unwavering support was the cornerstone of my doctoral journey.

I would also like to express my sincere appreciation to Professor Akira Matsuzawa for his invaluable guidance and support throughout my doctoral study. His insightful comments and constructive criticisms have been instrumental in shaping my research work. I am also grateful for his kind invitation to his house and the opportunity to socialize with everyone, which enriched my experience in Japan beyond the laboratory and provided me with many unforgettable memories. Our conversations have been a source of inspiration, opening up new perspectives and broadening my vision.

I would like to express my sincere gratitude to Professor Atsushi Shirane for his unwavering support throughout my doctoral study. As a supervisor and mentor, he always offered me valuable advice and helped me break free from the cycle of overthinking and unproductive thoughts. His encouragement and support were instrumental in the success of my research. Moreover, Professor Shirane is a role model for me in terms of his work ethic, economic approach, and inspiring leadership. He constantly inspires me to generate innovative ideas and think critically when facing technical challenges. Thank you for being a great supervisor and mentor to me.

I would also like to express my sincere gratitude to the members of the Ph.D. committee, namely Prof. Jiro Hirokawa, Prof. Takashi Tokuda, Prof. Hiroyuki Ito, Prof. Atsushi Shirane, and Prof. Takeo Fujii for taking the time to review and evaluate my dissertation, and for attending my final presentation. Their valuable feedback and suggestions have greatly contributed to improving the quality of my work and inspiring me to further pursue my research interests.

I would also like to express my heartfelt gratitude to the most thoughtful individuals in our laboratory: Hiroyuki Sakai, Yoshino Kasuga, Makiko Tsunashima, Ayumi Okubo, Teruki Someya, and Kiyoshi Yanagisawa. Their support and guidance have been invaluable throughout my time here. Their insightful advice, clear explanations, and timely reminders have greatly assisted me in both my academic and personal pursuits. Thank you all so much for your kindness and generosity.

I would like to express my sincere gratitude to my seniors, Bangan Liu, Zheng Sun, Jian Pang, Yuncheng Zhang, Yun Wang, Rui Wu, and Seungjong Lee. Their invaluable advice has been instrumental in achieving the results presented in this dissertation. Additionally, I am grateful for the time we spent together and the enjoyable moments we shared, which greatly enriched my life in Japan.

I would also like to extend my gratitude to the SATCOM group members: Xi Fu, Zheng Li, Hans Herdian, Chun Wang, Waleed Madany, Ashivir Aviat Fadila, Carrel, Dingxin Xu, Yi Zhang, Chenxin Liu, Wenqian Wang, Michihiro Ide, Abanob Shehata, Minzhe Tang, Xiaolin Wang, Yudai Yamazaki, Jun Sakamaki, Keito Yuasa, Yuan Gao, Sena Kato, Yasuto Narukiyo, Takeshi Nakamura, Rattanan Saengchan, Atsuhiro Kawaguchi, Joshua Alvin, and Muhammad Amar Maruf. Their contributions and support have been invaluable, and I am grateful for their knowledge-sharing and the moments of joy we shared. I wish them all the best in their future endeavors.

I would like to express a special thank you to my non-school colleagues: Minkyuk Sung, Juyeong Kim, Inchan Ju, Sangyeop Lee, Hyun-cheol Park, Junghwan Kim, and Heejae Jeon. When faced with problems that could not be solved with school colleagues, they provided me with fresh perspectives and expanded my field of knowledge. They have been a great source of inspiration, and I am grateful for their friendship.

I also would like to thank everyone who has supported me during my doctoral studies. It has been an unforgettable journey, and I am grateful for the opportunity to pursue my research in such a supportive environment.

Finally, I want to thank my parents and sister. Even though they are all far from me in the distance, I feel warm in my heart.

Abstract

This dissertation represents a significant contribution to the development of a Ka-band CMOS deployable active phased-array TX for the LEO small satellite constellation. To achieve high data throughput, low-cost, and low power consumption in SATCOM using LEO small satellite constellation, the TX design must satisfy these three key requirements.

To address these challenges, this dissertation proposes several novel techniques, including a phased array load tuner for low-power consumption, a dual circular polarization calibration for higher data rate, a low-power single circular polarization coupler, and a new deployable substrate implemented with a hetero-segmented liquid crystal polymer (LCP) substrate to lower launch cost. Moreover, a systematic array design for small satellites is introduced to further reduce the DC power consumption.

Experimental results demonstrate that the proposed techniques successfully achieve the three key requirements for the phased-array TX in the LEO small satellite constellation. Specifically, the phased array load tuner achieved $\times$1.39 power efficiency improvement at a -40° beam angle, while the proposed circular polarization calibration method improved the cross-polarization discrimination (XPD) by 36.3 dB, doubling the data rate with dual circular polarization. The single circular polarization coupler reduced 38.3% of the DC power consumption in signal circular polarization mode compared to conventional single circular polarization generation methods. Additionally, the proposed deployable phased-array TX with hetero-segmented LCP substrate demonstrated deployability and a lightweight form factor of 9.65 g.

Taken together, the results of this dissertation represent a significant step towards realizing LEO small satellites that can provide high data throughput at low cost and low power consumption.

Contents

List of Figures

List of Tables

Chapter 1

Introduction

Terrestrial communications such as WiGigs [9–18], 5^{th} generation cellular communications (5G) [19–35], sensing radars [36–39] is well developed to benefit human beings. Terrestrial networks provide tremendous conveniences, covering all over the globe where human beings can conquer. However, there are limitations that the terrestrial networks cannot overcome: 1) vulnerability to terrestrial disaster, 2) no connection to air, or maritime.

Satellite communication (SATCOM) has been the essential communication infrastructure for various purposes since the emergence of satellite history. Providing various precious services that cannot be delivered with terrestrial networks, SATCOM is conducting irreplaceable roles in our daily life.

- Global positioning services (GPS)
- Satellite broadcast systems
- Earth explorations
- Communication to air, maritime, underprivileged areas
- Communications even when terrestrial disasters attack

Furthermore, the internet of things (IoT) accelerated needs of the massive terminal connectivity. Because the SATCOM system can provide wide coverage areas. This results in an increase in demand for the SATCOM networks. Again, this demand brought out high data throughput handling ability to the SATCOM systems. SATCOM is one of the most important communication resources for human beings in present and the future.

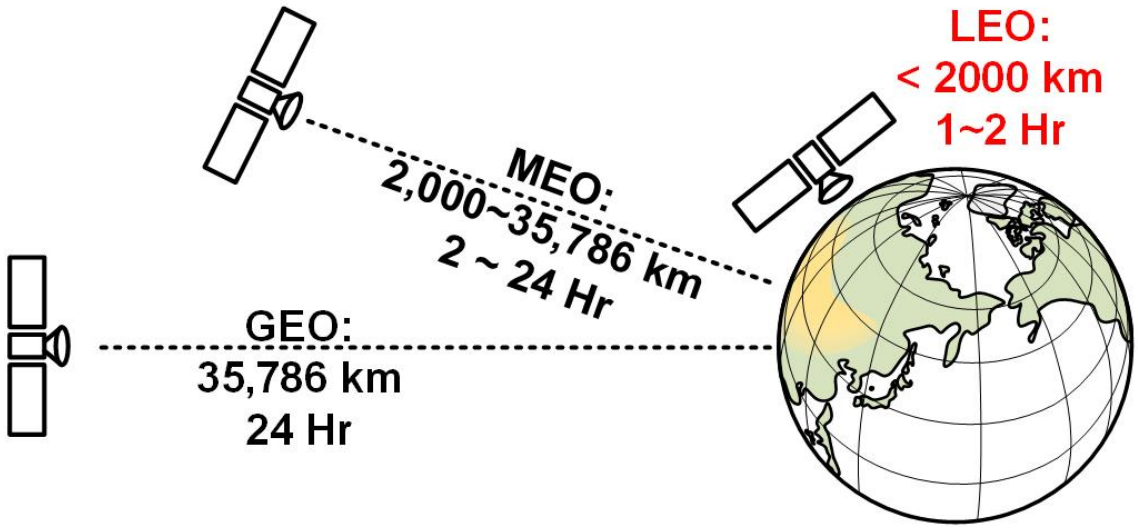

Figure 1.1: Various types of satellite orbit by altitudes: their altitude, and revolution time.

1.1 LEO Small Satellite

SATCOMs can be categorized by different satellite orbits: geostationary-earth orbit (GEO), medium-earth orbit (MEO), and low-earth orbit (LEO) as shown in Figure. **??**.

- **GEO**: Geostationary-earth orbit is 35.786 km high. The satellite revolution period is synchronized to the earth's rotation period. This enables the satellite to see the fixed spot on the earth's surface. This means that ground station antennas are not required to track satellite locations. Because its orbit is far away from the earth, the communication coverage is widest even with a narrow beam-width antenna. However, it suffers from long propagation delays due to the long communication distance.

- **MEO**: Revolution period is around half a day. For the wide coverage, more satellites are required than GEO but fewer than LEO. This orbit is popular for many navigation systems. Propagation delay is more than LEO but shorter than GEO.

- **LEO**: Low-earth orbit has around 500 to 2000 km height. LEO satellites' revolution period is around 1 2 hours. This means that fixed-spot ground stations can communicate with the satellite for a very short time. If wide coverage is required, then a satellite constellation required with a number of satellites. Thanks to the short distance, propagation delay is the shortest among the three types of orbit types.

While the GEO and MEO satellites have been popularly used for decades, the LEO satellites are becoming a prominent SATCOM solution for their low latency, and low

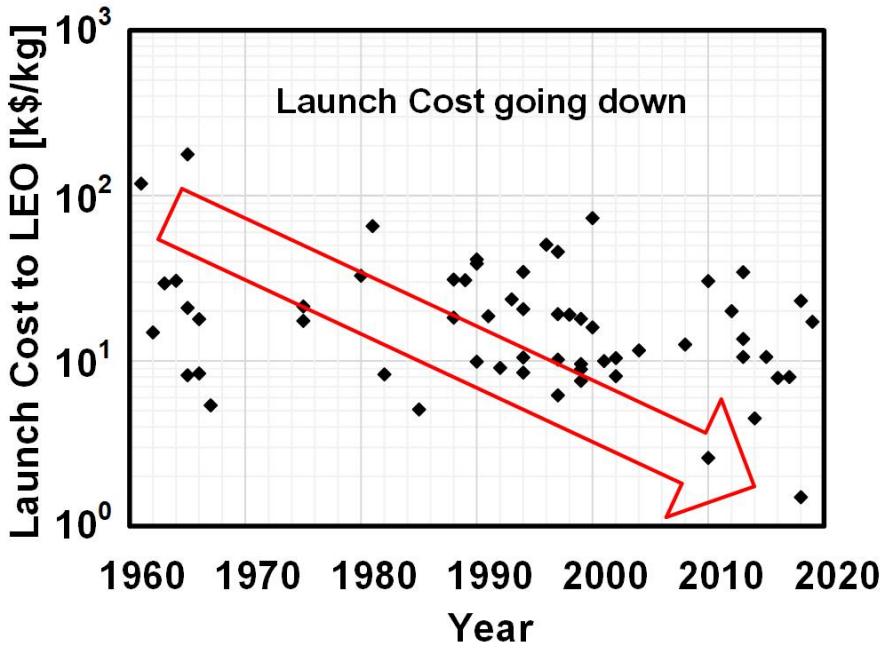

Figure 1.2: Launch cost of the LEO satellites over the satellite history [1].

price. Furthermore, the emergence of the *NewSpace* businesses boosted the drop of the rocket launch cost. In Figure. 1.2, the trend of the rocket launch cost to the LEO for several decades is shown. As shown in Figure. 1.2, the 2020s launch cost per mass is dramatically reduced by around 100 times compared to the 1960s. With the reduced launch cost, many satellites can be launched into space, thus it is possible to build a satellite constellation. By communicating between satellites, the LEO can break through the trade-off between latency and coverage area which comes from orbit altitude. This boosted the LEO satellite system as one most prominent and important SATCOM systems. Especially, the LEO satellite shows its competence in remote sensing such as earth-exploration satellite service (EESS) utilizing low orbit altitude for higher optical cameras, and high data rate and low-latency communication to provide internet service to all the globes.

1.1.1 Earth Exploration Satellite

One most adequate applications for the LEO satellite is the EESS. This is because of the higher optical resolution due to the low altitude of the satellite. As the various types of terrestrial problems such as global warming, earthquake, marine pollution, aerosols, and typhoons as shown in Figure. 1.3 are becoming more and more vicious, the EESS shows its true worth. Utilizing various types of optical observation equipment and their imagery data, human beings can analyze the phenomenon, grasp the symptom, and be

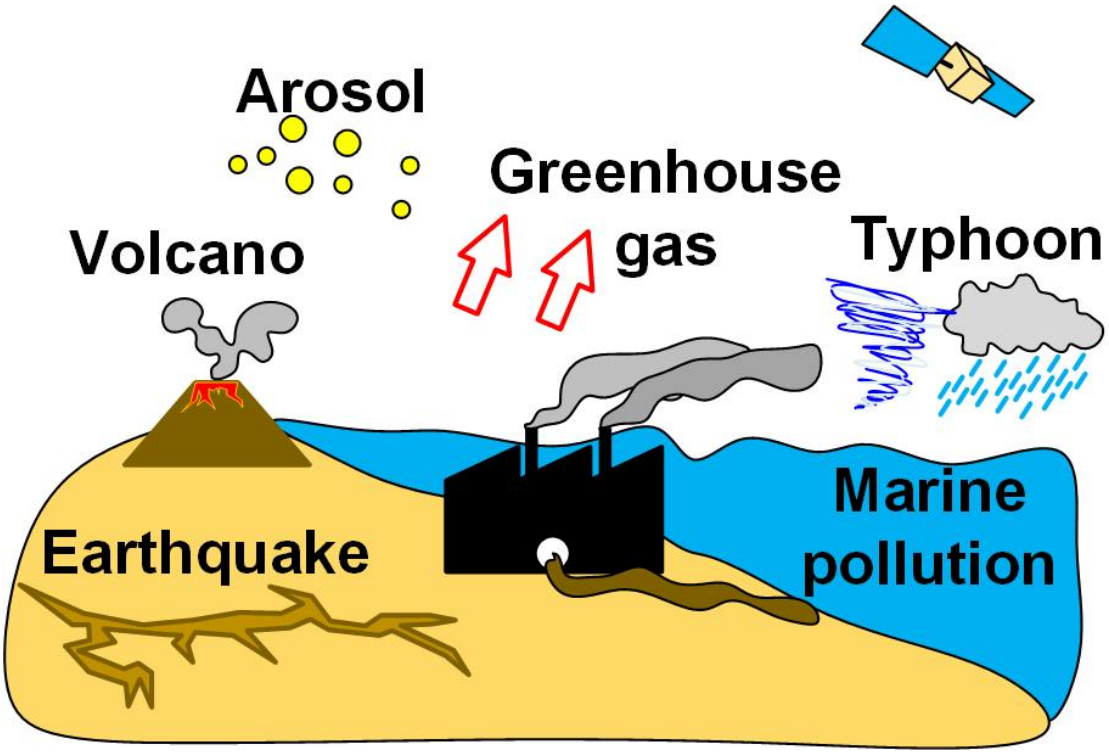

Figure 1.3: Internet of things and its application.

prepared for the problem breaking. For these reasons, the demand for data from the EESS is increasing, making the EESS one of the most important SATCOM applications.

By composing the constellation of the small satellites, the EESS performance incredibly increases. Figure. 1.4 illustrates how the EESS achieves high performance with the satellite constellation. The satellites form orbits by passing through the north pole and south pole which are called polar orbits. Every single polar orbit is called an orbit plane. In each orbit plane, several satellites fly. This constellation composition has several advantages.

- All the areas of the globe can be observed concurrently.
- Abundant data enables predictions much more accurately.
- Only a single ground station can be built for reduced cost because all the satellites pass through the north and south pole.

Because of the above advantages, EESS with the satellite constellation can satisfy the market need, thus many EESS operators are changing their paradigm from a single satellite to satellite constellations.

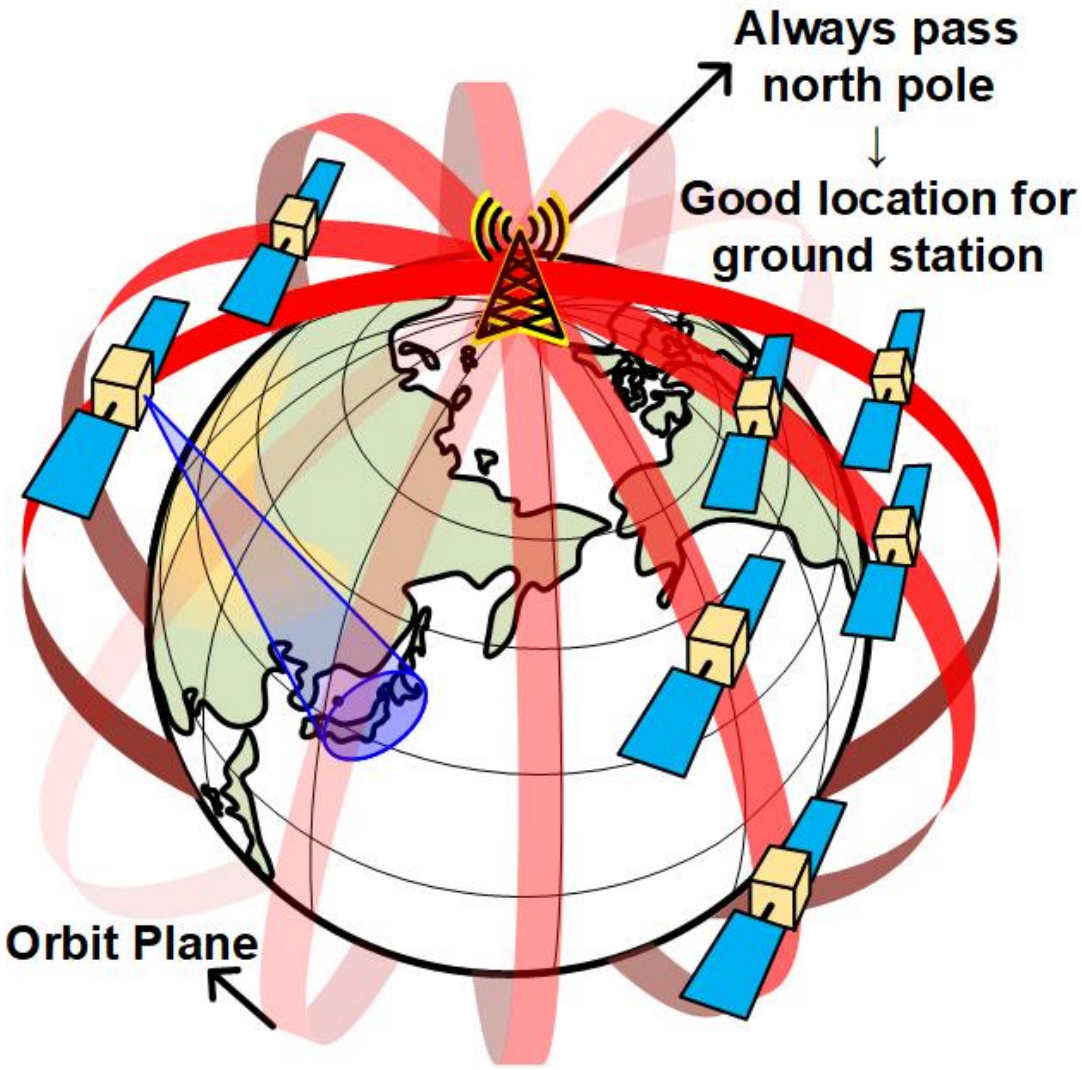

Figure 1.4: LEO satellite constellation build-up for EESS.

1.1.2 High Data Rate SATCOM

Not only the remote sensing applications but also high data rate SATCOM is one prominent application with the LEO small-satellite SATCOM. As the same as the EESS constellation, high data rate SATCOMs also utilize satellite constellations to cover all over the globe. The satellites connect to not only the ground terminals but also adjacent satellites to connect one ground point to another.

While the conventional SATCOM systems have used X-band or K-band, many *NewSpace* enterprises such as SpaceX, Amazon, Telesat, OneWeb, etc are moving to the Ka-band for its wider bandwidth. The wider bandwidth provides a faster data rate by the Shannon-Hartely theorem as depicted in Equation. 1.1

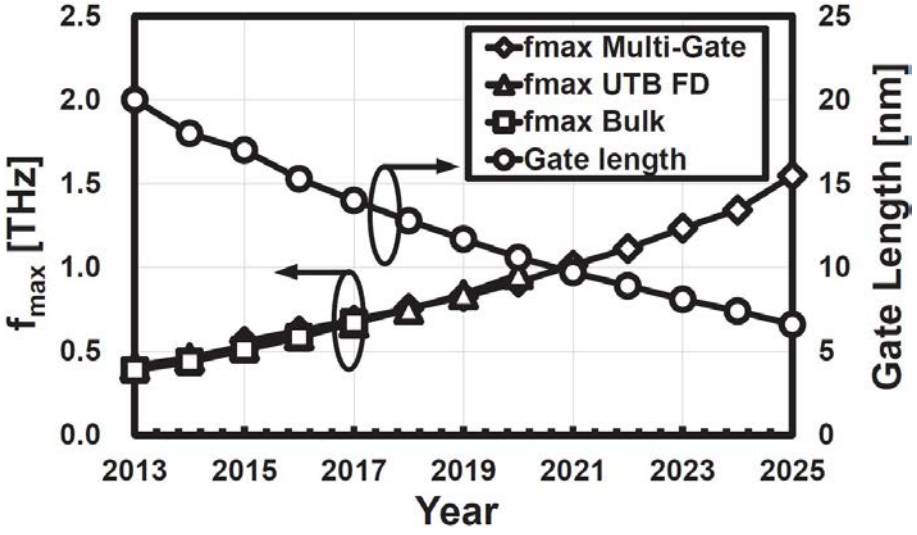

Figure 1.5: Maximum oscillation frequency of the CMOS along with the evolving nodes.

$$C = BW \times \log_2\left(1 + \frac{S}{N}\right) \tag{1.1}$$

where C denotes channel capacity in bits per second, B is the bandwidth, and S/N is the signal-to-noise ratio. Furthermore, because the low altitude of the LEO satellite exhibits low latency, LEO SATCOM became one most important SATCOM solutions.

1.2 CMOS Millimeter-Wave

The fast-evolving CMOS technology has brought numerous benefits to millimeter-wave wireless transmitters (TX), enhancing their capabilities and improving their overall performance. Although CMOS technology is less expensive, compound semiconductor technologies were previously used for mm-wave frequencies due to their ability to handle higher frequencies that CMOS technology could not cover. However such compound semiconductors suffer from high fabrication costs, low integration levels, and additional package costs. As shown in Figure. 1.5, the CMOS technology successfully shifts the paradigm by their reduced nodes [40]. With the highly integrated mm-Wave systems, minimized manufacturing and package costs are realized [41–43]. Furthermore, as elaborated upon in Chapter 2 and discussed in previous sections, the implementation of active phased array and LEO small satellite constellations necessitates a significant number of integrated circuits (ICs), thereby driving up demand for CMOS technology and facilitating mass production. This increase in demand leads to reduced manufacturing costs, highlighting the economic benefits of using CMOS technology for these applications.

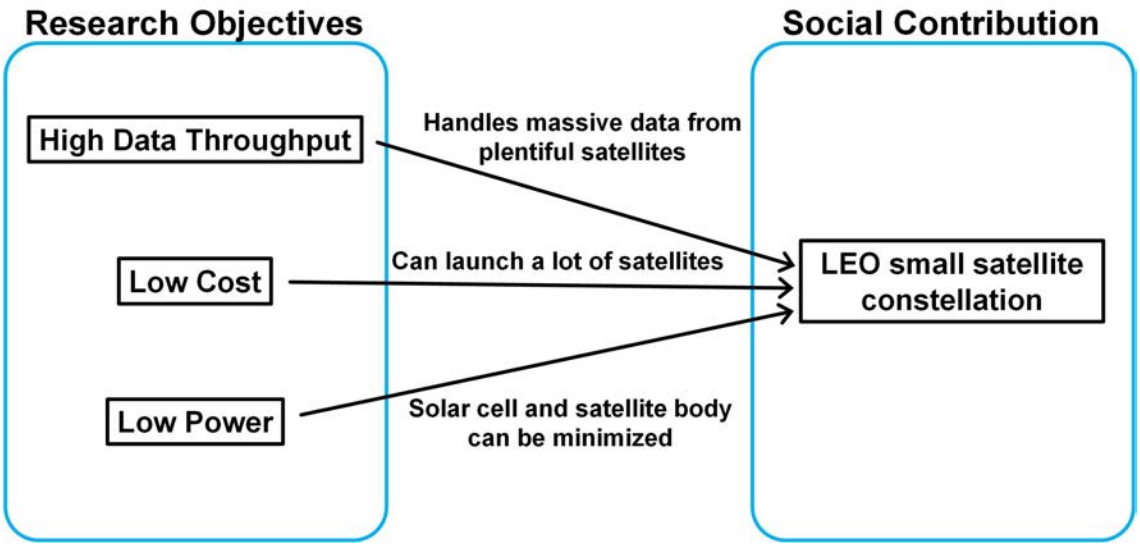

Figure 1.6: Relationship diagram between the research objectives and social contribution.

1.3 Research Objectives and Thesis Overview

The research objective of this thesis is to implement the Ka-band CMOS active phased-array TX for small satellites, targeting low power consumption, high data throughput, and low cost as summarized in Figure. 1.6.

This thesis is organized as shown in Figure. 1.7 and explained as follows.

Chapter. 2 mainly presents the challenges for the LEO small satellite TX implementation. For that, Chapter. 2 summarizes standard TX design challenges and special requirements from the Ka-band CMOS active phased-array TX for LEO small satellite constellation. Then, the research objectives will be revisited.

Chapter. 3 presents how the phased-array TX can be space-efficient. For the space-efficiency, the chapter proposes a new flexible liquid crystal polymer (LCP) substrate structure for the deployable phased-array TX. With the proposed hetero-segmented LCP substrate, The deployable phased-array TX shows excellent space efficiency. The discussion about mechanical deformation calibration of the proposed deployable phased array is presented, as well. Showing the measurement results of the deployable phased-array TX, the chapter supports the idea of the proposed deployable phased-array TX on the hetero-segmented LCP substrate.

Chapter. 4 presents about two main techniques: a power-efficient load tuner for the SATCOM phased-array TX and a novel circular polarization calibration for the data rate doubling. Circuit details on the proposed phased array load tuner and the proposed circular polarization calibration detection are discussed. Not only the circuit details but the principle of the two techniques are also represented in detail. The measurement results

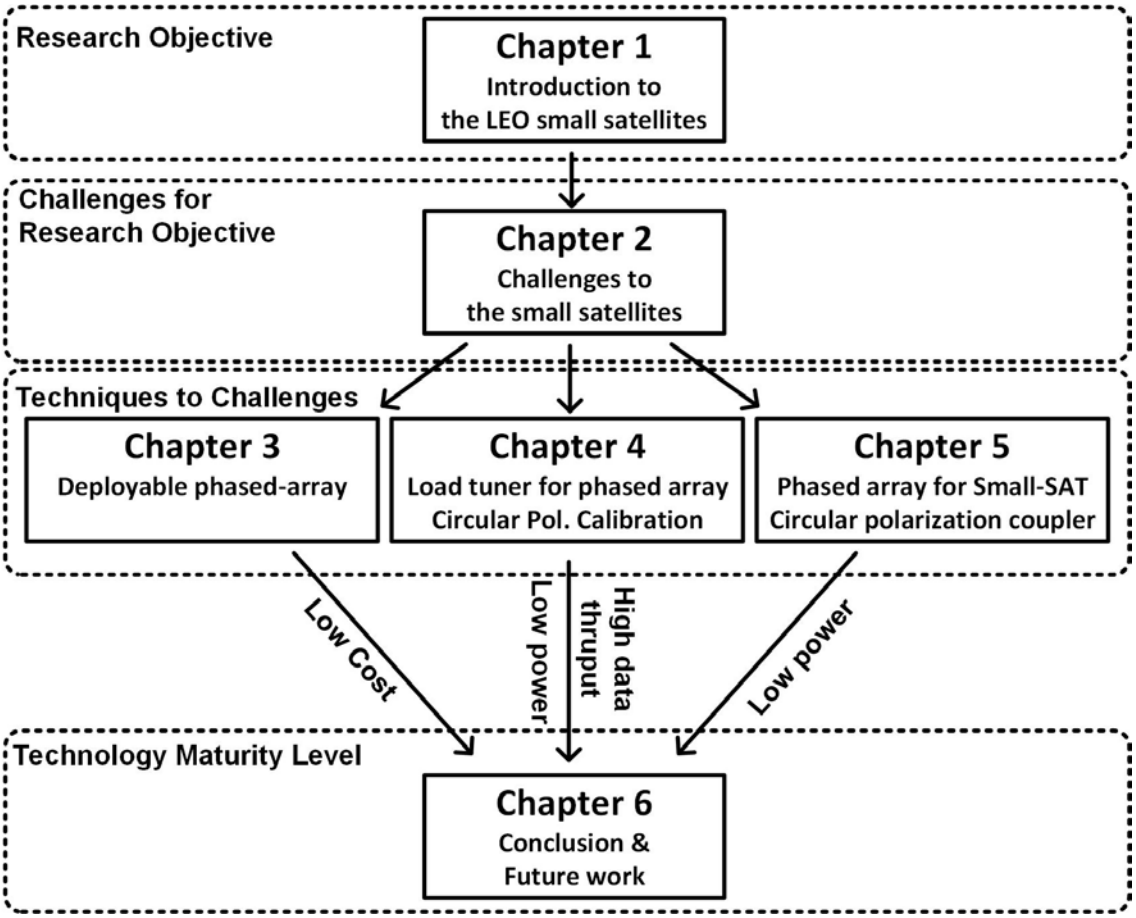

Figure 1.7: The chapter organization and overview of this doctoral thesis.

of the proposed techniques over the air (OTA) well-supports that the idea is critical to the implementation of the LEO small satellite constellation.

Chapter. 5 demonstrates the systematic design methodology about how to make the LEO small satellite power-efficient, and a novel single circular polarization coupler for better power-efficiency. A comparison of the various circular polarization is discussed and why the proposed active quadrature coupler is important is well addressed. Showing the benchmark on effective isotropic radiated power (EIRP) and DC power consumption, the chapter concludes that the proposed techniques are suitable for low-power TX design for LEO small satellite constellation,

Chapter. 6 summarizes the social contribution of the SATCOM using the LEO small satellite constellation, research objectives, and technical solutions to the technical challenges to achieve the research objectives introduced in this thesis.

Chapter 2

Challenges to Phased Array for Small Satellite

2.1 TX Design Considerations

This section discusses design considerations of the standard TX including noise, linearity, the relationship between bandwidth and data rate, digital modulation, and phased array. Although the SATCOM application requires lots of specific requirements in TX design, still standard TX design consideration is significant. Especially, the linearity consideration is a crucial consideration in all the TX designs including terrestrial and non-terrestrial systems. The noise might be less important in TX design, but for the correct TX power level decision, the noise of the RX in the ground station must be considered.

2.1.1 Noise

While the upper limit of a system's performance is determined by linearity, the smallest signal that the system can detect is dictated by noise. Achieving higher resolution in phase and amplitude detection requires lower noise levels compared to the signal itself. In the context of analog-to-digital conversion, the signal-to-noise ratio (SNR) is critical, and this subsection focuses mainly on the noise figure (NF) at the input of the ADC. Several noise performance metrics are commonly used, including noise temperature, input-referred voltage and current noise, and NF or noise factor (F). Among them, NF and F are particularly useful as they are SNR-friendly noise metrics. Thus, NF and F can be defined as follows:

$$F = \frac{SNR_{IN}}{SNR_{OUT}} \tag{2.1}$$

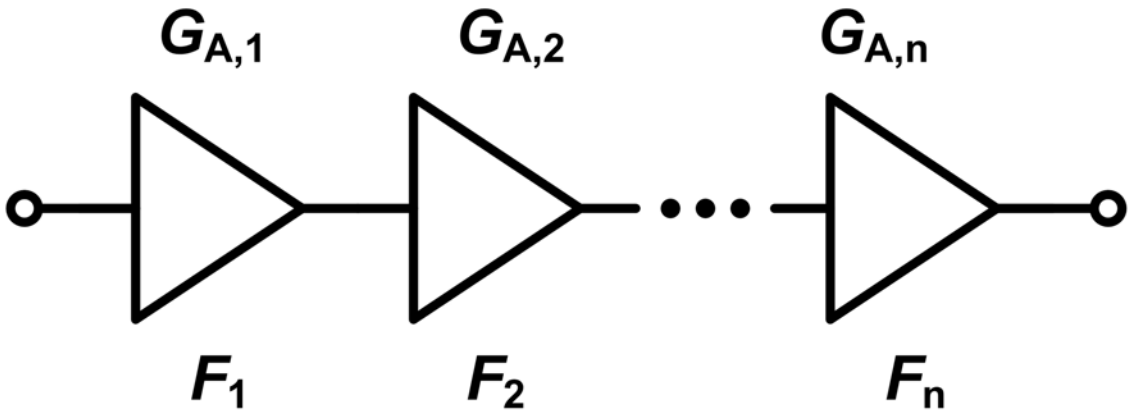

Figure 2.1: Block diagram for cascaded amplifiers with varying gains and IP3s.

$$NF[dB] = 10\log_{10} F \tag{2.2}$$

To ensure systematic design, it is necessary to derive the cascaded NF from the individual blocks' NF and gain in Figure. 2.1, under the condition of matched inter-stage impedances [44]. The expression for cascaded NF is as follows:

$$F_{TOTAL} = 1 + (F_1 - 1) + \frac{F_2 - 1}{G_{A,1}} + \frac{F_3 - 1}{G_{A,1}G_{A,2}} + ... + \frac{F_n - 1}{G_{A,1}G_{A,2}...G_{A,n-1}} \tag{2.3}$$

where, F_k is noise factor of k^{th} amplifier and $G_{A,k}$ is available power gain of k^{th} amplifier.

In SATCOM system design, noise temperature is more important and practical than NF for system noise evaluation. The NF metric is mainly concerned with the signal-to-noise ratio (SNR), while the noise temperature metric is focused on the noise itself. The relationship between NF and noise temperature can be expressed as

$$T = T_{REF}(F - 1), \tag{2.4}$$

where the T_{REF} is the reference temperature of the system. In the room temperature, T_{REF} becomes 290°K.

Because any lossy component has noise including the antenna, antenna feed lines, and active amplifiers, cascaded total noise temperature also must be considered as same as the NF case.

$$T_{TOTAL} = T_1 + \frac{T_2}{G_{A,1}} + \frac{T_3}{G_{A,1}G_{A,2}} + ... + \frac{T_N}{G_{A,1}G_{A,2}...G_{A,N-1}} \tag{2.5}$$

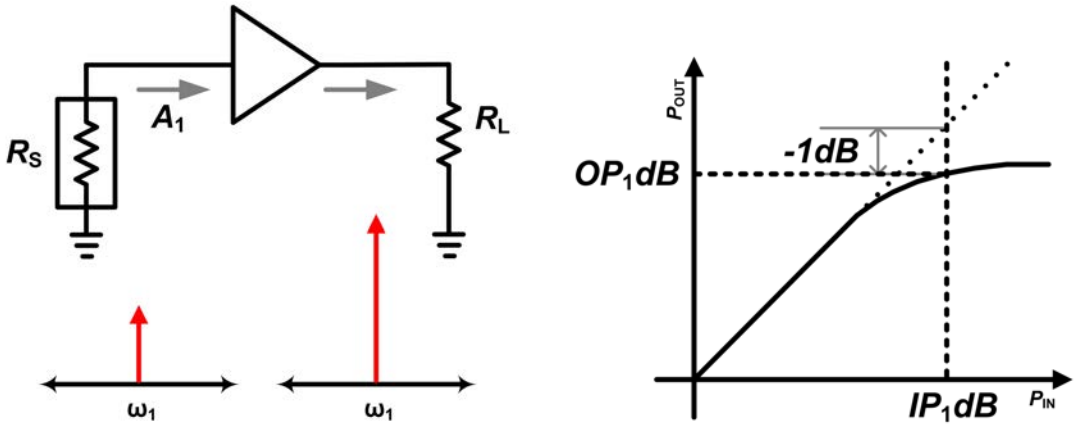

(a) (b)

Figure 2.2: Conceptual diagram of (a) a nonlinear amplifier system, and (b) gain compression response.

2.1.2 Linearity

In any system, it is well-known that signals cannot be infinitely large. There are several upper limiting phenomena, but most commonly, nonlinearity is used to analyze the upper limits of a system. Nonlinearity does not cause a unique phenomenon; rather, it gives rise to numerous issues such as gain compression, desensitization, cross modulation, intermodulation distortion (IMD), and amplitude modulation to phase modulation (AM-PM), among others. In many system designs, the most influential metrics are gain compression and IMD, and therefore, the analysis of gain compression and IMD is often prioritized. Additionally, 3rd order harmonic analysis, such as IMD analysis, will be discussed later, as the 3rd order harmonic is used for the main linearity analysis in this work.

Under the assumption of weak nonlinearity and memorylessness, the nonlinearity of a system can be characterized using a Taylor series expansion, as shown below [45].

$$y(y) = \alpha_1 x(t) + \alpha_2 x^2(t) + \alpha_3 x^3(t) + ... \tag{2.6}$$

To examine the output of a system, a single tone signal $x(t) = A\cos\omega t$ can be substituted into Equation. 2.6 resulting in the frequency components shown in Equation. 2.7.

$$y(y) = \alpha_1 A\cos\omega t + \alpha_2 A^2\cos^2\omega t + \alpha_3 A^3\cos^3\omega t + ... \tag{2.7}$$

By applying trigonometric identities, the output can be factored by frequencies:

$$y(y) = \frac{\alpha_2 A^2}{2} + \left(\alpha_1 A + \frac{3\alpha_3 A^3}{4}\right)\cos\omega t + \frac{\alpha_2 A^2}{2}\cos 2\omega t + \frac{\alpha_3 A^3}{4}\cos 3\omega t + ... \tag{2.8}$$

The output of a system can be factored by frequencies using trigonometric identities as shown in Equation. 2.8, which reveals important information about the system. First, signals at integer multiples of the input signal frequency, known as harmonics, appear at the output with amplitudes proportional to the input signal amplitude raised to the corresponding power. Harmonics are easier to suppress when the input frequency is high due to the larger frequency difference with the desired signal. Second, the fundamental gain is modified as the gain $\alpha_1 + 3\alpha_3 A^2/4$. In the CMOS process, where $\alpha_1\alpha_3 < 0$, the fundamental gain is compressed with high input signal amplitudes. The 1dB compression point, where the gain is compressed by 1dB compared to the small signal gain, is used to evaluate the linearity of system components.

A theoretical calculation can be done using the coefficients in Equation. **??** to find the value of the 1dB compression point simply by equating the gain to 1dB less than the ideal linear gain α_1.

$$A_{1dB} = \sqrt{0.145\left|\frac{\alpha_1}{\alpha_3}\right|} \tag{2.9}$$

When systems send a modulated signal, the signal is a frequency-spanned signal and not a single tone. It can be thought of as a series of multiple tones, which cause intermodulation. For the sake of simplicity, the analysis usually considers two tones as input. By substituting the signal $x(t) = A_1\cos\omega_1 t + A_2\cos\omega_2 t$ into Equation. 2.6 we can examine the output results.

$$\begin{aligned} y(t) =& \alpha_1 (A_1\cos\omega_1 t + A_2\cos\omega_2 t) \\ &+\alpha_2 (A_1\cos\omega_1 t + A_2\cos\omega_2 t)^2 \\ &+\alpha_3 (A_1\cos\omega_1 t + A_2\cos\omega_2 t)^3 \\ &+... \end{aligned} \tag{2.10}$$

Thus, Equation. 2.10 can be derived. Again by applying trigonometric identities, a more meaningful form can be obtained. For further simplification of the analysis, the most important terms are:

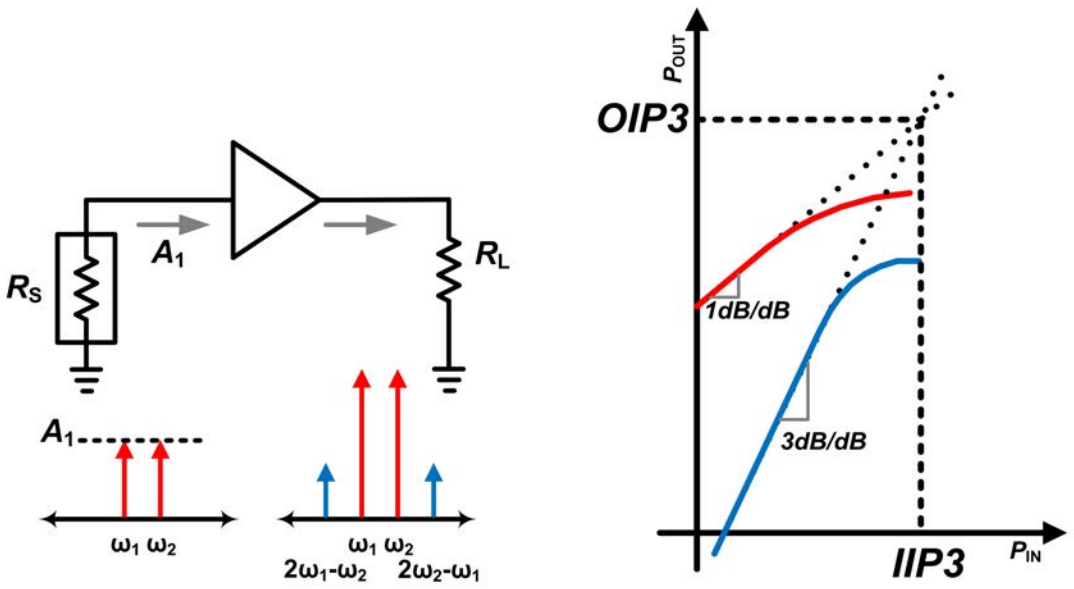

(a) (b)

Figure 2.3: Conceptual diagram of (a) a nonlinear amplifier system, and (b) intermodulation response.

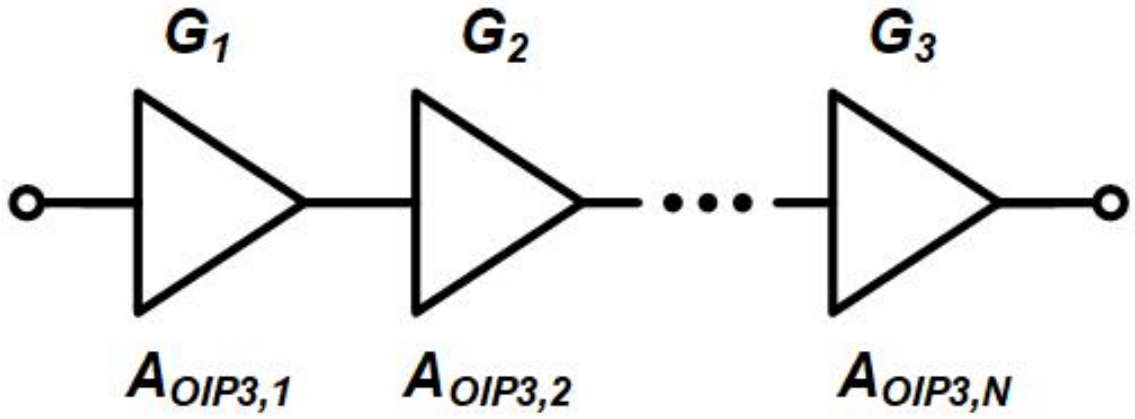

Figure 2.4: Block diagram for cascaded amplifiers with varying gains and IP3s.

$$\begin{aligned} y(t) = & \frac{3\alpha_3 A_1^2 A_2}{4} \cos\left(2\omega_1 - \omega_2\right) t \\ & + \frac{3\alpha_3 A_1 A_2^2}{4} \cos\left(2\omega_2 - \omega_1\right) t \end{aligned} \tag{2.11}$$

The third-order intermodulation (IM3) components are the result of the third-order

nonlinearity, occurring at frequencies that are not multiples of any of the input frequencies. They are commonly referred to as third-order IMDs because they are more important than any other IMDs, as they occur at frequencies too close to the signal to filter out easily. Higher-order IMDs or harmonics are generally more degraded than lower-order ones and can be filtered out more easily. Therefore, a new important metric for nonlinearity is defined, called the third-order intercept point (IP3), as shown conceptually in Figure. 2.3.

To calculate the IIP3, two sinusoidal signals with the same amplitude should be input to the nonlinear amplifier. Then, the amplitude of the IM3 signal can be simplified to $3/4 \cdot \alpha_3 A^3$. The IIP3 point can be obtained by equating this value to the fundamental signal:

$$|\alpha_1 A_{IIP3}| = \left|\frac{3}{4}\alpha_3 A_{IIP3}^3\right| \tag{2.12}$$

Solving this equation:

$$\frac{A_{IIP3}}{A_{1dB}} = \sqrt{\frac{4}{0.435}} \approx 9.6dB \tag{2.13}$$

an intriguing relationship that allows us to use both values interchangeably can be found.

In practical situations, it's possible for the value of OIP3 to exceed the supply voltage, and the higher order nonlinearities can also affect the intercept point of the fundamental signal and the IM3 signal. As a result, the intercept point may deviate significantly from the defined IP3 point. To address this issue, extrapolation techniques are often used to estimate the IP3 point that aligns with the established definition, as demonstrated in Figure. 2.3.

When designing a transceiver system, it is common to have multiple stages with varying levels of gain and linearity connected in series as depicted in Figure. 2.4. The overall linearity of the system, which is represented by the IP3 point, can be estimated using the following approach:

$$\frac{1}{A_{IIP3}^2} = \frac{1}{A_{IIP3,1}^2} + \frac{\alpha_1^2}{A_{IIP3,2}^2} + \frac{\alpha_1^2\beta_1^2}{A_{IIP3,3}^2} + ... \tag{2.14}$$

where $A_{IIP3,j}$ is the input amplitude at the IP3 point of the j^{th} cascaded stage. α_1 and β_1 are the ideal linear gains of the first stage and the second stage, respectively. It is important

to note that the linearity of later stages must be higher than that of earlier stages in order to avoid degradation of the overall linearity. This is due to the fact that the IP3 of each stage is scaled down by the gain of all the previous stages. Equation. 2.14 is applicable not only for IP3 but also for other nonlinearity component descriptions, such as P1dB.

The Equation. 2.14 can be alternatively expressed in terms of the output IP3, A_{OIP3} by multiplying it with the total system gain. This yields:

$$\frac{1}{A^2_{OIP3}} = \frac{1}{A^2_{OIP3,N}} + \frac{1}{G_N A^2_{OIP3,N-1}} + \frac{1}{G_N G_{N-1} A^2_{OIP3,N-2}} + ... \tag{2.15}$$

where G_N is the gain of last stage and $A^2_{OIP3,i}$ is output IP3 point of the i^{th} stage. Here, again, the linearity of the last stage is most dominant to cascaded linearity.

2.1.3 Bandwidth and Data Rate

As mentioned in the introduction, boosting the frequency and bandwidth is the fundamental way to enhance the data rate of a transmitter system. At higher frequencies, more bandwidth resources become available, allowing us to use 10% of the center frequency. To calculate the channel capacity in bits per second, Nyquist's formula is employed for a multi-level signaling communication system:

$$C = 2B \log_2 M \tag{2.16}$$

where B is the baseband signal bandwidth, and M is the number of different symbol values. The term 2B can be substituted by the symbol rate (symbols per second or baud).

However, designing a high-bandwidth transmitter can be challenging for designers due to the limitations of the mixer and power amplification. Increasing the bandwidth infinitely seems impossible. Therefore, shifting the different PA stages is a possible solution to enhance the bandwidth and, in turn, the data rate of our system.

In practice, the frequency spectrum is not rectangular, so raised cosine filtering is used to limit the infinite time-domain characteristics [46]. This type of filtering results in some excess bandwidth that can be characterized by the roll-off factor, usually ranging from 0.25 to 0.35. Designers must carefully consider the factor's impact on the system design procedure. Fig. 2.5 illustrates the frequency response of a raised-cosine filter with various roll-off factors.

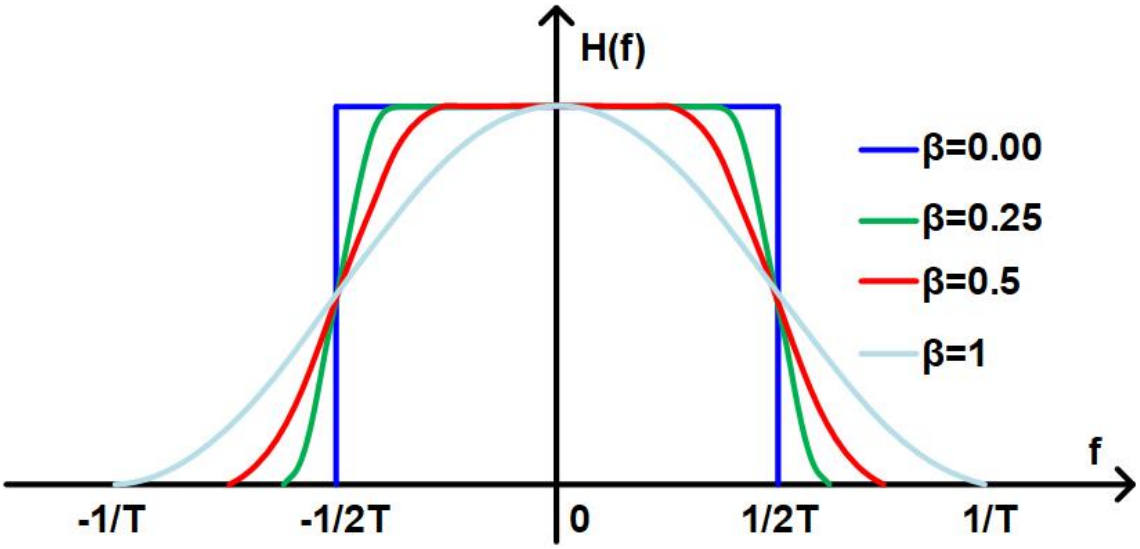

Figure 2.5: Frequency response of the raised-cosine filter with different roll-off factors.

2.1.4 Digital Modulation

Integrating three design parameters from three previous sections, noise, linearity, and bandwidth, one comprehensive signal quality metric can be defined:

$$SNDR = 10\log_{10}\frac{S}{N+D}, \tag{2.17}$$

where the S denotes signal power after passing a noisy and nonlinear gain system, N is for the output noise power of the system, and D is for the newly generated interference output power of the system by distortion. D is normally considered as adjacent channel power (ACP) which comes from 3^{rd} order intermodulation terms. The concept of the ACP is exactly the same as the IMD3, but with a non-zero bandwidth signal, not two tones. The noise, N can be calculated with the signal bandwidth:

$$N\,[W] = (kT_0(F-1)BG) \tag{2.18}$$

or in dBm unit,

$$N\,[dBm] = -174dBm/Hz + 10\log_{10}(F-1) + 10\log_{10}B + 10\log_{10}G \tag{2.19}$$

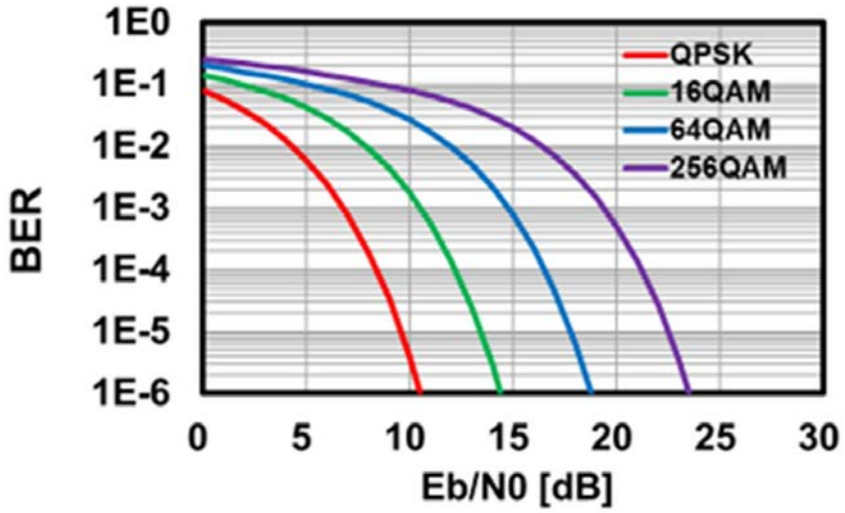

Figure 2.6: Calculated BER over the E_b/N_0 of the QAM modulations.

where the k is Boltzmann constant, T_0 is the system temperature, F is the noise factor, B is the signal bandwidth, and G is the system gain. The SNDR is a very important parameter to decide the success and failure of communication under a given modulation scheme.

Compared to analog modulation, digital modulation offers greater noise immunity and better compatibility, making it the preferred choice for modern wireless communication systems. Digital data can also benefit from encryption and error-correcting algorithms to ensure data integrity. Our daily electronic devices, such as personal computers, smartphones, tablets, and cars, rely heavily on digital data processing centers to operate effectively.

Various digital modulation schemes are available for different types of communication systems. Simple communication systems, such as onboard direct connections, often use amplitude shift keying (ASK), frequency-shift keying (FSK), and phase-shift keying (PSK) modulation. ASK is used for amplitude modulation in analog domains, while FSK and PSK are used for frequency and phase modulation domains, respectively.

More advanced modulation schemes, such as M-array digital modulation, allow one symbol to represent multiple bits (N) with several signal levels (M). The values of N and M are related by the equation:

$$N = \log_2 M \tag{2.20}$$

This thesis will focus on two typical digital modulation schemes for analysis and mea-

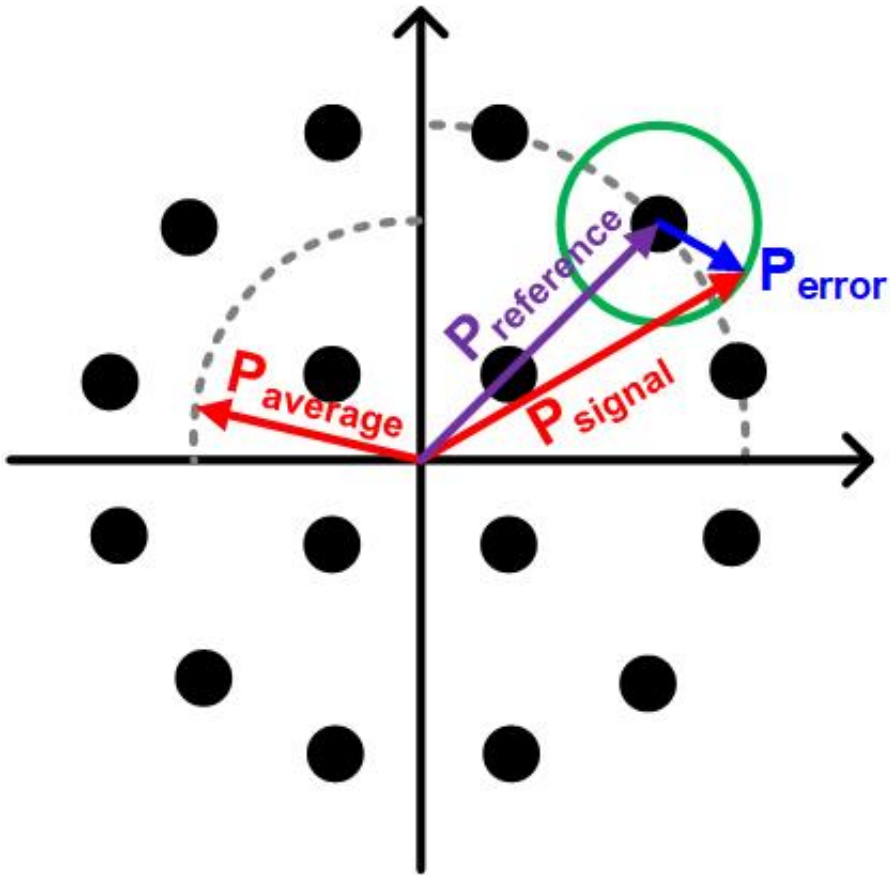

Figure 2.7: Constellation figure of 16-APSK modulation for the definition of the EVM.

surement: quadrature PSK (QPSK) and M-array amplitude and phase shift keying (M-APSK). The reason APSK is chosen instead of quadrature amplitude modulation (QAM) is that APSK is much more immune to signal compression due to the system nonlinearity at a fixed power level compared to QAM. This means that the average signal power with APSK is higher than that with QAM under the same power amplifier (PA). Quadrature modulation involves 90-degree phase shifting for modulated signals at the same carrier frequency. This method can help distinguish different signal symbols that have different signal phases, even if their amplitude levels are the same. Quadrature modulation can improve spectrum efficiency by doubling the transmission rate compared to conventional PSK or FSK modulation schemes. QPSK can support 2 bits in one symbol, while APSK can support more than 2 bits modulation scenarios with a higher signal-to-noise ratio (SNR). The APSK modulation scheme can use different amplitudes and phases to form the symbol, increasing the link speed while keeping the same occupying bandwidth. For example, 16-APSK modulation is composed of 16 constellations with 4 bits of information in one symbol.

Various indicators have been introduced in the past to evaluate communication system performance, with bit error rate (BER) being one of the most common. BER shows the ratio between the number of bit errors and the total number of transmitted bits during a time interval. A BER of 10^{-3} is considered acceptable for wireless communication. To make the BER value more relevant to the wireless system design process, it can be directly linked to the signal-to-noise ratio (SNR) or bit energy per noise density, E_b/N_0, which can be derived using probability functions. Figure. 2.6 shows the relationship between BER and E_b/N_0 as a plot. A 7 dB E_b/N_0 is required to achieve QPSK wireless communication, while a 14 dB SNR is required to achieve a 64-QAM link.

Another commonly used method for evaluating digitally modulated wireless links is the error vector magnitude (EVM). The definition of the EVM is illustrated in Figure. 2.7. The resulting error vector is normalized to average signal amplitude and then converted to decibels using the following formula:

$$EVM(dB) = 10\log_{10}\frac{P_{error}}{P_{average}}, \tag{2.21}$$

where P_{error} is the average RMS power of the error vectors for each symbol, and $P_{average}$ is the power of the maximum point in the constellation. The EVM can also be represented as a percentage:

$$EVM(\%) = \sqrt{\frac{P_{error}}{P_{average}}} \times 100\%. \tag{2.22}$$

2.1.5 Phased Array

The emergence of 5G networks has brought about a significant shift in the way we think about wireless communication systems, and the phased-array system is at the forefront of this revolution. This technology is set to play a dominant role in the future of wireless communication, particularly in the context of the extremely wider coverage of the Low Earth Orbit (LEO) satellite terminals.

Compared to conventional isotropic antennas, phased-array antennas offer a number of advantages: electrical beamforming, high array gain, etc. The radiation pattern of an ideal isotropic antenna is the same in all directions, while a phased-array antenna with many elements can focus its radiation pattern in a specific direction. This allows for greater directional control, with reduced radiation strength in other directions. The

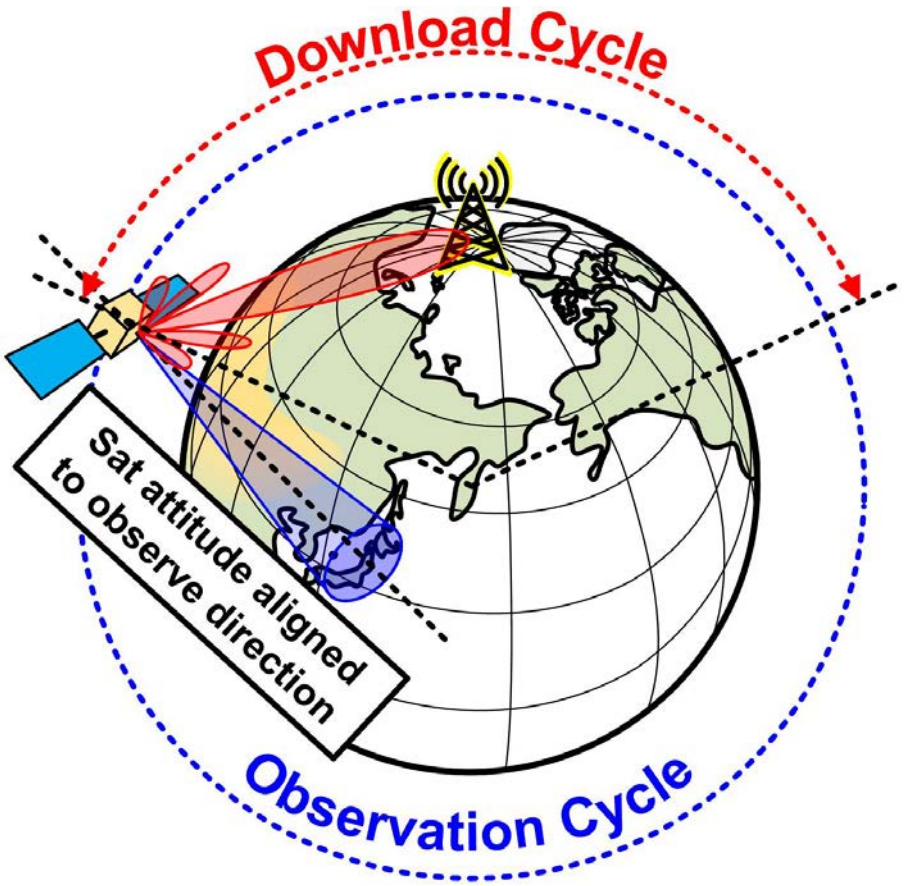

Figure 2.8: Diagram to show how the phased array increases the communication duration.

main difference between the ideal isotropic and phased-array antenna is referred to as the direction gain.

The use of phased-array antennas in SATCOM will help to improve the overall performance of wireless communication systems. These antennas can be used to enhance signal strength, increase coverage range, and provide better interference management. In addition, the directional control offered by phased-array antennas can help to reduce energy consumption and improve overall system efficiency. As such, the phased-array system is set to become an essential component of not only the cellular network but also SATCOM infrastructure, providing reliable and efficient wireless communication for a wide range of applications.

The phased-array antenna, which consists of multiple antenna elements, can significantly improve the directivity and reduce the sidelobe radiation pattern. By adjusting the RF signal phases among the different antenna elements, the beam direction can be controlled and the radiation pattern can be focused in a specific direction. The more antenna elements are used, the higher the radiation pattern will be in the main direction

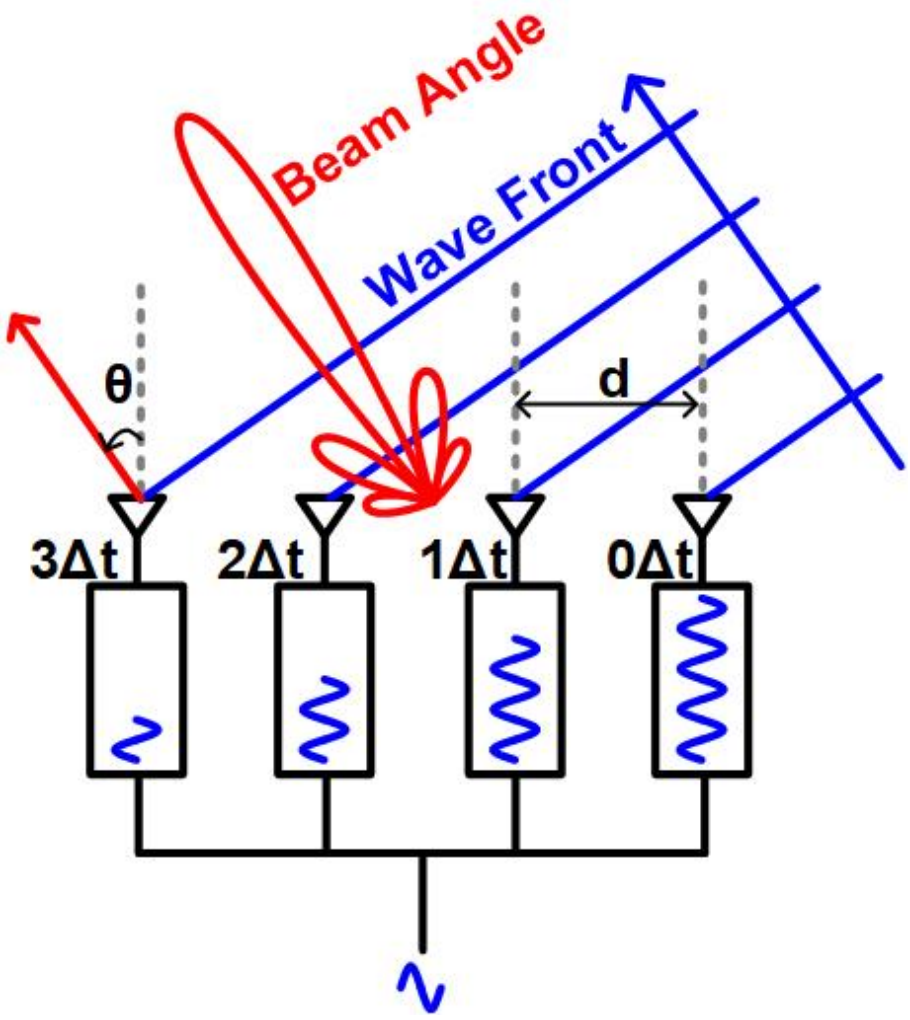

Figure 2.9: Principle of the phased array operation.

and the narrower the beam will be. Therefore, the phased-array system is widely used in modern communication systems, especially in the upcoming 6G network communication system, and is expected to play a dominant role in the extremely wider coverage using LEO satellite terminals.

In addition to the advantages discussed earlier, phased arrays can enhance data throughput. While the phased array itself cannot increase data bandwidth, it can increase communication duration, which in turn improves overall data throughput. Figure. 2.8 illustrates how the phased array can achieve this. By steering the beam angle, the satellite can initiate communication during the early phases of an orbit cycle and maintain it until the late phases, thus increasing communication duration. A conventional single antenna system can achieve similar results by adjusting the direction of the satellite. However, many other

optical cameras or mission equipment are typically aligned or fixed to the satellite body. This means that when communication starts and the satellite body is turned towards the ground station, any other missions will be interrupted. In summary, the phased array can increase communication duration without interfering with other missions.

The implementation of the phased-array system is depicted in Figure. 2.9. On the TX side, the RF radiation signal is generated by implementing different phase shifts for different elements. For a certain beam angle θ, the linear progressive phase difference α between different elements can be expressed using the following equation:

$$\alpha = -\beta d \sin\theta \tag{2.23}$$

where the β is the wave number which can be defined using wavelength, λ as:

$$\beta = \frac{2\pi}{\lambda} \tag{2.24}$$

As noted earlier, it should be emphasized that the equation provided is specifically for a half-wavelength spaced linear element array, and the beam angle may vary for different distances between the transmitter elements.

After the signal is radiated by the PA and antennas, the RF signal will be added coherently with the in-phase amplitudes of the different antenna elements at a set beam-steering direction. This results in an additional antenna gain of $20\log_{10} N$ for the transmitter, where N is the number of elements in the linear array.

2.2 TX Design Challenge for LEO Small Satellites and Research Objectives

This section discusses small-satellite-specific research objectives for the TX design. To run an LEO small satellite constellation, there arise three important requirements for designing in TXs. This thesis targets these three requirements as research objectives in Ka-band CMOS phased-array TX implementation.

1. High Data Throughput

   As mentioned in Chapter 1, the demand for high data throughput is increasing rapidly to meet the requirements of the IoT era, handle high-resolution imagery data from EESS satellites and satellite constellations, and manage the massive data

traffic from inter-satellite data links in satellite internet access services, among others.

2. Low Cost

   Constructing an LEO small satellite constellation involves launching a large number of satellites, which can be costly. To mitigate launch costs, satellites must be small and lightweight so that multiple satellites can be launched using a single rocket, thereby reducing expenses. However, the low altitude of LEO satellites exposes them to air and atmospheric friction, which can shorten their lifespan, necessitating frequent management and re-launching.

   In addition to launch costs, IC fabrication represents a significant expense that can increase the overall cost of LEO satellite constellation systems. In the past, discrete compound semiconductor components were used for SATCOM systems, as they were manufactured in low volumes. However, the implementation of LEO small satellite constellation systems requires a high volume of satellite launches, which, in turn, necessitates a significant amount of IC fabrication. As discussed in Section 2.2.2, the implementation of phased arrays can further increase the number of required ICs.

3. Low Power Consumption

   Due to the small size of small satellites, the area available for solar cells, which are the main source of energy for the satellite, is limited. Furthermore, unlike GEO satellites, LEO satellites orbit closer to Earth's surface, resulting in more frequent eclipses during each revolution. This not only limits the amount of solar energy that can be generated but also the time during which it can be generated.

2.2.1 High Data Throughput

Dual Circular Polarization

In order to achieve a higher data rate, it is widely recognized that there are two standard methods: 1) increasing the bandwidth of the signal, and 2) increasing the SNR to support a higher M-ary modulation signal. Not only the ways listed above but also polarization multiplexing can increase the data rate. For example, two linearly polarization, horizontally, and vertically polarized signals can be independently received by the two differently polarized antennas, i.e. horizontally and vertically polarized antennas. This means that if the two polarized antennas are used for loading two independent random signal streams with the same carrier frequency to double the data rate. Likewise, any two independently

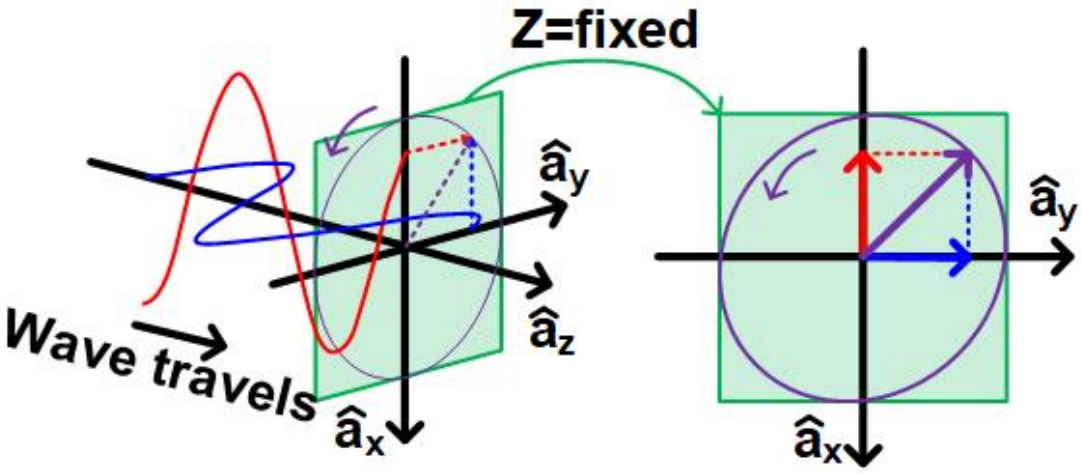

Figure 2.10: Graphical description of the left-handed elliptical polarization.

defined polarized signals can be selectively received, thus doubling the data rate. The one most popular two independent polarizations are circular polarizations: left-handed circular polarization (LHCP), and right-handed circular polarization.

Circular polarization has been adopted for decades for the SATCOM systems for their polarization because circular polarization has a lot of advantages [47]:

- Antenna orientation alignment is not required in both TX and RX
- Less susceptible to discrimination by multi-path propagation
- Resistant to signal degradation due to inclement weather conditions for reflectivity, absorption, phasing, and multi-path.

Thus this thesis also targets the implementation of dual circular polarization. To understand polarization including circular polarization, linear polarization, or generalized polarization, elliptical polarization, which is a general case of polarization, is illustrated in Figure. 2.10. Not only circular polarization but any type of polarization can be represented with two linear polarization basis vectors, $\widehat{a_x}$, $\widehat{a_y}$. The generalized polarization can be expressed as [48]:

$$\widehat{e}(t) = \widehat{a_x} E_x \cos(\omega t) + \widehat{a_y} E_y \cos(\omega t + \delta_L), \tag{2.25}$$

where E_x is the electric field intensity in the X-axis direction, E_y is the electric field intensity in the Y-axis direction, and δ_L is the phase difference between two X and Y-axis

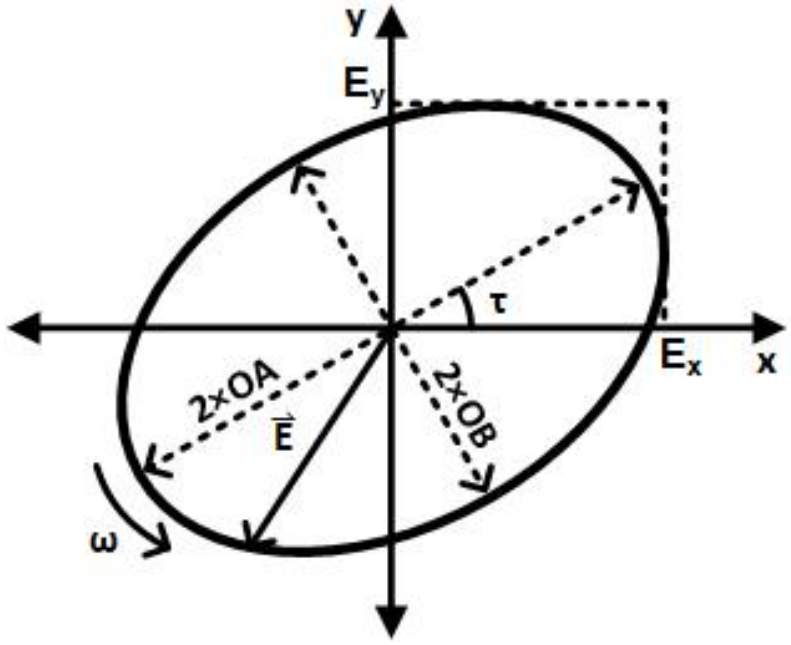

Figure 2.11: Mathematical description of the left-handed elliptical polarization.

direction signals. Again, this expression can be reproduced using phasor and dividing the equation by E_x:

$$\widehat{e} = \widehat{a_x} + \widehat{a_y}\rho_L e^{j\delta_L}. \tag{2.26}$$

Noted that the new parameter, ρ_L is the amplitude difference between two X and Y-axis direction signals. Using the Equation. 2.26, several extreme cases can be categorized.

- if ($\rho_L = \infty$) & (δ_L : $don'tcare$), then Horizontal LP
- if ($\rho_L = 0$) & (δ_L : $don'tcare$), then Vertical LP
- if ($\rho_L = 1$) & ($\delta_L = +90°$), then RHCP
- if ($\rho_L = 1$) & ($\delta_L = -90°$), then LHCP
- if ($\rho_L \neq 1$) & ($\delta_L = \pm 90°$), then Elliptical CP

Here, the other polarization description parameters, major axes, and their tilt angle can be defined as shown in Figure. 2.10.

$$\overline{OA}, \overline{OB} = \sqrt{\frac{1}{2}\left(E_x^2 + E_y^2 \pm \sqrt{E_x^4 + E_x^4 + E_y^4 + 2E_x^2E_y^2\cos 2\delta_L}\right)} \tag{2.27}$$

$$\tau = \frac{1}{2}\arctan\left(\frac{2E_x^2E_y^2}{E_x^2 - E_y^2}\cos\delta_L\right) \pm \frac{\pi}{2} \tag{2.28}$$

Here, extreme cases are considered again with the Equation. 2.27 and 2.28.

- if ($E_y = 0$) : only one major axis remains, Horizontal LP
- if ($E_x = 0$) : only one major axis remains, Vertical LP
- if ($E_x = E_y$) & ($\delta_L = \pm 90°$): $\overline{OA} = \overline{OB} = 1$, $\tau = \pm 90°$, LHCP or RHCP

From the above expressions, one metric, axial ratio (AR) for evaluating how the polarization is close to the ideal polarization can be defined.

$$AR = \frac{\overline{OA}}{\overline{OB}} \tag{2.29}$$

If the AR becomes ∞, then it means the signal is linearly polarized. If the AR equals 1, then the signal is circularly polarized. In the dual linearly polarized system case, once the measured AR is not ∞ or 0, that means the coupling to each opposite polarization RX antenna happens as the same amount as the AR value. AR is a very convenient metric to measure the coupling of one polarized signal to the other independently polarized signal. However, AR does not provide the intuition to observe the coupling between two independently circularly polarized signals. In the circular polarization case, cross-polarization discrimination (XPD) is much more convenient and it can be defined as:

$$XPD = \frac{AR + 1}{AR - 1} \tag{2.30}$$

The Equation. 2.30 does not give intuition on how the XPD is related to the coupling, yet. Because the LHCP and RHCP are orthogonal to each other, any type of polarized signals can be decomposed into the LHCP component and RHCP component. Figure. 2.12 illustrates decomposed polarizations with vector relationship further extended from

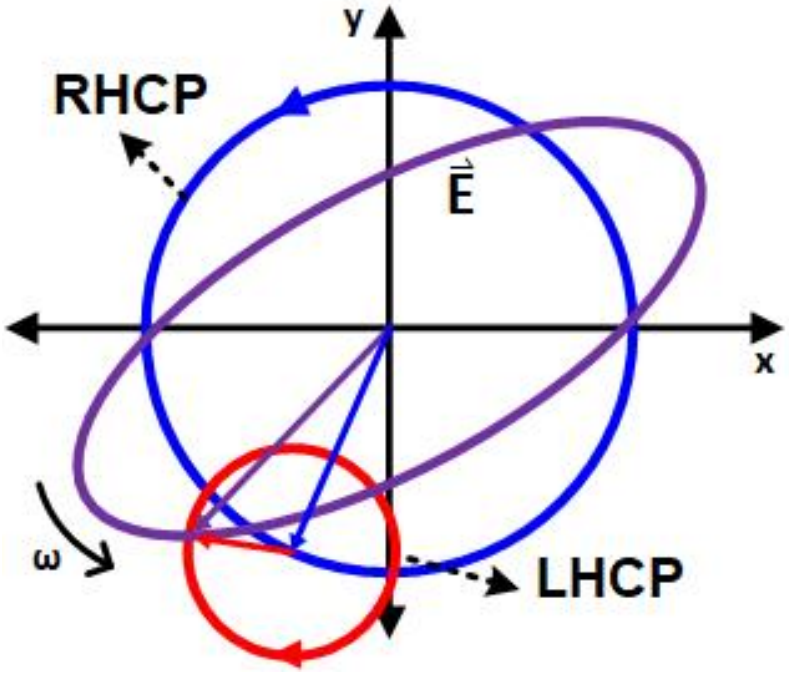

Figure 2.12: Mathematical description of the left-handed elliptical polarization.

Figure. 2.10. As illustrated in the Figure. 2.12, electric field intensities of the two polarized signals can be intuitively compared. The two intensities ratio is the definition of the XPD.

While circular polarization is widely used in SATCOM applications, its implementation is not as easy as linear polarization. In literature, [6, 7], two ways of circular polarization generation are presented. One is to use a circularly polarized patch antenna. The other is to re-use the phase shifter (PS) and variable gain amplifier (VGA) in a phased array beamformer. The first methodology gives the non-complex implementation of the circular polarization, but the circularly polarized patches are fabricated on printed circuit board (PCB), thus suffering from huge process variation and low XPD. The other methodology synthesizes the circularly polarized signal with the two linearly polarized signals. Because it uses PSs and VGAs, even though there process variation happens, the XPD can be recovered as well as the resolution of the PSs and VGAs. However, reusing the beamformer cannot support dual circular polarization. The details will be discussed in Chapter. 5. As discussed, the generation of clean dual circularly polarized signals with high XPD is challenging.

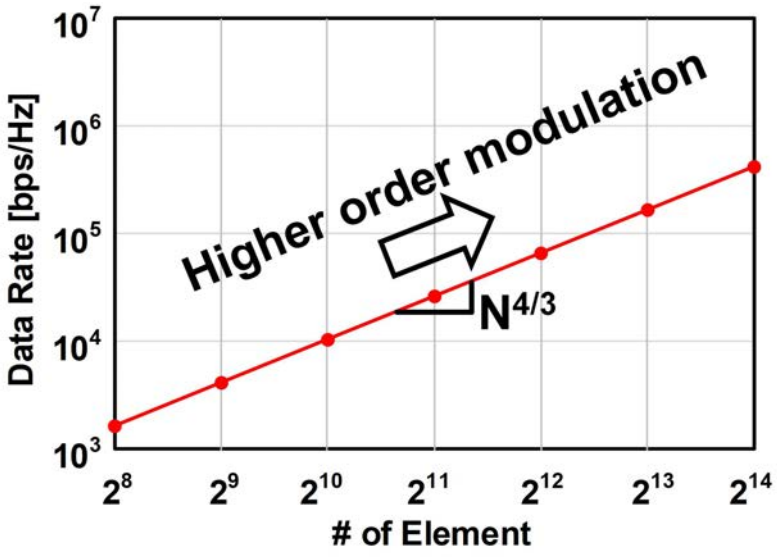

Figure 2.13: Relationship between data rate and the number of elements.

Large Array Size

A large array size also can be helpful for higher data rate. Figure. 2.13 shows the relationship between data rate and the number of elements. For this model, received power level is assumed to be proportional to the number of elements to the power of 2. In addition to the received power level, DVB-S2X standard [49] is referenced to found out the relationship between a data rate and required SNR, which is proportional to the power of 2/3. Thus, the total data rate is proportional to the number of elements to the power of 4/3. To address only proportionality, data rate is set to 1 $[bps/Hz]$. From above discussion, it is obvious that the more the number of elements is, the faster data rate is.

2.2.2 Low Cost

Launch Cost

Figure. 1.2 shows overall LEO sat launch costs per kg are being reduced, however, it is still too much expensive to build a full constellation. Even worse, building a satellite constellation requires a lot of satellites. Even though the satellite size is small, launching a lot of satellites is costly, thus the satellite size and weight must be reduced as small as possible.

One more factor that boosts the required launch number is that the lifetime of the LEO satellite is around 5 years which is very short compared to other orbits. This is because there is atmospheric friction that slows the satellite's flying speed down. Because of the

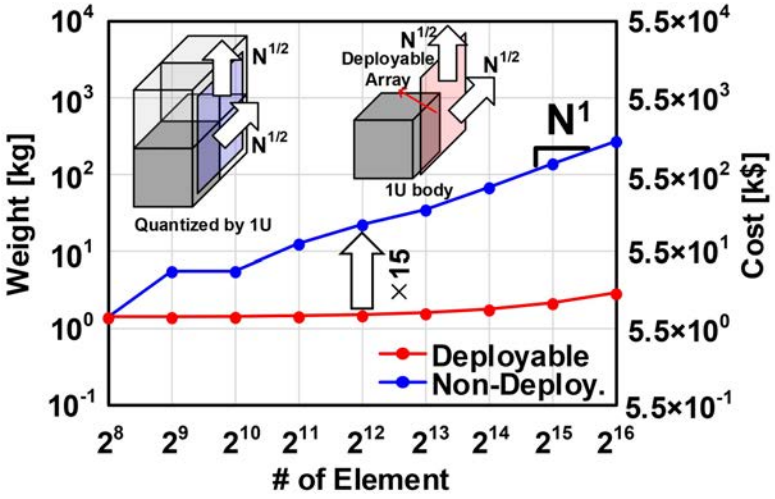

Figure 2.14: Relationship between launch cost and the number of elements.

short lifetime, the more frequent re-launch of rockets to replace the fallen satellites is mandatory.

Figure. 2.14 shows simplified launch cost to the LEO of two different types of satellite over the number of elements: deployable antenna with cube-sat, non-deployable antenna with square shape satellite by 1 U satellite body unit size. the 1 U is the unit satellite body size of the CubeSat, which is 10cm×10cm×10cm. In order to evaluate the cost, the price of SpaceX rideshare (5,500 $/kg) is referenced being addressed that the launch cost is proportional to the weight. The non-deployable case is assumed to have quantized satellite size increase by 1U CubeSat. Thus, the volume or weight is proportional to the number of elements. The deployable case is assumed that the antenna is stowed into 1 U of the CubeSat size, and the area or the weight is proportional to the number of elements. A volumetric mass of the non-deployable array is assumed to be 1,360 kg/m^3, and an areal mass of the deployable array is assumed to be 0.82 kg/m^2. From the above comparison, at the 4096-element case, deployable array antenna expected to have 1/15 times lighter weight than non-deployable array case.

Fabrication Cost

In addition to the cost of rocket launches, the manufacturing cost of the TX IC is another significant expense. Conventionally, lots of SATCOMs have used a single expensive compound semiconductor transceiver (TRX) with a single antenna. Because the single antenna provides wide coverage and the single compound semiconductor TRX provides high output power, a single compound semiconductor TRX, and a single antenna solution is an adequate solution for a single satellite system. However, this solution is not the best

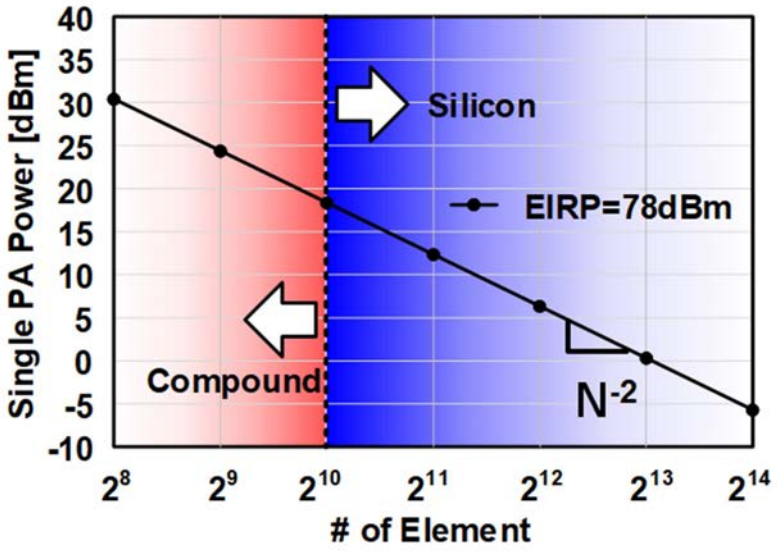

Figure 2.15: Appropriate process depending on single power amplifier's output power over the number of the elements.

solution anymore in LEO small satellite constellation system. With the emergence of the phased array in SATCOM, the LEO satellite constellation requires countless TX IC chips. Figure. 2.15 shows the appropriate process depending on single power amplifier's output power over the number of the elements. The graph intuitively first shows, under the fixed EIRP, what single PA power should be over the number of the array elements. And then, depending on the single PA power, what process is appropriate can be represented. With relatively lower power level, silicon is much appropriate than compound semiconductors. Thus, together with low-cost silicon process, the lowered fabrication cost is expected. This paradigm shift made the compound semiconductor processes not charming solutions anymore with their pathetic yield and fabrication cost. Instead, the CMOS TRX solution is more prominent in this situation which requires mass production. With its fast-increasing performance, high yield, and low mass-production cost, the CMOS process became one of the distinguished processes for TRX fabrication.

2.2.3 Low Power

Limited Solar Energy

Small-sized satellites in LEO orbits can solely rely on solar energy as a power source. Although nuclear power or chemical-combustion energy sources may be considered, a nuclear power source is typically too large to be mounted on a small satellite, and chemical-combustion energy sources require oxygen which is not readily available in space. The

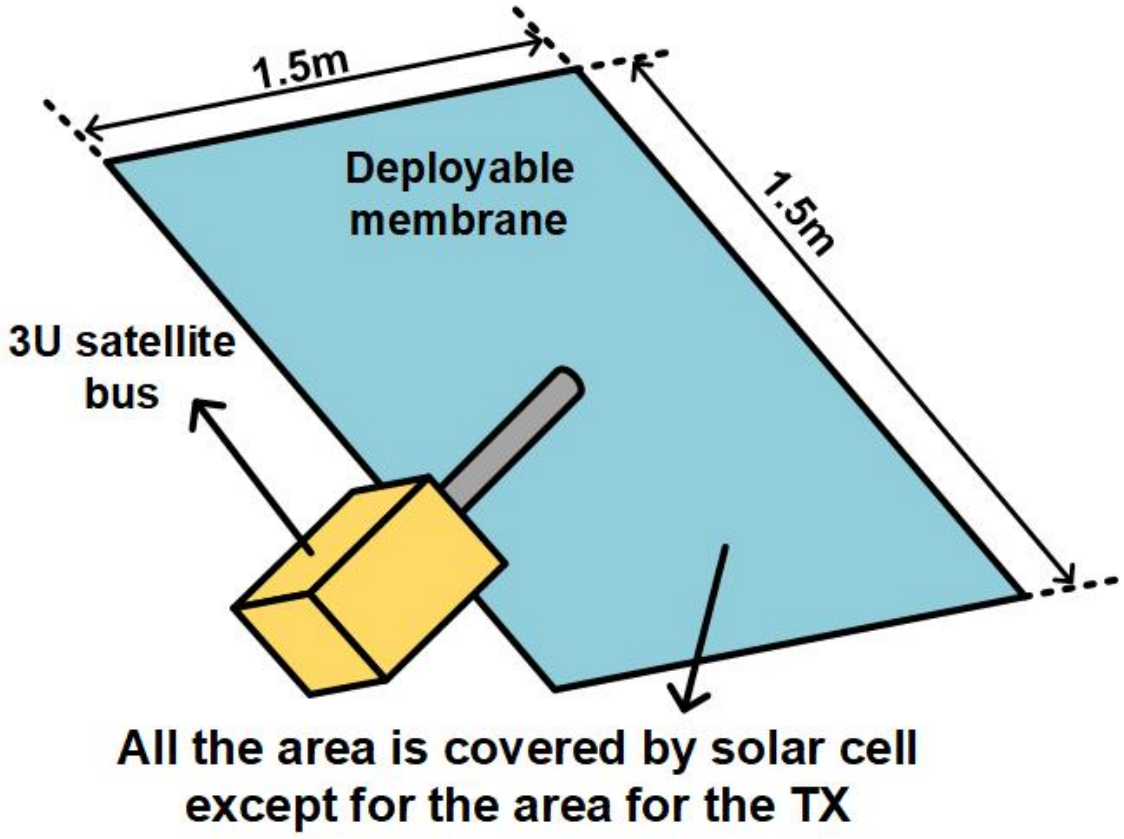

Figure 2.16: Satellite and solar cell geometry condition for the orbit average power simulation.

small size of the satellite not only limits nuclear power sources but also the solar energy source itself. Because solar cells generate more energy with more solar light reception area. Under this energy-limited environment, SATCOM systems, propulsion systems, attitude determination and control systems (ADCS), and control computers should share solar energy. Thus, power budgets for satellites must be carefully considered. While this thesis does not delve into the design of power budgets, it does present data on the amount of solar energy that can be generated and the amount of power that small satellites can consume.

As will be discussed in Chapter. 3, deployable membranes and antennas will be considered to reduce the volume and weight [50]. Because the shape of the satellite is important in obit average power (OAP), the satellite with a deployable membrane is considered to calculate OAP as shown in Figure. 2.16. For the OAP calculation, a 0.8m×0.8m-sized membrane is considered and both the front and back surfaces of the membrane are covered with solar cells except for the area for TX. Because the TX area is small enough to ignore here, the TX area is not considered for OAP calculation. For the calculation, the

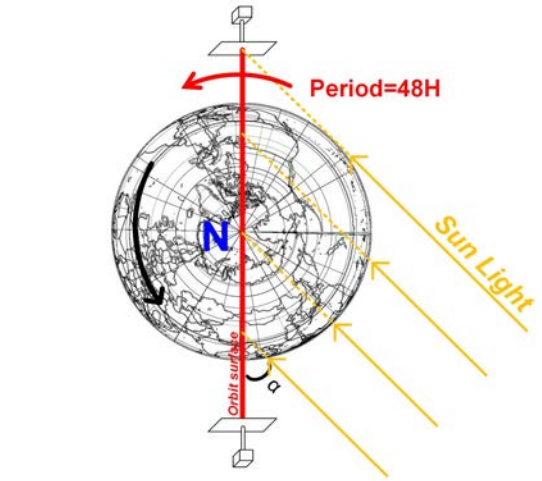

(a)

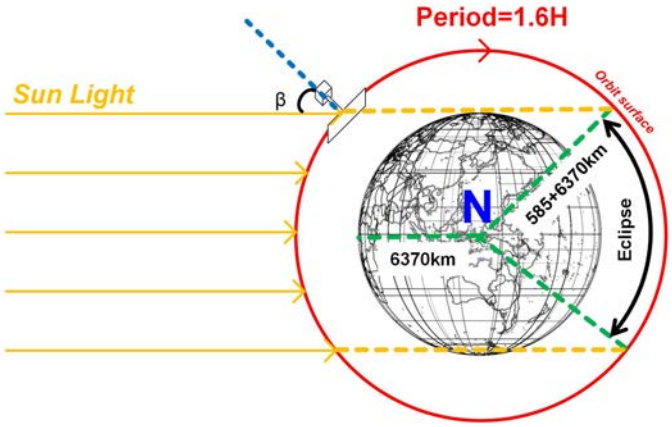

(b)

Figure 2.17: orbital condition for the orbit average power simulation: (a) north pole view, and (b) equator view.

power generated by solar cells is set to 95 $[W/m^2]$.

Now the orbit conditions should be discussed as shown in Figure. 2.17. A satellite flies at a 585 km altitude and passes the north pole and south pole in a revolution. This orbit is called the polar orbit. The orbit plane is defined as the surface drawn by the orbit trajectory. While the earth rotates counter-clockwise over 24 hours period, the orbit plane rotates counter-clockwise over 48 hours period which is two times as slow as the earth's rotation speed. The orbit plane is set to rotate with the sunlight direction to let all satellites receive even solar energy during an orbit plane cycle in the satellite constellation. The angle, α between sunlight and the orbit plane in Figure. 2.17(a) can be represented as $\alpha(t) = 2\pi/48 \times t$ and projection of the sunlight to the solar cell can be represented as:

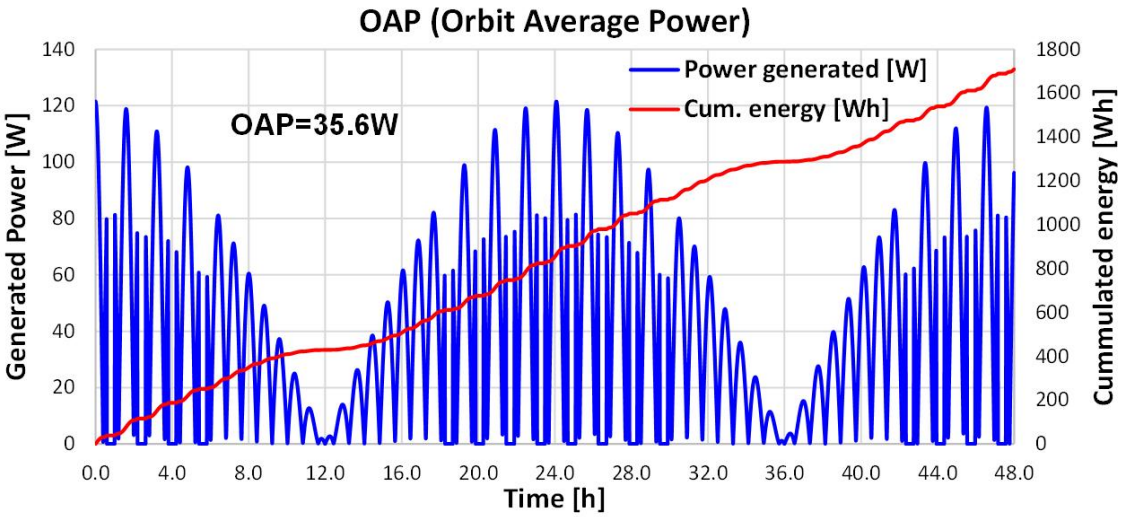

Figure 2.18: Simulated generated solar power in a satellite orbit cycle.

$$\cos\frac{2\pi}{48}t \tag{2.31}$$

where t is the time in "hour". One more dependency on the projection of the solar energy is the angle β in an orbit motion in Figure. 2.17(b). The attitude of the satellite is set that one side of the membrane forward to the earth's direction. The time-varying β can be expressed as $\beta(t) = 2\pi/1.6 \times t$ and sunlight projection to the solar cell by the angle β is:

$$\cos\frac{2\pi}{1.6}t. \tag{2.32}$$

Then, solar cell power per area, solar cell area, and all the projection terms are calculated together to achieve power generated by the solar cells.

$$P_{solar}(t)\ [W] = 95\ [W/m^2] \times 2 \times 1\ [m^2] \times \cos\left(\frac{2\pi}{48}t\right) \times \cos\left(\frac{2\pi}{1.6}t\right). \tag{2.33}$$

Furthermore, to include the eclipse effect, Equation. 2.34 can be considered as a conditional expression.

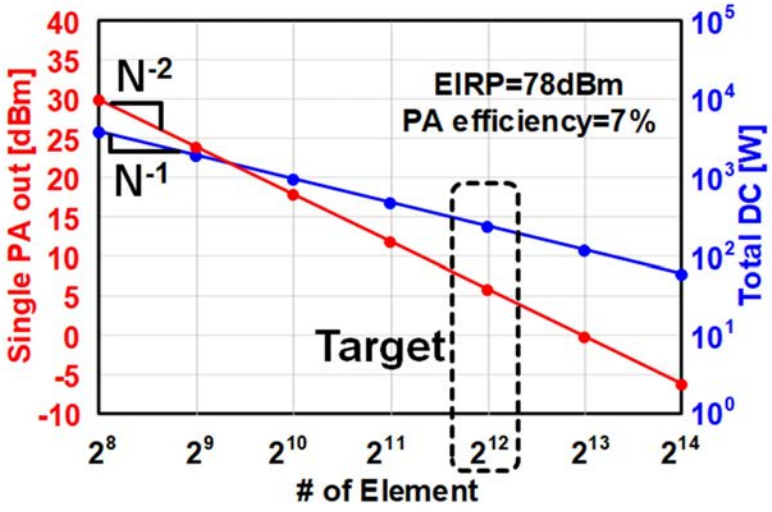

Figure 2.19: power dissipation reduction by large array antenna.

$$
\begin{aligned}
|\cos(\alpha(t))| &> \cos\left[90^\circ + \arctan\left(\frac{6370}{585+6370}\right)\right] \\
&\quad and \\
\cos(\beta(t)) &> -\left|\cos\left[90^\circ + \arctan\left(\frac{6370}{585+6370}\right)\right]\right| \\
&\quad then \quad P_{solar} = 0
\end{aligned}
\tag{2.34}
$$

Finally, a full description of the power generated by the solar cell is achieved in Equation. 2.33 and 2.34. With the equations, the resultant generated power is shown in Figure. 2.18. Blue curves denote generated power by the solar cells, P_{solar}, and the red curves denote accumulated energy in $[Wh]$. if the total generated energy during the cycle can be divided by the total cycle period, which is 48 hours, then, finally 35.6 [W] of the OAP can be calculated.

From the calculation, the desired satellite generates 35.6 W of average power. Considering power consumption by important satellite central control systems, 28% of power is deposited for SATCOM power consumption, which is 10 W of power consumption.

Thermal Radiation Issues

One critical reason to reduce power consumption is that black body radiation is the only mechanism to cool down the system unless the active cooling system is adopted, which is difficult to mount on small satellites. Unlike convection, the black body radiation cooling

performance is deadly limited. Because of this issue, absolute thermal energy generation must be avoided for small satellite system realization. If the array size becomes larger and the thermal area for black body radiation becomes larger, as well, thus better cooling performance. Furthermore, with a larger array size, total DC power consumption can be reduced, and the temperature of the system cools down further.

Lowering Cost by Large Array

The total DC power consumption in phased array can be reduced with large-sized array. This is because the larger array gain means the reduced single PA power and DC consumption under fixed EIRP. Figure. 2.19 demonstrates how the large array size can reduce the total DC power consumption. Under fixed EIRP, if the number of the elements increases, then single PA power must be reduced. In other words, under the same PA efficiency, DC power consumption of PA must be reduced, proportionally. As shown in the Figure. 2.19, while the single PA power reduces proportional to the number of elements to the power of -1, the total power consumption reduces proportional to the number of elements to the power of -2.

2.3 Satellite Phased Array TX

The previous discussion reveals that low cost, high data throughput, and low power consumption TX design in LEO small satellite constellation are essential requirements. To achieve the above three objectives for an LEO small satellite TX, this thesis proposes and realizes the below seven techniques:

- Dual circular polarization: High data throughput
- K-band: High data throughput
- CMOS: Low cost
- Phased array: High data throughput, Low power
- Deployability: Low cost

The first challenge is to implement dual circular polarization. By utilizing dual polarization, polarization multiplexing becomes possible, effectively doubling the signal bandwidth and data throughput. However, dual polarization is susceptible to process variations and temperature, among other factors. High-quality dual circular polarization requires elaborate circular polarization generation or calibration. The second and third challenges

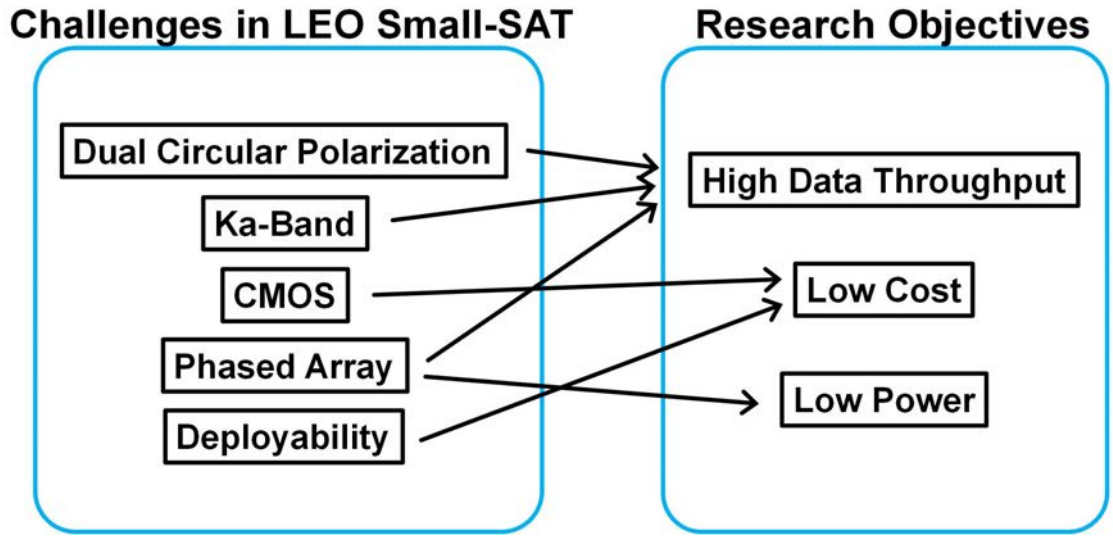

Figure 2.20: Relationship diagram between the challenges to the LEO small satellite and research objectives.

are Ka-band and CMOS technology. Combining these two technologies results in wider bandwidth and low-cost TX fabrication. The fourth challenge is the phased array, as discussed in Section 2.1.5. A phased array can increase communication duration and EIRP by increasing array gain without requiring a power output increase from the PA. This means that total PA power consumption can remain constant while EIRP increases. In other words, a phased array can reduce total power consumption while maintaining the given EIRP. The fifth challenge is the implementation of deployability. As a phased array is utilized in this thesis, a deployable phased array is one possible solution, but there may be manufacturing issues to address. Figure. 2.20 provides a clear overview of the relationship diagram between challenges and research objectives.

Moving forward in this chapter, we will analyze the link budget of the phased-array TX to determine the appropriate architecture. Subsequently, we will delve into the design targets and their potential social contributions, while also addressing the challenges that must be overcome.

2.3.1 Link Budget

While the success of SATCOM is decided by many factors, the most important design consideration is the careful design of the link budget. To achieve enough EIRP with limited power resources, the appropriate link budget design becomes more crucial.

Figure. 2.21 illustrates the designed link budget of the phased-array TX for the satellite segment in this thesis. For the link budget calculation, -6 dBm output power PA and

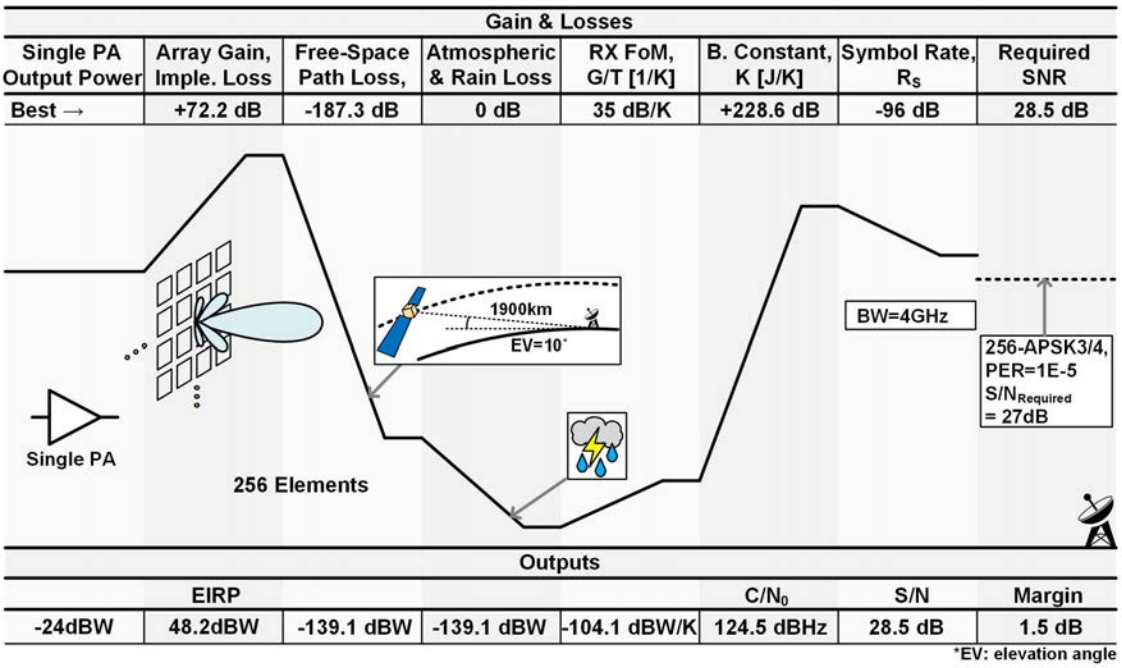

Figure 2.21: Link budget of the phased-array TX for the satellite segment in this thesis.

4096-element array size is used on the TX side. A 4096-element phased array antenna outputs 48.2 dBW EIRP. The 48.2 dBW signal travels a long distance, 1900 km, which is calculated from 585 orbit altitude and 10° ground station antenna elevation angle. The free space path loss (FSPL) from the 1900 km is calculated by:

$$FSPL = 20\log_{10}\frac{c}{4\pi} - 20\log_{10} d - 20\log_{10} f \tag{2.35}$$

where c is the speed of the light and d is the link distance, and f is the center frequency of the signal. From the Equation. 2.35, the FSPL is given as 187.3 dB. Because the Ka-band is susceptible to rain loss, 9 dB of the rain loss should be taken into account, as well [51–55]. However, for best link scenario, rain loss is set to 0 dB in Figure. 2.21. On the ground station RX side, a 3.7 m of commercial-of-the-shelves parabola antenna is utilized. The RX antenna has 35 dB/K of G/T. After multiplying the received signal by the Boltzmann constant, a carrier-to-noise ratio of 124.5 dBHz is achieved. Now the signal SNR can be calculated by applying noise bandwidth from the symbol rate information, which is 4.0 GHz. The SNR of the received signal is 28.5 dB. The above calculation can be summarized as:

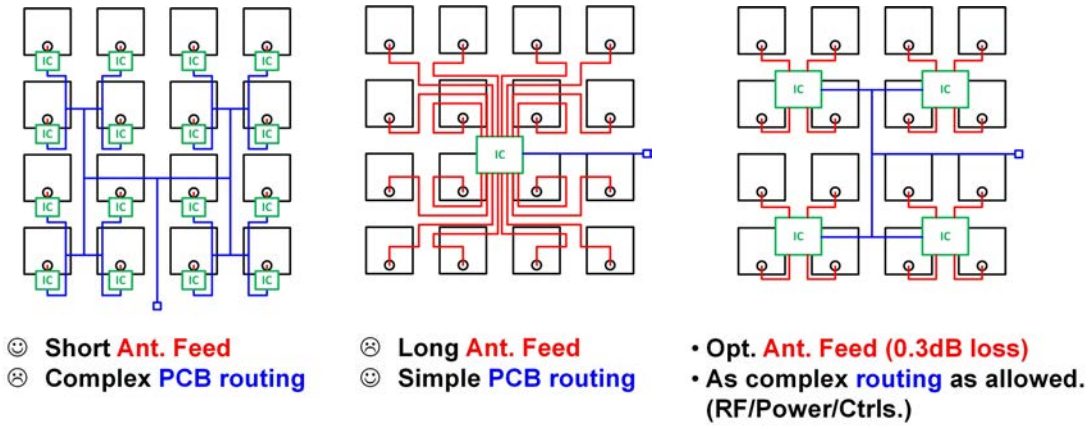

(a) (b) (c)

Figure 2.22: Conceptual diagram of antennas and RFIC (a) 1:1 Antenna/RFIC drive ratio, (b) 16:1 Antenna/RFIC drive ratio, and (c) 4:1 Antenna/RFIC drive ratio.

$$\frac{S}{N} = P_{TX} + G_{TX} - FSPL - L_{sum} + G/T_{RX} - 20\log_{10} k - 20\log_{10} R_S \tag{2.36}$$

where, S/N is the SNR of the received signal, P_{TX} is the output power of a single PA, L_{sum} is other additional losses except for FSPL, G/T_{RX} is the RX antenna figure of merit (FoM), R_S is the signal symbol rate for noise calculation, and G_{TX} is the TX array gain. G_{TX} can be represented as below:

$$G_{TX} = 20\log_{10} N \tag{2.37}$$

where N is the number of the element antenna in TX.

The above link budget reveals that the received SNR, 18.5 dB can support the highest modulation scheme in DVB-S2X standard which is 256-APSK with 3/4 code rate [49]. Targeting to support the DVB-S2X standard, the required PA output power and the number of elements are 6 dBm and 4096, respectively, under 585 km LEO, 10° elevation angle, and 4GHz symbol rate conditions.

2.3.2 Element Integration Level

Not only the number of element of an array, but also how many elements are integrated into IC or antenna/radio frequency integrated circuits (RFIC) drive ratio is one important consideration. Figure. 2.22 shows three different scenarios upon different antenna/BFIC

Specification	Value
Link Speed	64 Gbps
EVM@4GBaud/DP	27 dB
EIRP	48 dBW
DC Power	500 / 250 W (DP / SP)
Areal Stow Rate	1/16
TX Weight	0.1 kg
Power Efficiency	>15% / -50°~+50° Scan

Figure 2.23: Summarized quantitative targets.

drive ratio of the RFIC. As compared in Figure. 2.22(a) and Figure. 2.22(a), depending on the antenna/BFIC drive ratio, the complexity and length of the routings between antennas to an RFIC (output routings) and the complexity and length of the routings between an RFIC and system input (input routings) vary in opposite direction. Here input routing contains RF distribution lines to RFIC, digital control lines, and power distribution lines, and the output routings includes antenna feed lines.

If the antenna/RFIC drive ratio is 1:1, minimum rate, the length of the output routings is the minimum, while the length of the input routings become the maximum. In this scenario, the lowest output loss which is critical to the output linearity and TX efficiency is expected. However, complexity of the input routing becomes the maximum. The complex input routings including input RF distributions, control lines, power supply lines may require a number of layers of substrate. A number of layers results in cost increase and fabrication inaccuracy. In other hand, If the antenna/RFIC drive ratio is high, say 16:1 as shown in Figure. 2.22(b), the complexity of the input routings is mitigated, while output routings, antenna feed lines become long and complex. The long and complex antenna feed lines may cause huge loss and coupling between lines.

The above discussion derives one optimization rule: As short output routings as possible under input routings are allowed by process design rules. With the optimization rule, the antenna/RFIC drive ratio is set to 4:1 as shown in Figure. 2.22(c) in this thesis. The single output antenna feed line may consist of two lines for dual polarization signaling or a single line for single polarization.

2.3.3 TX Design Target

The quantitative targets from previous discussion are summarized in Figure. 2.23. Setting the link speed as maximum which can be exploitable from the 27-31 GHz DVB-S2X communication, required EVM is set to 27 dB under dual circular polarization transmit-

ting mode. From the required EVM, EIRP and allowed DC consumption at dual circular polarization mode are decided as 48 dBW and 500 W with 4096-element active phased array, respectively. Likewise, single circular polarization mode DC consumption is set to 250 W. To stow the 4096-element size array into 1U small-sat, required areal stow rate is required to be 1/16. Lastly, total TX weight is set to 0.1 kg and the power efficiency over the steered beam angle (-50 +50°) is set to >15 %.

Finally, the summarized research background is demonstrated in Figure. 2.24 including realized techniques to achieve quantitative research targets. The first is to implement dual circular polarization. To realize dual circular polarization, a comprehensive understanding of polarization is required. The second is to design the Ka-band phased-array TX in CMOS technology, which requires elaborate modeling at high frequency and careful measurement to evaluate the TX. Furthermore, systematic-level design with PCB is also required with full 3D electromagnetic simulation. The third technique involves developing of Ka-band CMOS phased-array TX to a deployable substrate. The fourth technique is the use of a load tuner, which will be introduced in Chapter 4. The load tuner can adjust the load impedance against the deteriorated antenna impedance caused by element coupling and beam steering, thus improving efficiency. Improved efficiency, under the given RF output power, leads to reduced DC power consumption. Next, a clever circularly polarized signal can further reduce TX DC power consumption. Considering all of the above, a systematic array design that minimizes loss while maximizing array gain will be explored to reduce the total DC power consumption.

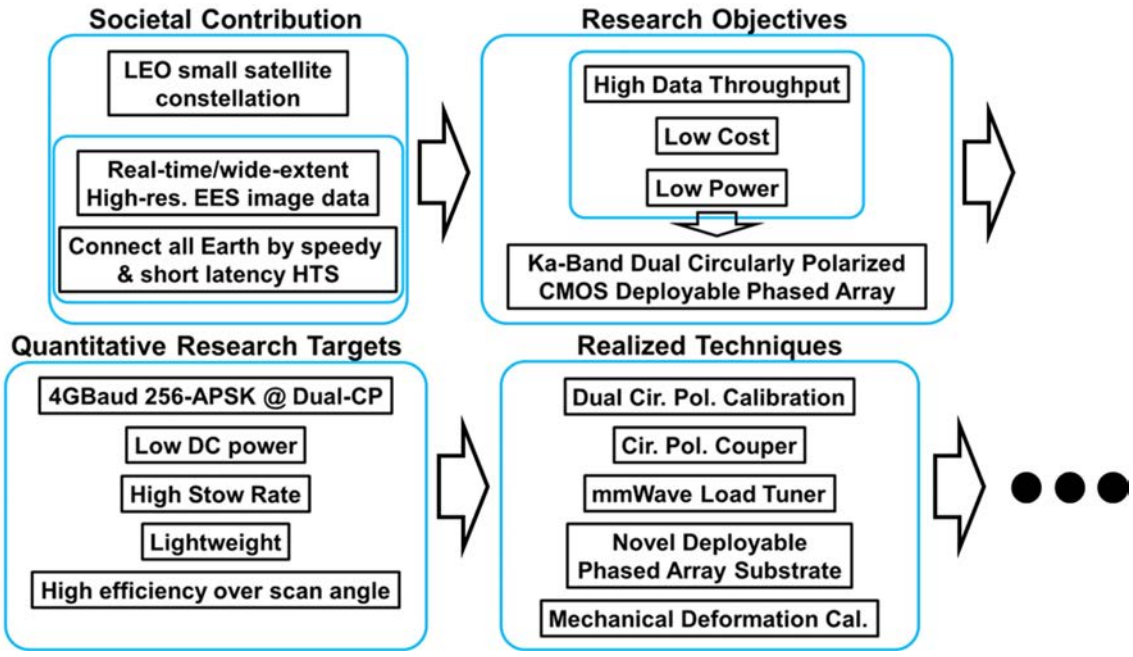

Figure 2.24: Relationship diagram between the challenges to the LEO small satellite and research objectives.

Chapter 3

Space-Efficient Deployable Phased-Array

This chapter discusses Ka-band CMOS deployable phased array TX. Specifically, for implementing the deployability, this chapter concentrates on how to build the deployable substrate for TX integration. In Section. 3.1, the concept of the deployable phased array, and the prior arts will be presented. After that, the practical deployable phased array implementation will be discussed in the Section. Because this chapter focuses on how deployability is implemented, details on deployable PCB and RF components on the PCB will be addressed rather than active ICs. 3.2. Finally, measurement results and the summary of the chapter will be deliberated on in the Section. 3.3 and 3.4.

3.1 Introduction

3.1.1 Deployable Phased Array

As depicted in Chapters 1 and 2, one of the most crucial concerns in the satellite business is the exorbitantly high launch cost. To reduce costs as much as possible, every component in satellites must be minimized in volume and weight. However, antennas are a component that has performance dependent on their size. In terms of transmission (TX), a larger antenna size is preferred in order to focus the radiated power, which would otherwise spread out in all directions. Conversely, in terms of reception (RX), larger antenna size is preferred in order to collect small radiated signal energy that is spread out over the air. Specifically, for space applications, communication distances are too great to establish communication links with small antennas. These two conflicting factors result in a trade-off between antenna size and satellite cost.

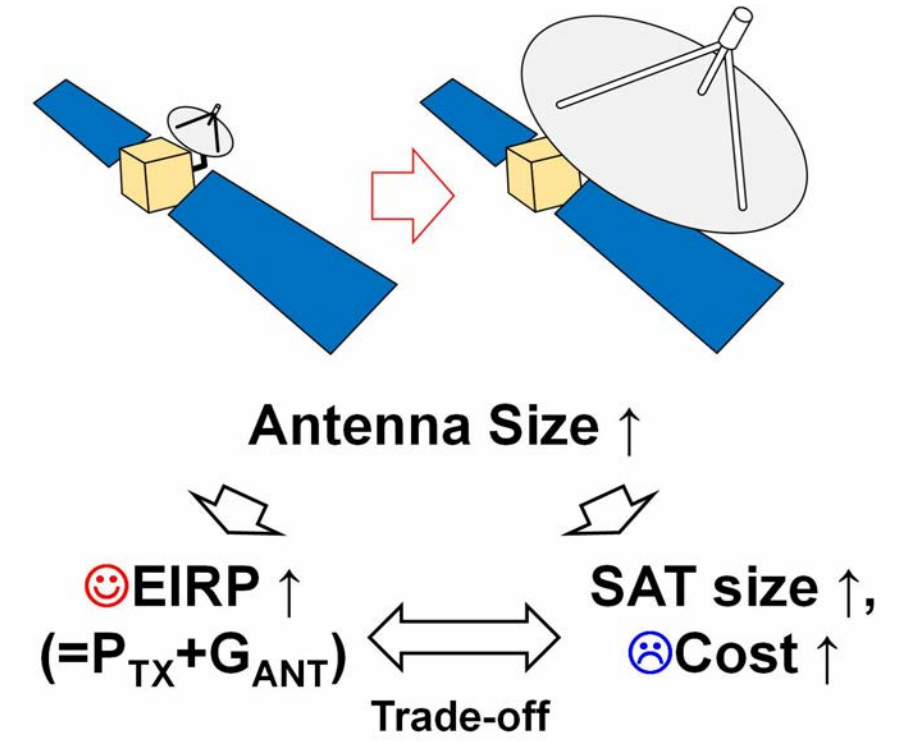

(a)

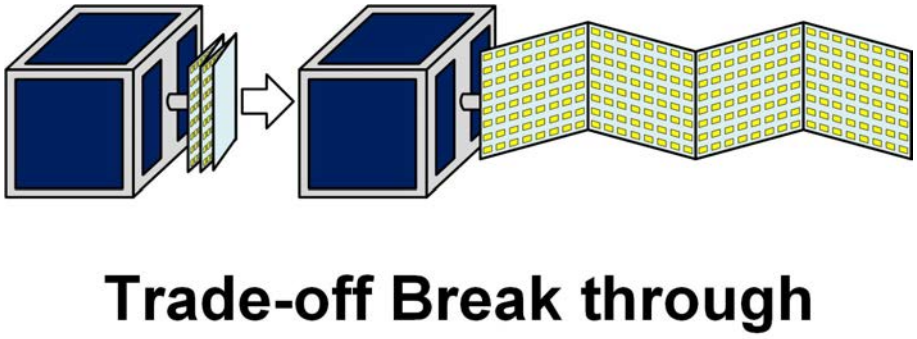

(b)

Figure 3.1: (a) Trade-off between cost and EIRP in antenna on satellites, and (b) break-through of the trade-off with the deployable array antennas.

The Figure. 3.1(a) explains the trade-off relationship between antenna size and satellite cost. Especially, in terms of the TX, antenna size is directly related to the EIRP. Thus, the trade-off was re-visited as the relationship between EIRP and satellite cost. To break through the trade-off, as an old solution, deployable antennas are well developed as shown in Figure. 3.1(b). By doing so, a satellite with folded antenna can be launched at a reasonable cost, and deploy the antenna for higher EIRP.

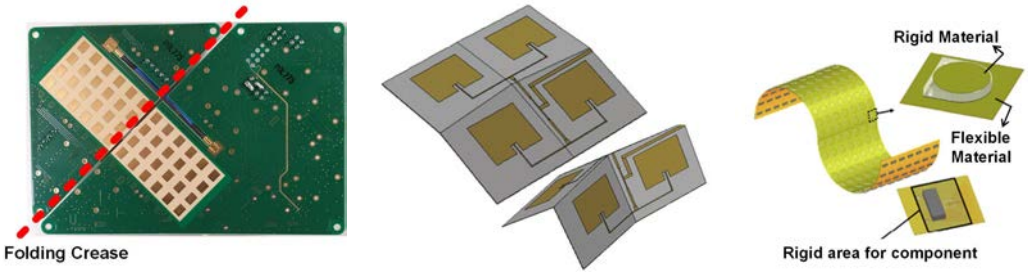

(a) (b) (c)

Figure 3.2: Conventional deployable antennas:(a)Two rigid substrates [2], (b) Fully flexible substrate [3], and (c)hybrid rigid-flex substrate [4].

	Advantages	Disadvantages
This work	•Strong IC solder against fold •No process error in rigid-flex integration •Light weight •Multi-layer PCB → adequate for larger array	
Two rigid substrate	•Strong IC solder against fold •Less process variation	•Difficult to scale to large array •Heavy weight
Fully flexible substrate	•Light weight	•IC solder defect by fold •Two layers PCB → inadequate for larger active phased-array
Hybrid rigid-flex substrate	•Strong IC solder against fold	•Process error in rigid-flex integration •Two layers PCB → inadequate for larger array

Figure 3.3: Comparison of conventional deployable array antennas.

3.1.2 State-of-the-Arts

There has been significant research regarding deployable array antennas with various types of deployability [2–4, 56–67]. As shown in Figure. 3.2, three different types of deployable antennas can be selected as representative deployable structures. One approach is to implement deployability with two rigid substrates fixed on a flexible membrane [2]. This structure offers the advantages of rigid substrates, such as multi-metal layers, low-loss substrates, less process variation, and a mechanically solid and stable footprint for IC

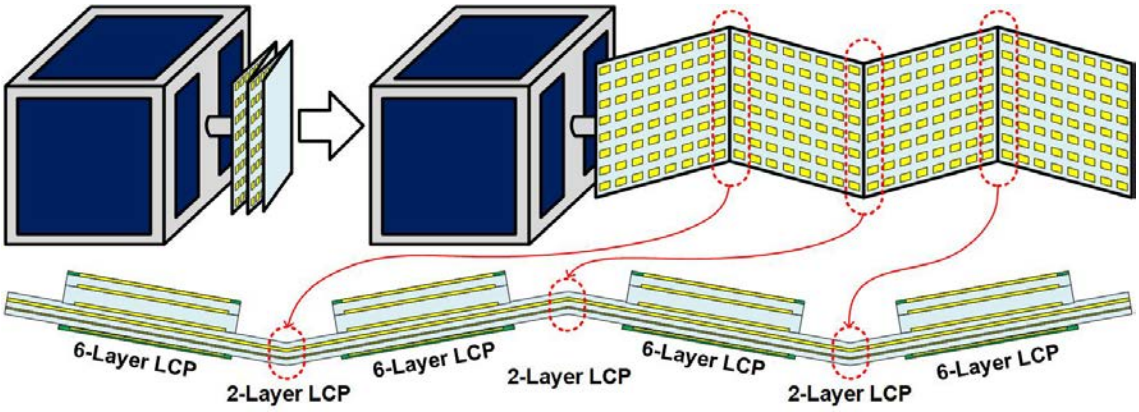

Figure 3.4: Proposed deployable phased array antenna structure.

soldering. However, this type of substrate cannot be scaled up to a large array, and it is also relatively heavy. Another approach is to use a fully flexible substrate [3]. This type of antenna array is straightforward to build and is lightweight. However, arrays on a fully flexible substrate cannot provide solid IC soldering footprints and enough multi-metal layers to integrate many control routings for an active phased array. These disadvantages make it challenging to build large-size active phased arrays. The third approach is to utilize hybrid rigid and flexible substrates [4]. This structure combines the advantages of both rigid and flexible substrates, offering solid and stable IC soldering footprints, convenient crease formation, and a wide patch-to-ground gap for patch antenna design. However, hybrid rigid-flex substrates have a significant challenge: the process variation is too significant to implement mm-wave frequency TX building blocks. Additionally, the work in [4] does not have a sufficient number of metal layers for active phased array implementation. The comparison between three types of deployable array antennas is summarized in Figure. 3.3.

3.2 Deployable Phased Array Implementation

3.2.1 Phased Array Architecture

Figure. 3.4 illustrates the proposed substrate structure for a deployable active phased array TX. The substrate is composed of LCP and copper metal layers. The place for the IC soldering and antenna implementation is manufactured with 6-layer substrate. The place for the foldable crease is manufactured with 2 layers of LCP substrate. Two different numbers of layers are implemented by laminating different sizes of the LCP substrates composing a hetero-segmented LCP substrate. The 6-layer substrate has a wider substrate thick-

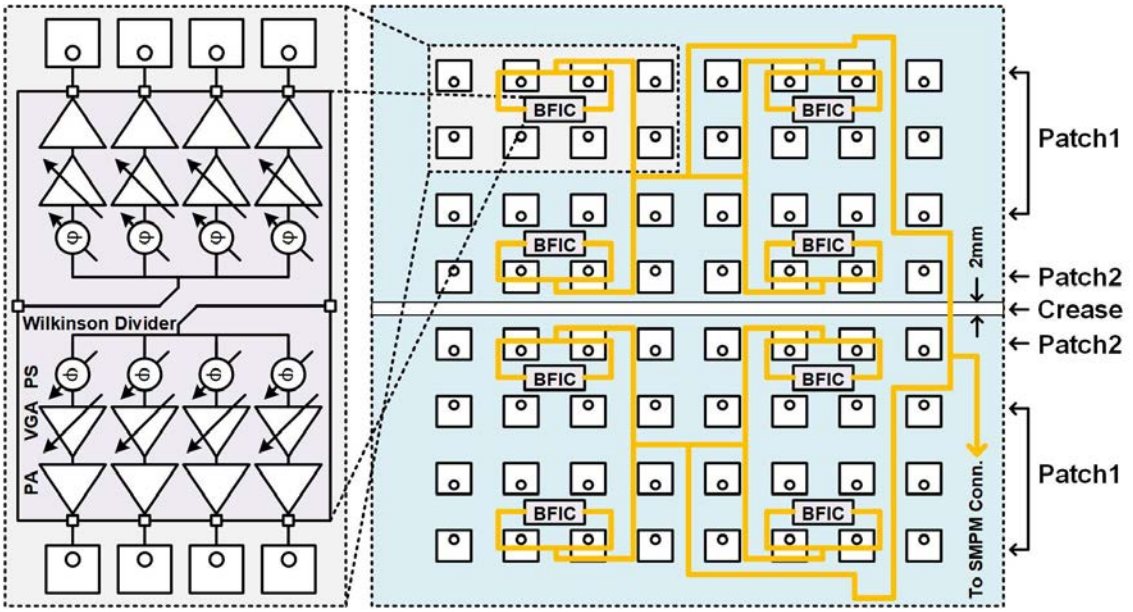

Figure 3.5: Architecture of the proposed deployable phased-array TX on the hetero-segmented LCP substrate.

ness in patch antenna side layers for higher antenna efficiency and wider bandwidth. The hetero-segmented LCP substrate can achieve solid and stable IC soldering footprints, less process variation unlike rigid-flex fabrication, lightweight, and multi-metal layers for handling the large active phased array control signals. By solving all the disadvantages of the aforementioned conventional deployable array antennas, the proposed hetero-segmented LCP substrate displays remarkable achievements. The advantages of the deployable arrays on the proposed hetero-segmented LCP substrate are summarized together with the conventional deployable array antennas in Figure. 3.3.

The Architecture of the proposed deployable phased-array TX on the hetero-segmented LCP substrate is shown illustrated in Figure. 3.5. For the proof of concept, an 8×8 element array is constructed. Eight antennas are driven by a single beamformer IC (BFIC). The BFIC in [8] is adopted for the active phased array functionality implementation. The BFIC is originally designed for dual circular polarization. Because of that, the BFIC has two independent inputs. However, in this proof of concept, two inputs are tied together with a power divider to prove the phased array on the proposed hetero-segmented LCP substrate without implementing a circular polarization scheme. The antennas and BFICs are integrated on the 6-layer substrate which is highlighted in cyan color in Figure. 3.5. The RF power distribution lines are also drawn in the 6-layer substrate avoiding passing the 2-layer substrate as possible. In the proof-of-concept phased-array TX, the RF distribution lines pass the 2-layer substrate only once. At the input of the distribution lines, a

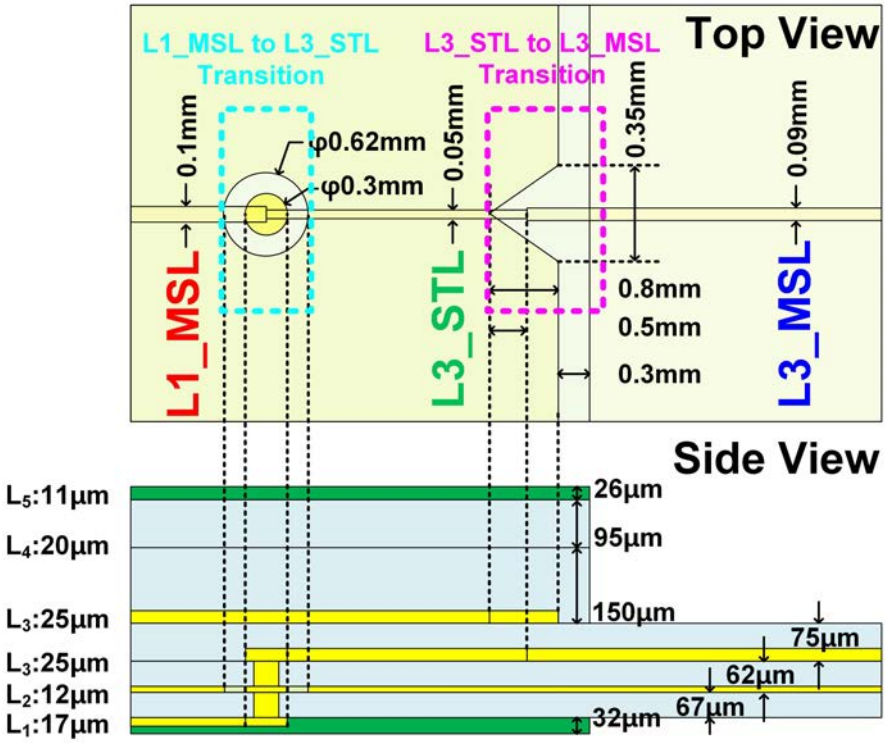

(a)

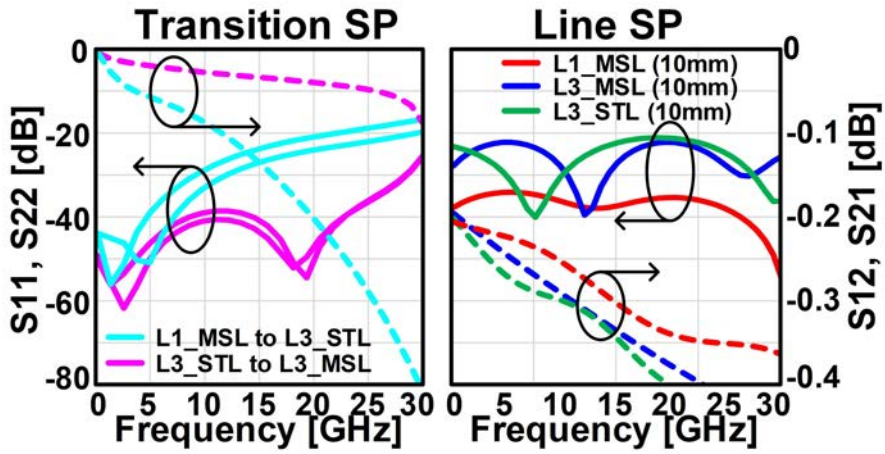

(b)

Figure 3.6: Designed RF lines: microstrip line on L_1, stripline on L_3, and microstrip line on L_3 (a) 3D model, and (b) simulation results.

small form factor of an SMPM connector is integrated not to interrupt deployability.

3.2.2 RF Components on the Hetero-Segmented LCP Substrate

Although active beamforming integrated circuits (BFICs) play a crucial role in conducting phase shift and gain variation of signals in each element of the active phased-array transmitter, they are not critical components for implementing deployability in the deployable phased array. To achieve deployability, a flexible or foldable substrate is necessary, and on-PCB RF blocks are essential for combining and distributing RF signals to the active BFICs. Therefore, careful design of on-PCB RF blocks is crucial for the successful implementation of a deployable phased array. This subsection presents about the designs of RF distribution lines, and antenna patch designs.

Figure. 3.6 illustrates three different types of RF distribution lines that are distinguished by color. The first line is a microstrip line (MSL) on the L_1 layer, referred to as L1_MSL. These lines are used for antenna driving by BFICs, and the signal patterns are on the L_1 layer, while the ground plane is on the L_2 layer. High frequency simulation software (HFSS) is used to evaluate the designed L1_MSL, which has a line width of 0.1 mm. The second RF distribution line is a stripline (STL) on the L_3 layer called L3_STL in short. The L3_STL consists of an L_3 signal line and two ground planes, and the designed line width is 0.05 mm, with the line being sandwiched by two L_2 and L_4 ground planes. The third line is the L3_MSL on a 2-layer substrate. Although the signal line of this line is patterned in L_3, it forms a microstrip line structure in the absence of L_1, L_4, L_5, and L_6 layers, as shown in the lateral view of the board in Figure. 3.6(a). The designed line width of the L3_MSL is 0.09 mm. The two lines on L_3 are used for input RF signal distribution to the BFIC from the input SMPM connector. Two lines are also designed for switching between two different substrates, the 2-layer substrate, and the 6-layer substrate. When the signal running on the L3_STL on the 6-layer substrate encounters the 2-layer substrate, the signal layer does not change, while only one of the two ground planes disappears. To prevent increasing return loss due to the abrupt line cross-section shape change, signal transition structures are also designed. The 3D models of the L3_MSL-to-L3_STL and L3_STL-to-L1_MSL transition structures are shown in Figure. 3.6(a). In the L3_MSL-to-L3_STL transition design, the L_3 ground plane is cut in a triangular shape to distribute the electrical field smoothly. In the L3_STL-to-L1_MSL transition design, L_1 to L_3 via is used, and the L_2 ground hole diameter size is carefully selected to emulate a coaxial-like structure. The simulation results of the two transitions and three lines are presented in Figure. 3.6(b), which shows well-matched and low transmission loss performances.

In addition to the challenges posed by the RF distribution lines, the patch antenna design in a hetero-segmented LCP substrate presents another difficulty. Due to the inconsistent distribution of the substrate's geometry, the antennas located far from and near the

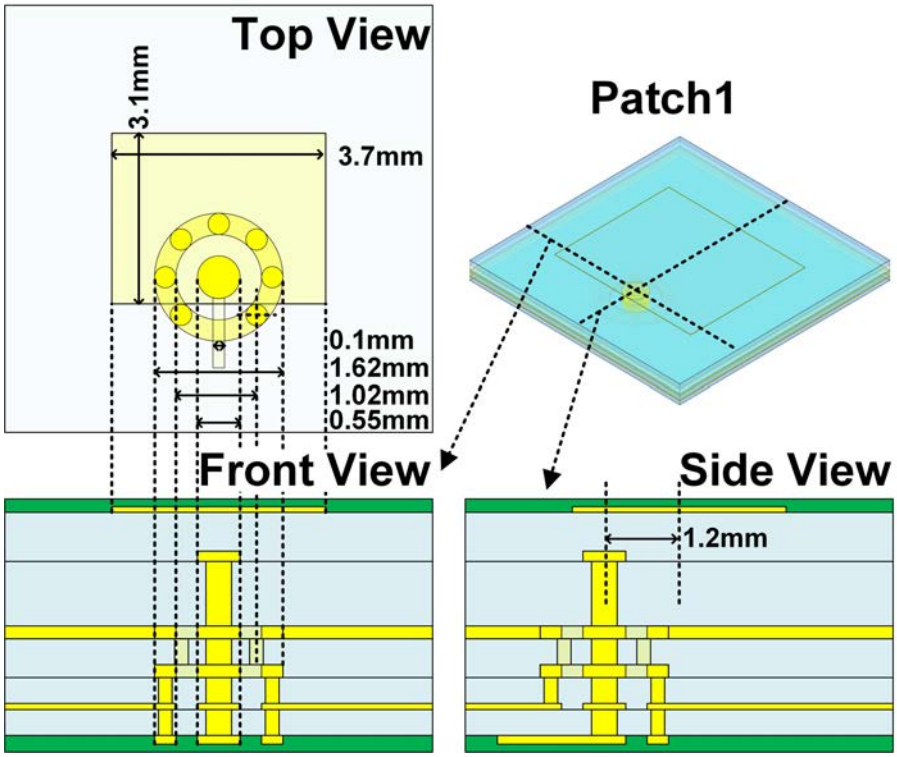

(a)

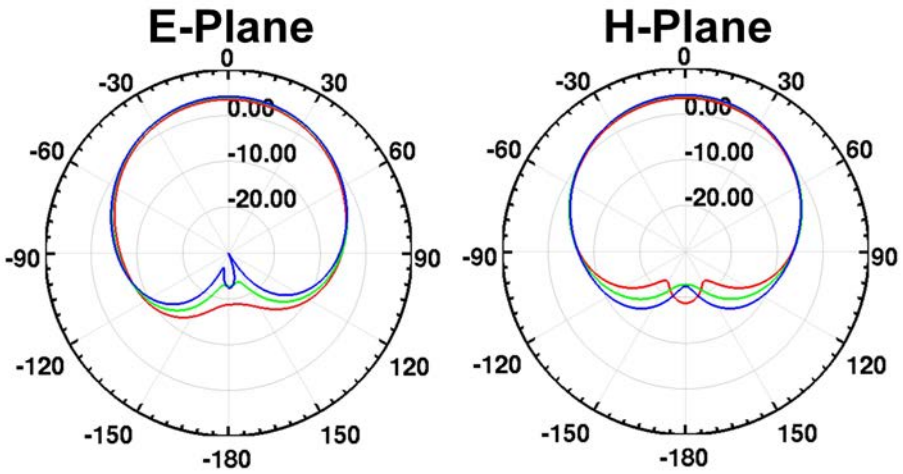

(b)

Figure 3.7: Designed patch antenna far from the crease (a) 3D model, and (b) simulated antenna gain in E-plane and H-plane.

geometry change exhibit different characteristics. For example, on a 2-layer substrate, the patch located far from the crease is called patch1, while the one located near the crease is called patch2. This inconsistency can result in degraded return loss and antenna gain pattern. Therefore, a careful RF electromagnetic simulation is required, and an HFSS unit

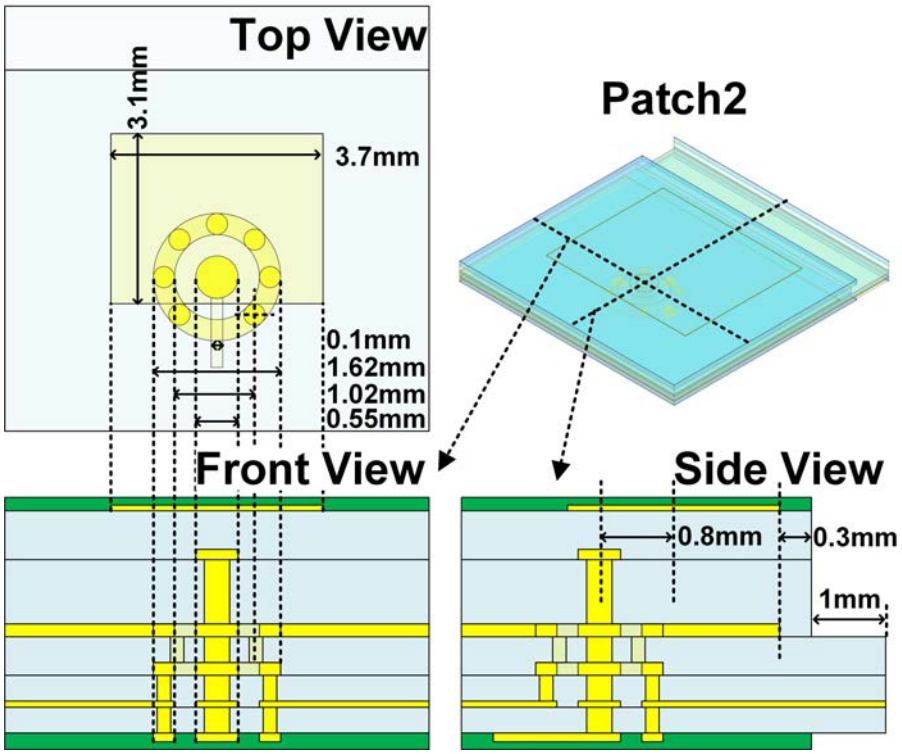

(a)

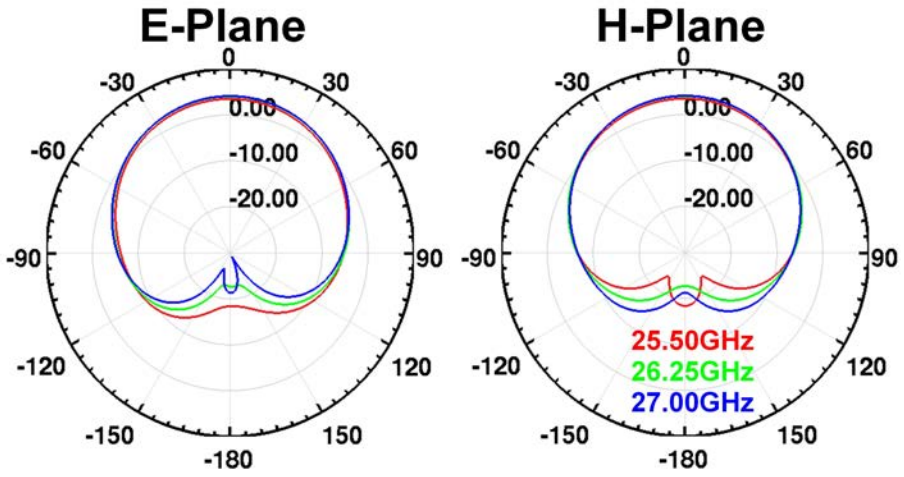

(b)

Figure 3.8: Designed patch antenna near the crease (a) 3D model, and (b) simulated antenna gain in E-plane and H-plane.

cell simulation is utilized. The unit cell simulation assumes that a unit cell is periodically deployed, thereby assuming an infinite array. This simulation takes into account the adjacent field coupling between elements. Figures 3.7(a) and 3.8(a) show the 3D models of the two designed patch antennas. Both antennas are designed to be fed using the proxim-

ity coupling feed methodology. The signal comes from L1_MSL and is connected to the L_1-to-L_5 via. At the end of the via on the L_5 side, there is a 0.55 mm diameter via land metal pattern. The signal couples to the L_6 patch pattern from the L_5 land pattern. Around the L_1-to-L_5 via, L_2, L_3, and L_4 form a circular ground ring to emulate the coaxial-like shape for the 50 Ω matching. Not only the circular ground ring pattern, but the vias between L_2-to-L_3 and L_3-to-L_4 also surround the L_1-to-L_4 via. As discussed, the antenna in Figure. 3.8(a) has a 1 mm back-off defect in the substrate on the right side, which causes differences in gain and matching. To compensate for these differences, the location of the feeding vias is slightly adjusted. The feeding via for patch1 is located 1.2 mm away from the patch center, and the feeding via for patch2 is located 0.8 mm away from the patch center. The simulated results are shown in Figures 3.7(b) and 3.8(b), taken at 25.5 GHz, 26.25 GHz, and 27 GHz, as the utilized BFIC is designed for EESS downlink band. As can be seen, both antennas show the same gain values in both the E-plane and H-plane.

3.2.3 Calibration of the Crease

After the deployable substrate is folded, a crease remains which may not be completely restored to a flat surface after deployment in space, and the angle of the crease can be random. The random angle makes it difficult to predict, and thus calibration of the crease is required.

In Figure. 3.9, a simple one-dimensional phased array diagram is shown for understanding the phased array calibration. As the designed deployable phased array TX has a single crease, the conceptual diagram also has a single crease. To calibrate the phased array, first, two sub-arrays divided by the crease must be well-calibrated and well-controllable phased arrays. This operation can be done on the ground in the measurement room before launching into space. For the calibration, the rotating-element vector (REV) algorithm [68] can be utilized. After the deployment of the antenna in space, the REV algorithm can be used again for further calibration.

For the mathematical details, let's say the beam angle to the test receive antenna of the left-side sub-array and right-side sub-array be α_L and α_R, respectively. Because

$$\begin{aligned} \alpha_L &= \delta + \alpha \\ \textit{and} \quad \alpha_R &= \delta - \alpha, \end{aligned} \tag{3.1}$$

The α and δ can be solved. Here, the α is the direction to the test receive antenna from the flat-state full array. Because the α is the direction to the test antenna, for real communication operation, the α is a redundant parameter for the beam steering. In communication and beam steering, only the δ is added or subtracted from the wanted beam angle at each

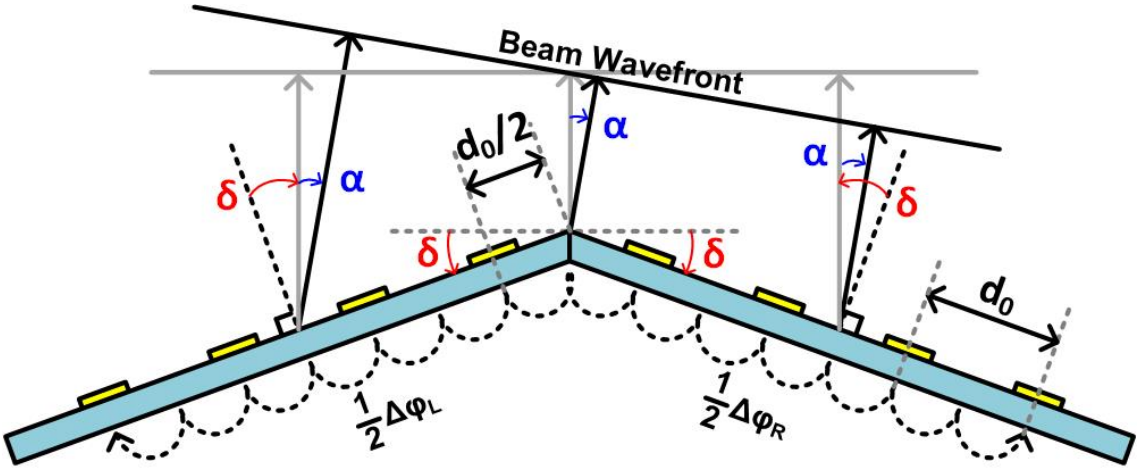

Figure 3.9: One-dimensional phased array diagram for comprehensive calibration understanding.

left and right-side sub-array. In this way, phased arrays with more than one crease can find their crease angles and be calibrated.

Here is the summarized calibration algorithm.

- Each sub-array turns on and steers the beam until the test antenna measures the highest power.
- Save each beam angle that achieves the highest receive power: $\alpha_L = \delta + \alpha$, $\alpha_R = \delta - \alpha$.
- Find δ from the Equation. 3.1
- apply crease angle δ to the wanted beam direction.

One more important consideration in calibration is calibration time. For calculating the calibration time, a 4×4 array consists of 16×16 sub-array, thus a 64×64 array in total, is assumed. In addition to the array size configuration, beam switching speed for a sub-array is set to 38 msec from SPI command write time. Lastly, assuming each sub-array sweeps beam by 30 steps of azimuth angle and 30 steps of elevation angle, totally 900 steps are taken into account. The calibration time can be derived as below.

$$t_{CAL} = t_{Beam-sub} \times \#\ of\ beams \times \#\ of\ subarrays = 9\ mins. \tag{3.2}$$

Here, $t_{Beam-sub}$ is the sub-array beam switching time, 38 msec, # of beams are set to 900, and # of subarray is set to 16. From the above result, a single calibration time is 9 minutes.

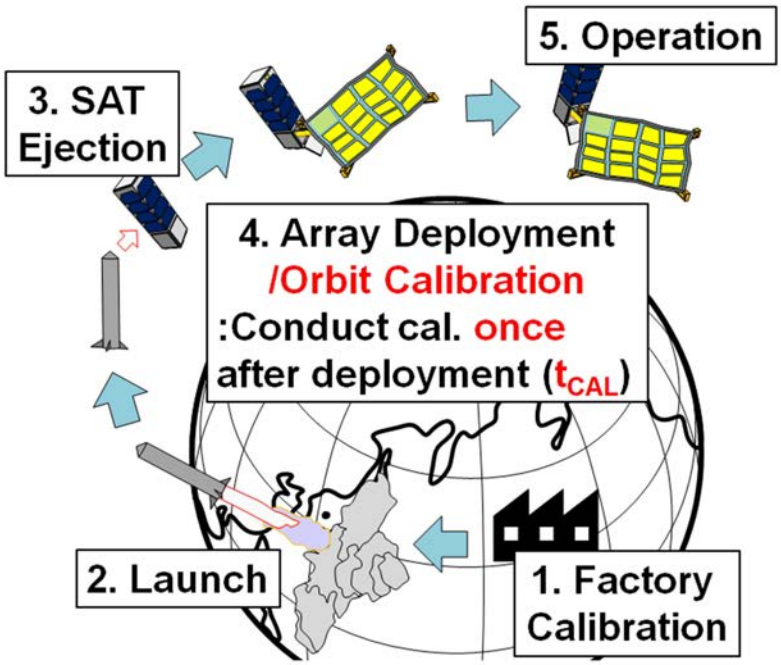

Figure 3.10: Satellite launch phases for deployable phased array.

Figure. 3.10 shows satellite launch phases including several important initial missions. After the satellite sits on the orbit, it starts deploying membrane which includes solar cells and deployable phased array. When the deployment of the flexible membrane is done, the satellite begins the calibration with external probe antenna on satellite body. As aforementioned in previous discussion, the calibration takes 9 minutes. Because there is no air in the space, once the deployment and vibration due to the deployment are finished, mechanical deformation does not change. Until the space mission is finished, calibration is not conducted anymore.

Weight Comparison LCP flexible substrate is inherently lighter than rigid substrates. Figure. 3.11 shows two different fabricated phased array on deployable substrate and Megtron 6 rigid substrate. Measured areal mass of rigid substrate is 2.96 kg/m^2 with nine layers and areal mass of flexible substrate is 0.82 kg/m^2 with six layers. While single layer thickness of each substrate is similar, comparing nine layers and xix layers substrate is not fair. For the fair comparison, nine layers substrate is normalized to six layers substrate by simply multiplying 6/9. The normalized areal mass of the phased array on Megtron 6 rigid substrate is 1.98 kg/m^2. Comparing this directly to areal mass of flexible substrate, 0.82 kg/m^2, the results tell that flexible substrate is as lighter as $\times 1/2.4$ than rigid substrate.

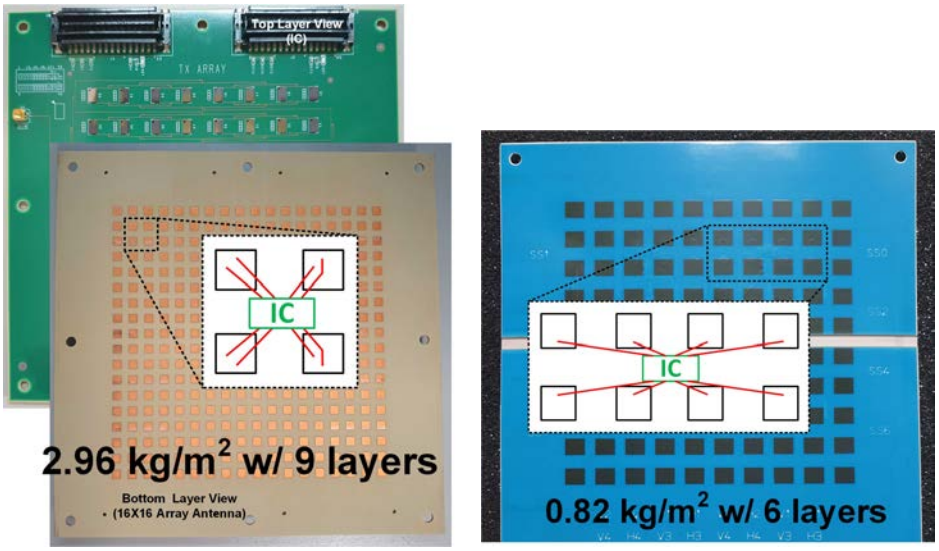

(a) (b)

Figure 3.11: Weight comparison between: (a) a phased array on Megtron6 rigid substrate, and (c) a phased array on LCP flexible substrate.

3.3 Measurement Results

To further evaluate the proposed hetero-segmented LCP deployable phased array TX, the design depicted in Figure. 3.5 was fabricated, as shown in the photographs of Figure. 3.12. Figure. 3.12(a) displays a side view of the fabricated TX in the IC, where eight BFICs and L1_MSTLs leading to the antenna feeding points can be observed. The 6-layer substrate was used to successfully route not only RF lines, but also control lines for the serial peripheral interface (SPI) and all the necessary power lines. On the other hand, Figure. 3.12(b) displays a side view of the fabricated TX in the antenna, with a 10×10 array of implemented antennas. Only the inner 8×8 array is activated by the BFICs, while the surrounding outside antennas are dummy antennas that reduce the different coupling effects in edge antennas and inner antennas. The blue area, covered by solder resist, represents the 6-layer substrate zone, and the white area represents the 2-layer substrate zone, which can be easily distinguished visually. The measured weight of the fabricated deployable phased-array TX on the hetero-segmented LCP substrate is only 9.65 g.

To demonstrate the proposed hetero-segmented LCP substrate folds appropriately, the pictures of the fabricated deployable phased array in various bent-angle states are shown in Figure. 3.13.

One of the most important functions of a phased array is beam steering, and the exact beam steering function is essential for the successful operation of the array. This is especially true for deployable phased arrays, as their mechanical deformation can affect

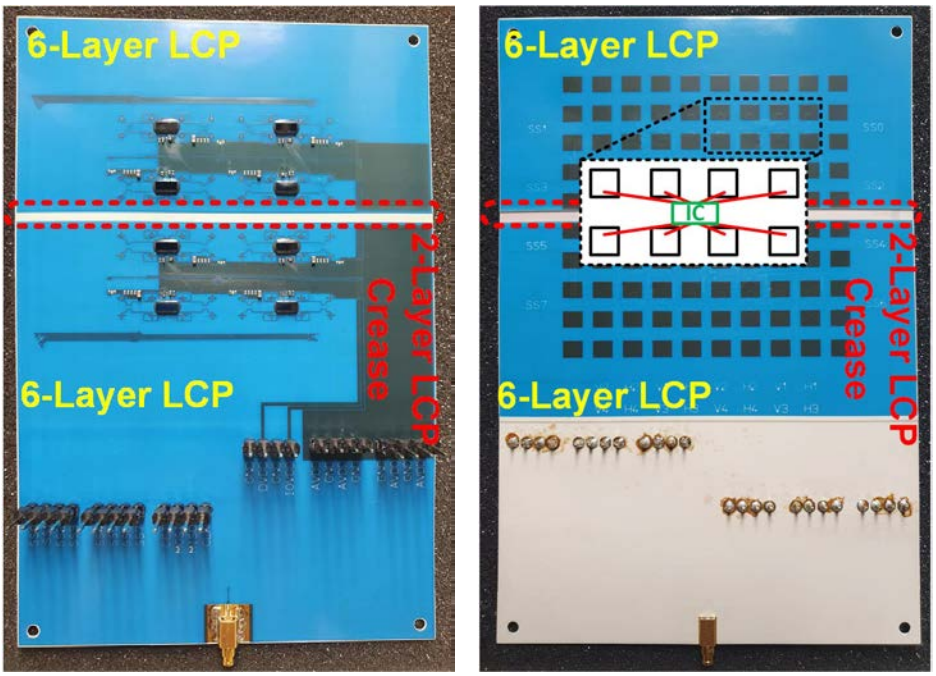

(a) (b)

Figure 3.12: Fabricated deployable phased-array TX: (a) IC-mounted side view, and (c) antenna-implemented side view.

the beam steering function, making it a major concern. In order to test the beam steering, Figure. 3.14 shows the beam patterns under various substrate bent angles: $\delta = -10°$, $\delta = 0°$, $\delta = +10°$, and $\delta = +20°$. The beam patterns in each sub-figure are distinguished by colors and were measured at -50°, -40°, -30°, -15°, 0°, 15°, 30°, 45°, and 5°. All data were measured with the above calibration. Even as the bent angle increases, causing the beam patterns at large beam angles to deviate from those at the flat state, the beams still direct towards the expected direction accurately.

One interesting observation in Figure. 3.14 is that the beam patterns are asymmetric when they are switched. The reason for asymmetric beam pattern is uneven power distribution by trace resistance. Measured power supply voltage near ICs are shown in Figure. 3.15. As shown in the figure, each chip receives power supply with ±1% variation. Because digital-to-analog converters for mosfet gate bias refer to the power supply for output signal generation, gate biases of amplifiers also changes thus bias current changes abruptly. This results in abrupt change in each element gain control a lot.

In both TX and RX phased arrays, accurate beam steering is essential, but in TX, the most critical performance metrics are the EIRP and power consumption, as the output power level of the PA determines the communication distance, which is particularly important for long-distance space applications. Figure. 3.16 illustrates the measured EIRP

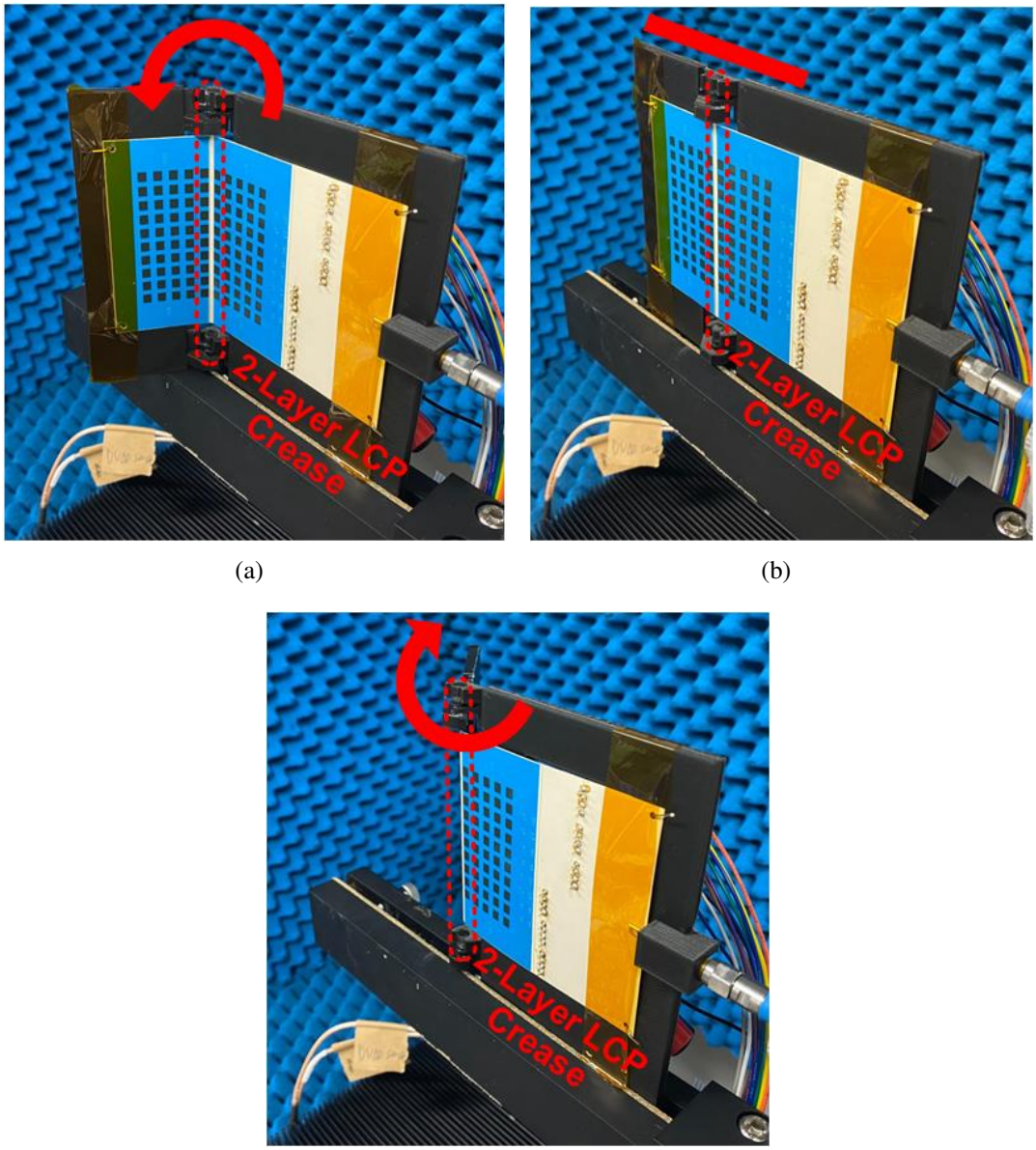

(a) (b)

(c)

Figure 3.13: Fabricated deployable phased-array TX in various bent angles: (a) bent inside the antenna surface, (b) flat state, and (c) bent outside the antenna surface.

plotted against the swept input power. The measurement shows that a saturated EIRP of 46.7 dBm is achieved with 64 elements radiating, and the power consumption at the saturation point is measured to be 4.1 W. The EIRP at the 1 dB compression point is 38.0 dBm under 2.9 W DC power consumption. The EIRP measurement is conducted at a flat state with 0° bent angle.

Not only the measured performances with a single tone but also the performances with the modulated signal are measured. Figure. 3.17 illustrates the measured EVM over

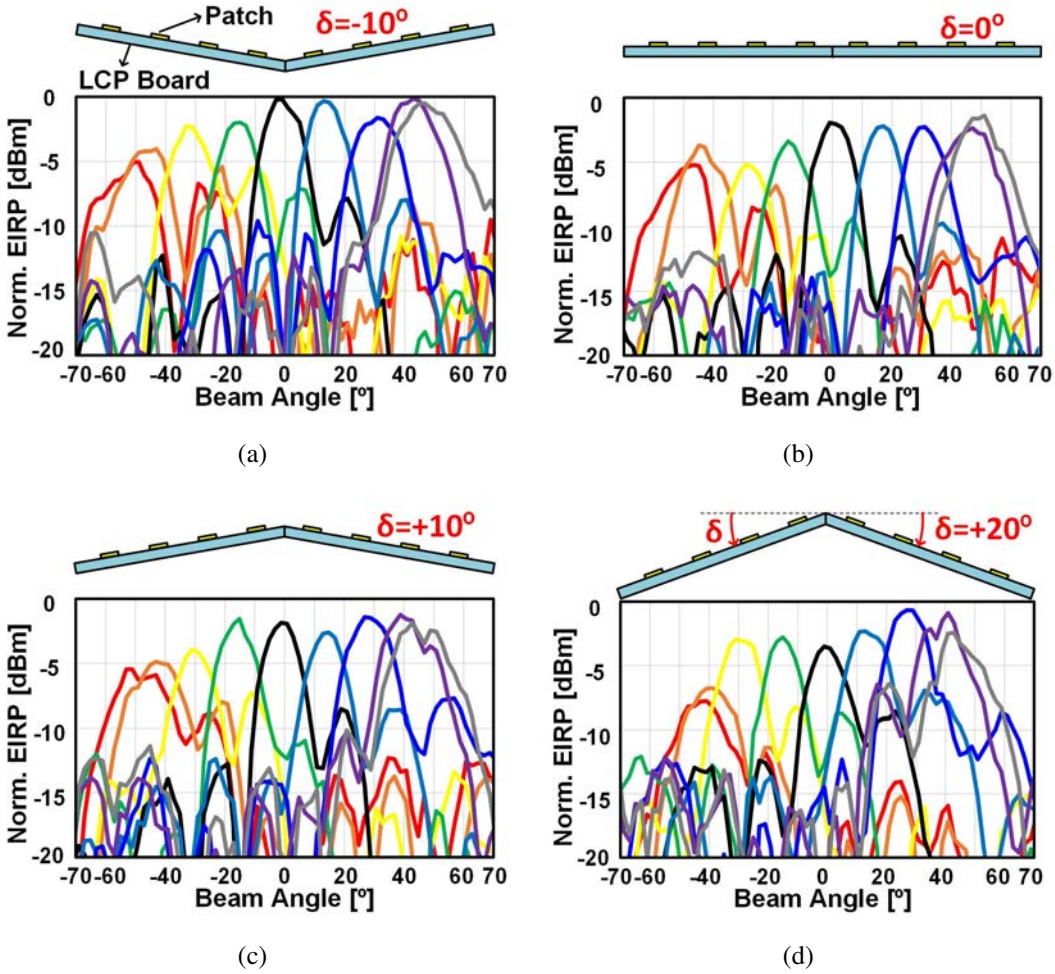

Figure 3.14: Measured beam pattern of the fabricated deployable phased array TX: (a) $\delta = -10°$, (b) $\delta = 0°$, (c) $\delta = +10°$, and (d) $\delta = +20°$.

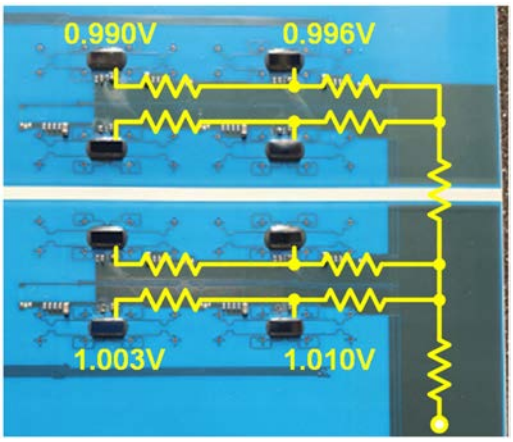

Figure 3.15: Uneven supply power distribution.

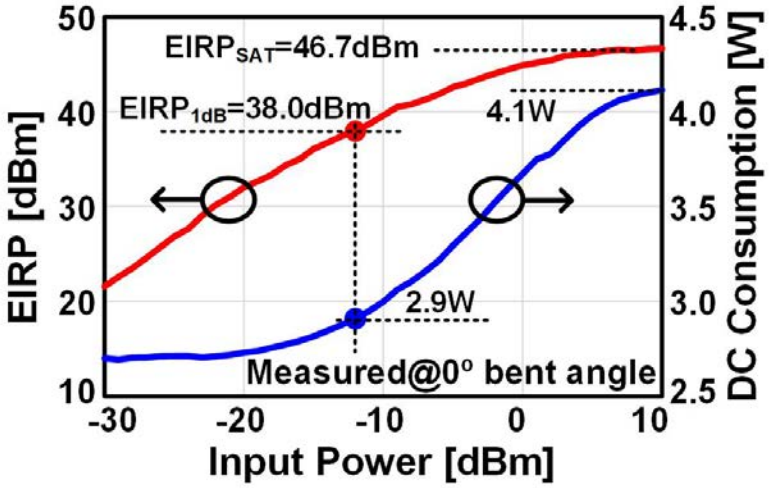

Figure 3.16: Measured EIRP along with the swept input power.

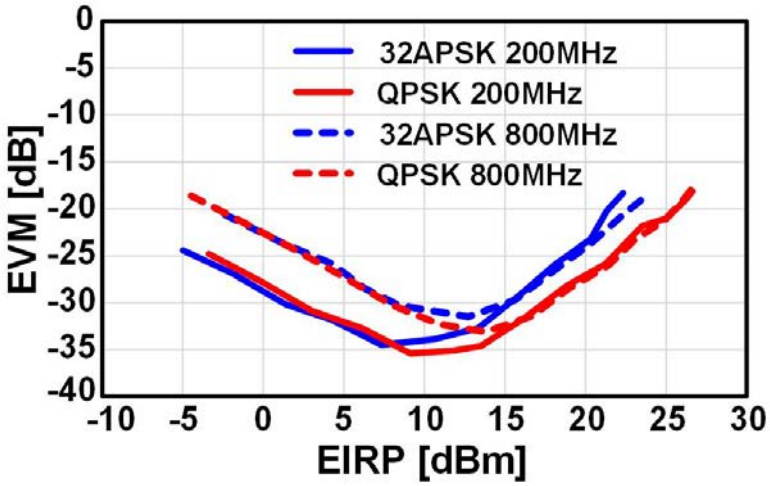

Figure 3.17: Measured EVM along with the swept EIRP.

swept EIRP and under the various modulation schemes. The EVM is measured with an 8-element array setup. From the simple calculation, the saturated EIRP in this setup is 28 dBm. There are several observation points. The first is that while the EVM decreases in a 1 dB/dB slope on the left side of the lowest EVM point, the EVM increases in a 2 dB/dB slope on the right side of the lowest EVM point. This is because, on the left side, the constant level of RX noise is dominant signal-degrading component, on the right side, the 3-dB-increasing ACPR is the dominant signal-degrading component, while the signal increase in a 1 dB/dB slope. The second is that the signals with a 200 MHz symbol rate are 6 dB as low as the signals with an 800 MHz symbol rate on the lower EIRP side. Another is, on the higher EIRP side, the EVM of the higher order modulation is higher

8-element OTA Meas. with 1500MBaud BW				
Modulation	32APSK	256APSK	QPSK	32APSK
Constellation	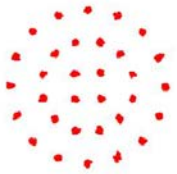			
EVM [dB]	-28.9	-28.3	-19.1	-21.6
EIRP [dBm]	13.3	12.3	23.2	22.8

Figure 3.18: Measured EVM under various modulation.

8-element OTA Meas. With 200MBaud under Bent-Board Condition				
Bent Angle, δ	0°		10°	
Beam Angle, α	0°	30°	0°	30°
Constellation		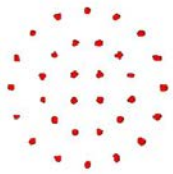	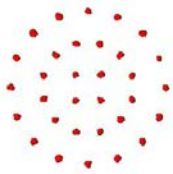	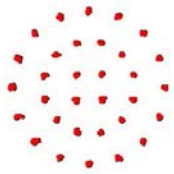
EVM [dB]	-34.6	-33.7	-34.5	-31.3
EIRP [dBm]	10.2	10.1	7.3	9.3

Figure 3.19: Measured EVM under bent-angle conditions.

than the EVM of the lower order modulation because the higher order modulation has a higher peak-to-average power ratio (PAPR). From the data, with the measurement setup, the maximum EVM is the -36 dB with a 200 MHz QPSK signal at 18 dB back-off from the saturated power point, and the -32 dB EVM is achieved with an 800 MHz 32-APSK signal at 15 dB back-off point. At the 6 dBm back-off point, -25 dBm and -20 dBm of the EVMs are achieved with QPSK and 32-APSK modulations, respectively.

The measured EVM with various modulations and a higher symbol rate of 1.5 GBaud are summarized in Figure. 3.18. At around 15 dB back-off from the saturated power level, the EVMs of 32-APSK and 256-APSK modulation are achieved at -28.9 dB and -28.3 dB, respectively. The constellations for each modulation are also shown in Figure. 3.18 and are clearly measured. At the 6 dB back-off point, QPSK and 32-APSK modulations show

EVMs of -19.1 dB and -21.6 dB, respectively. The constellations for both modulations also show distinguishable symbols.

In addition, the EVMs under various bent angle conditions were measured and are presented in Figure. 3.19. The measurements were conducted for both the board bent angle and the various beam angles. Specifically, 0° and +10° bent angles, as well as 0° and +30° beam angles, were chosen for this measurement. Despite the degradation of EIRPs at +10° bent angle, the constellations were still clear, with -34.5 dB and -31.3 dB EVMs measured at 0° and +30° beam angles, respectively.

All the measured EVM results with modulated signals are evaluated with nearest-approximation algorithm not with comparing with source symbol sets. While EVM measurement by comparing with source symbol can bit error rate (BER) because bit-decision correctness can be known, the nearest-approximation method does not provide BER measurement because the resultant symbol is decided as the closest symbol.

3.4 Summary

The proposed Ka-band 64-element deployable active phased-array TX on the proposed hetero-segmented LCP substrate achieves lightweight and small volume for the small satellites. Thanks to the new structure of the deployable substrate, which combines a 2-layer LCP substrate and a 6-layer substrate, the TX also achieved solid and stable IC soldering footprints, less process variation, and multi-layer routing for active phased arrays.

In the measurement, it is proven that the deployable phased array TX works properly at -10° to +20° board bent angle. The proposed deployable phased array TX can outputs 46.7 dBm EIRP with the 64-element array. The phased array TX supports 32-APSK modulation with a 1.5 GBaud symbol rate at 6 dB back-off from the saturated power point.

Chapter 4

Power-Efficient Load Tuner and Circular Polarization Calibration

This chapter discusses two techniques aimed at addressing the challenges faced by small LEO satellites. The first technique is the use of a load tuner in a phased array to reduce power consumption. The second technique is the dual circular polarization calibration method which addresses the impact of cross-polarization discrimination on signal quality. Section 4.1 will discuss the need for a load tuner in a phased array, followed by an explanation of how cross-polarization discrimination affects signal quality. In Section 4.3, the implementation of the load tuner for the phased array will be presented. Section 4.4 will present the dual circular polarization method. Measured results from the combination of both techniques applied to the fabricated Ka-band CMOS phased-array TX will be presented to support the presented ideas. Finally, Section 4.6 will provide a summary of the chapter.

4.1 Introduction

4.1.1 Dual Circular Polarization

In Section. 2.2, the mathematical description of circular polarization is well described and the importance of the XPD is simply introduced. In this section, the details about how XPD is related to the signal quality. For a short review of the intuitive understanding of circular polarization. Some important descriptions are summarized below.

- A single circular polarization consists of two signals that are linearly polarized in the horizontal and vertical directions, spaced 90 degrees apart in either a positive or negative direction.

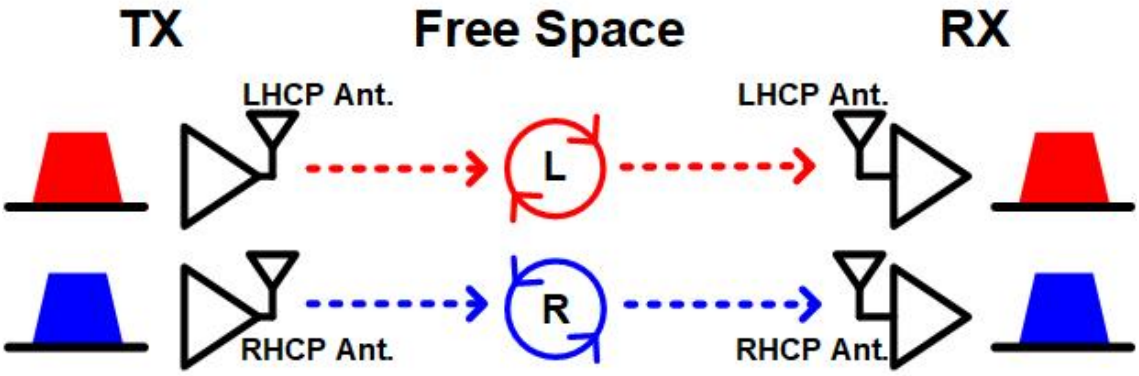

(a)

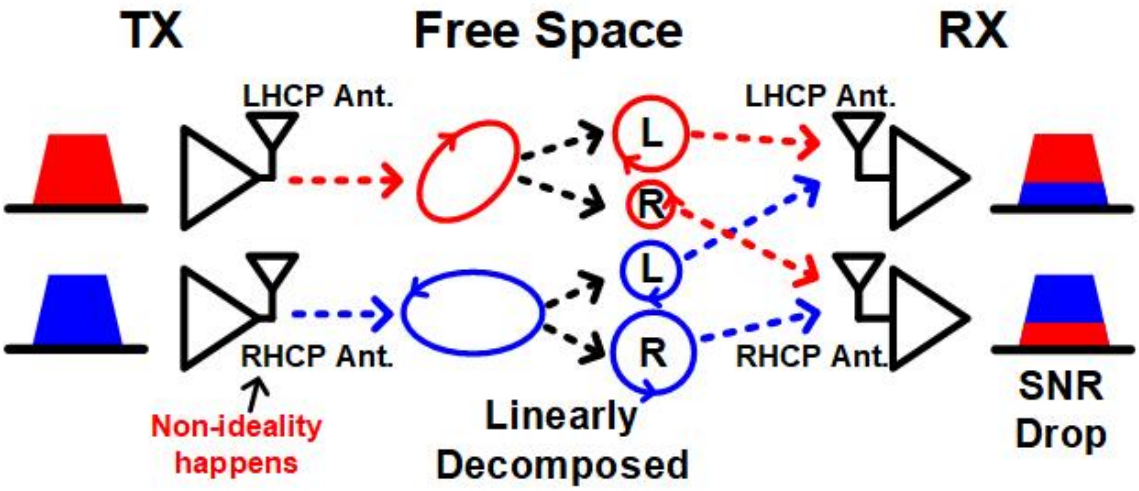

(b)

Figure 4.1: Description of impacts of dual circular polarization to signal SNR (a) ideal circular polarization, and (b) non-ideal circular polarization.

- The direction of the circular polarization is decided by the sign of the phase between two linearly polarized signals.
- The LHCP and RHCP are the new two orthogonal bases set to represent any kind of polarization, likewise the two linearly polarization do.
- The ratio of the electric field intensity of the two decomposed circular polarization is defined as XPD.

Figure. 4.1 demonstrates the impact of erroneous circular polarization on the SNR in dual polarization mode. In this configuration, the TX contains two paths for two different signals, with one antenna transmitting LHCP signals and the other antenna transmitting RHCP signals. Once the polarized signals are radiated into free space, they mix together.

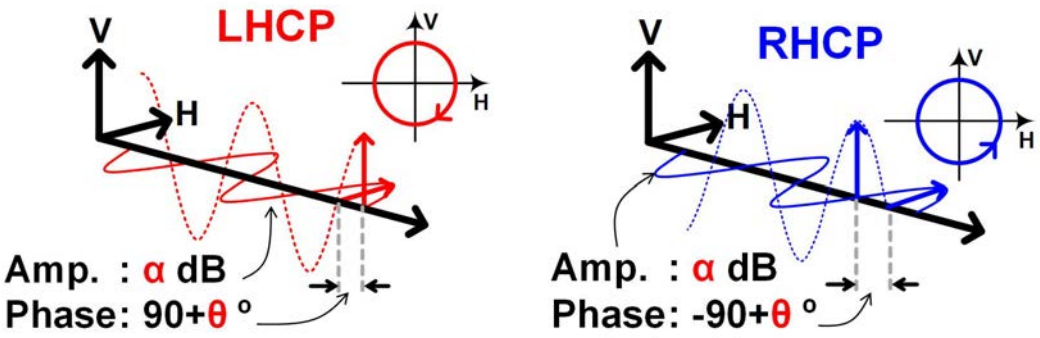

(a) (b)

Figure 4.2: Diagram for the linear combination of the (a) LHCP, and (b) RHCP.

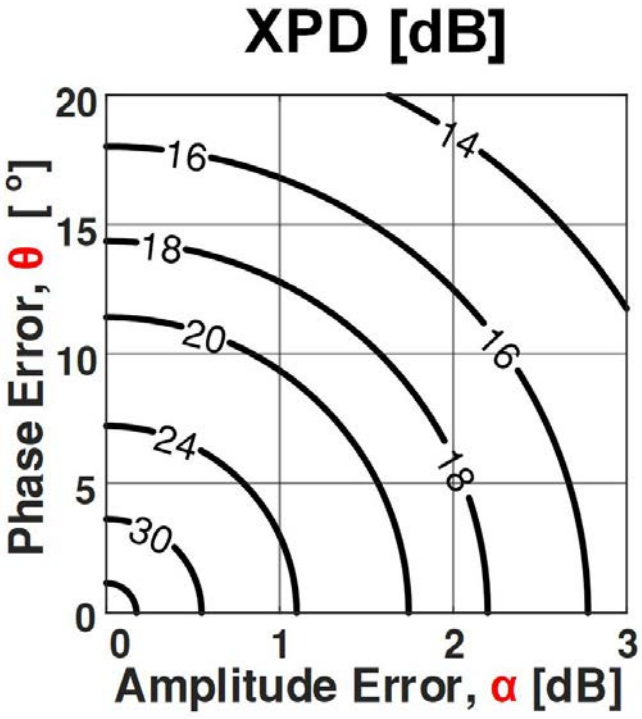

Figure 4.3: XPD contour map by the amplitude and phase error.

The ideal LHCP and RHCP RX antennas filter only their respective polarized signals. However, there are differences between ideal and practical cases, which are illustrated in Figures 4.1(a) and 4.1(b), respectively. In the ideal case (Figure. 4.1(a)), the red signal forms only LHCP, and the blue signal forms only RHCP without any unwanted components. Thus, the ideal LHCP and RHCP RX antennas can effectively filter the signal according to their polarization. In contrast, in the non-ideal case (Figure. 4.1(b)), the LHCP

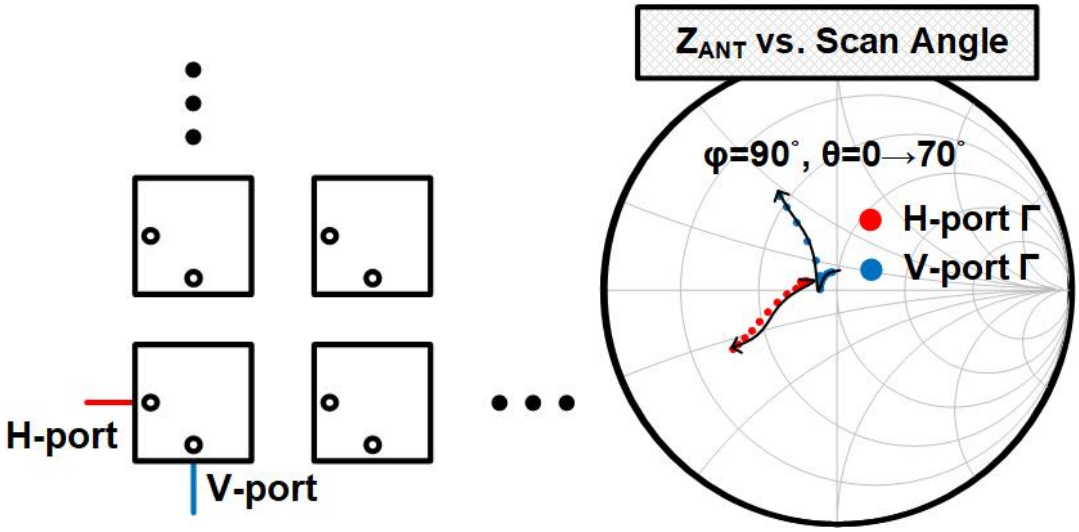

(a) (b)

Figure 4.4: Description of the load variation in a dual circularly polarized phased array: (a) antenna array diagram, (b) simulated antenna impedance of H- and V-port.

and RHCP signals become left-handed and right-handed elliptically polarized (LHEP and RHEP) signals, respectively, due to imperfect circular polarization generation by the TX. These signals can be linearly decomposed by simple mathematics into LHCP and RHCP components. As a result, the ideal LHCP and RHCP antennas cannot filter out the opposite polarization components, invoking coupling between the two signals. As shown in Figure. 4.1(b), the two coupled signals become noise or interference for the opposite polarized signal, leading to reduced SNR.

In this chapter, circular polarization is synthesized by two linearly polarized signals, so it is preferred to use parameters defined in the linear polarization sense. As a refresher, Figure. 4.2 illustrates the error parameters for circular polarization definition: α and θ. Furthermore, Figure. 4.3 displays the XPD variation in relation to the amplitude error α and phase error θ. For instance, when the errors are $\alpha = 0.5$ dB and $\theta = 0°$ or $\alpha = 0$ dB and $\theta = 4°$, 30 dB of XPD can be achieved. As explained earlier, XPD is equivalent to the SNR in dual circular polarization mode.

4.1.2 Load Variation by Phased Array Beam Steering

In addition to the dual polarization issue, load variation caused by beam steering and inter-antenna port coupling is another concern in phased array TX for small LEO satellites. As shown in Figure. 4.4, the loads at the antenna ports change significantly as the beam is steered. The antenna array with dual linearly polarized antennas is designed and simulated

Table 4.1: Comparison of load tuners in hand-held front-end and satellite phased array.

	Hand-held front-end	Satellite phased array
References	JSSC2020_Mannem [35] VLSI2019_Chappidi [69]	This work
Load variation source	Random hand-hold	Beam steering & inter-element coupling
Predictable?	Random	By simulation
Required tuning coverage	Wide (because of randomness)	Narrow (because of predictability)
Solution	Multi-stage tunable matching network	Fewer-stage tunable matching network
Loss in mm-wave	High	Low

in HFSS, where the port supporting horizontal polarization is referred to as H-port and the one supporting vertical polarization is called V-port. To emulate circular polarization, the phase difference between the two ports is set at 90° with equal amplitude. In the beam steering setup, both H- and V-ports are steered simultaneously from $\theta = 0°$ to $\theta = 70°$ with fixed ϕ. As shown in Figure. 4.4(b), the load variation due to the beam steering can greatly affect the efficiency and maximum output power of the PA, which is designed to operate at a fixed optimum load for maximum efficiency and output power. This suggests the need for a load tuner at the output of the PA.

However, designing a load tuner for a dual circularly polarized phased array encounters different challenges compared to conventional load tuners used in hand-held terminals, as reported in the literature [8, 35, 69–73]. Table. 4.1 summarizes the differences between hand-held front-end and satellite phased array load tuners.

One significant difference is the source of load variation. While antenna impedance variation in hand-held front-ends is caused by random user interactions, beam steering and inter-feeding-port coupling induce load impedance variation in satellite phased arrays. These different characteristics affect the predictability of load variation. The antenna impedance variation in hand-held terminals is random and difficult to predict, whereas, in phased arrays, the load variation can be predicted through careful electromagnetic simulation. The predictability of load variation determines the required tuning coverage during the design phase. Hand-held front-ends require wide coverage as the load variation is unknown, whereas a phased array load tuner can cover only the predicted load variation range. A wide tuning coverage load tuner design has a critical issue, however. To cover

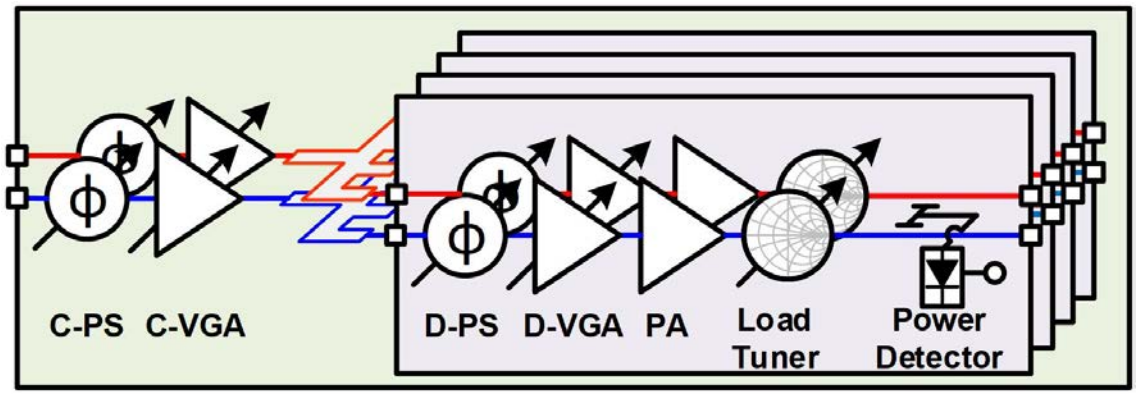

Figure 4.5: Block diagram of the proposed Ka-band dual circularly polarized CMOS TX BFIC.

the wide tuning coverage, multiple stages of tunable matching networks are required, which can be very lossy. This is especially problematic in mm-wave design, where passive component loss increases significantly due to the skin effect. Thus, a solution with fewer stages of load tuner in a mm-wave phased array is preferable.

4.2 TX Architecture and Circular Polarization Generation

4.2.1 TX architecture

Figure. 4.5 illustrates a block diagram of the proposed Ka-band dual circularly polarized CMOS TX BFIC. The TX is designed to cover the 25.5 GHz to 27 GHz frequency band which is the EESS downlink band. In a BFIC, four dual-channel TXs are implemented. A single dual channel includes two TX replicas for the H- and V-path. The two independent TXs are driven by the lumped wilkinson power divider, independently. The blocks after the output of the power divider are referred to as distributed paths (D-path) including D-PS, D-VGA, drive amplifier (DA), and PA. The path before the power divider is referred to as the centralized path (C-path) including C-PS, and C-VGA. The role of D-PS and D-VGA are used for beamforming to control amplitudes and phases of the signals from each element. The C-PS and C-VGA are for compensating the circular polarization imperfection that emerged in inter-chip variations. At each PA output, the load tuner is implemented as combined with the matching network. At the end of a single D-path, an RF coupler is implemented and a power detector reads the coupled signal to detect phase and amplitude differences between the H- and V-path.

4.2.2 Circular Polarization Generation.

By driving H- and V-ports of the dual linearly polarized antenna with the H- and V-path of a D-path, a BFIC can drive four dual linearly polarized patch antennas. With the architecture, the below two signals are driven into the H- and V-path inputs of the BFIC to generate dual circularly polarized signals.

$$A_L e^{-j90^\circ} + A_R e^{-j0^\circ} \tag{4.1}$$

$$A_L e^{-j0^\circ} + A_R e^{-j90^\circ} \tag{4.2}$$

where the A_L and A_R are the amplitudes for the signals to be LHCP and RHCP signals, respectively. The signal in Equation. 4.1 is to be entered into the input of the H-path, and the signal in Equation. 4.2 is to be entered into the input of the V-path. Because the H-port of the dual linearly polarized antenna makes a horizontally polarized signal and the V-port of the dual linearly polarized antenna makes a vertically polarized signal, the signals in the Equation. 4.1 and 4.2 are horizontally and vertically polarized, respectively. Once the signals are radiated outside the antennas, the signal term $A_L e^{-j90^\circ}$ in the Equation. 4.1 and the signal term $A_L e^{-j0^\circ}$ in the Equation. 4.2 form an LHCP signal with amplitude A_L. In the same way, the signal term $A_R e^{-j0^\circ}$ in the Equation. 4.1 and the signal term $A_R e^{-j90^\circ}$ in the Equation. 4.2 form an RHCP signal with amplitude A_L in the free space. The newly generated signals can be rewritten mathematically as:

$$LHCP : \widehat{a_H} \cdot A_L e^{-j90^\circ} + \widehat{a_V} \cdot A_L e^{-j0^\circ} \tag{4.3}$$

$$RHCP : \widehat{a_H} \cdot A_R e^{-j0^\circ} + \widehat{a_V} \cdot A_R e^{-j90^\circ} \tag{4.4}$$

where the $\widehat{a_H}$ and $\widehat{a_V}$ denote unit vectors in a horizontal and vertical direction, respectively, in a cartesian coordinate system.

This methodology of the generation of the dual circular polarization requires signal processing such as quadrature generation and quadrature mixing in the digital baseband (DBB). Normally those functions demand huge design burdens, e.g. area, and time. Even though generating circular polarization in DBB requires design burdens, digital signal processing can benefit their flexible calibration ability against any type of signal impairments.

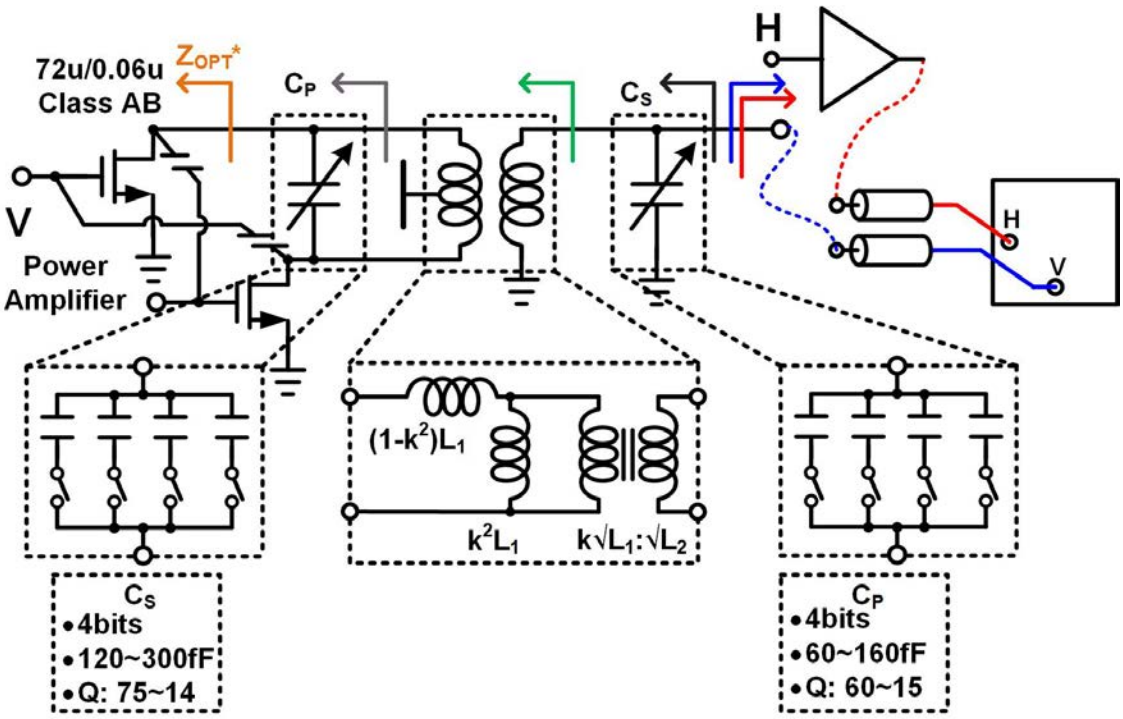

Figure 4.6: Circuit diagram of the designed PA and load tuner.

4.3 Load Tuner for Dual Circularly Polarized Phased Array

Figure. 4.6 illustrates the designed power amplifier (PA) and load tuner. The PA incorporates cross-coupled capacitors (CCC) to counteract the parasitic capacitor, C_{ds}, between the gate and drain terminals. The CCC effectively suppresses the reverse gain, thereby increasing the available power gain at the millimeter-wave frequency band. To achieve a low-loss design, the load tuner is integrated with the output matching network. This enables 2-dimensional load variation by controlling the two variable capacitors, allowing for complex load control on the Smith chart. The switches are implemented using 4-bit control for each. The C_S capacitor, located at the PA drain side, has a capacitance variation range of 120 fF to 300 fF and a Q value range of 75 to 15. The C_P capacitor, located at the load side, has a variable capacitance range of 60 fF to 160 fF and a Q value range of 60 to 15.

The detailed design method, regarding how to decide the capacitance values, is described in Figure. 4.7(a). The trajectories of the impedances seen at nodes highlighted as colored arrows are drawn in Figure. 4.7(a). The red and blue arrow denotes the H- and V-port impedances of the dual linearly polarized antenna or required impedance variation

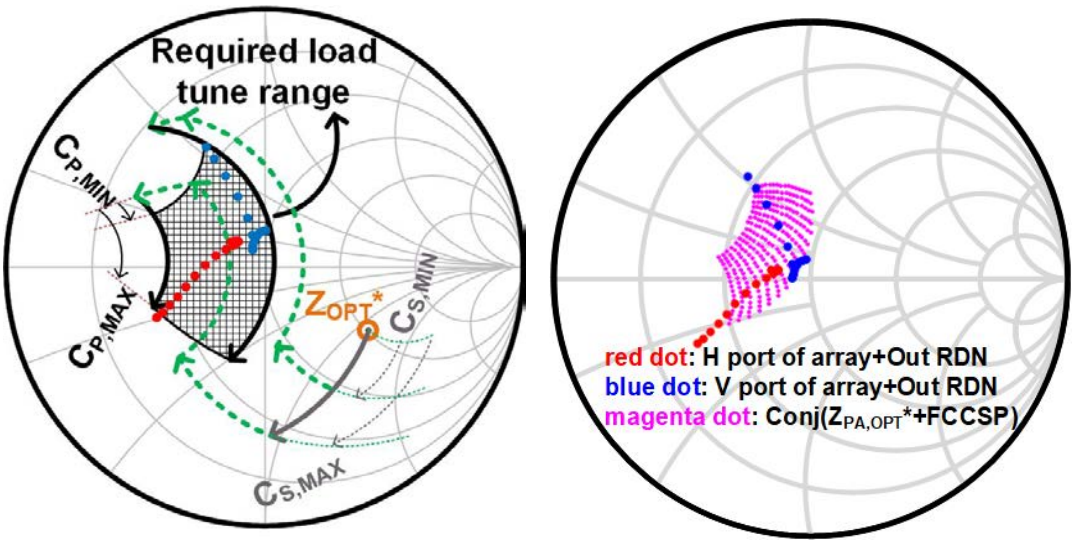

(a) (b)

Figure 4.7: Load tuner design: (a) conceptual design of PA and load tuner, and (b) simulated load variation of the array antenna and simulated load tuning coverage of the designed PA and load tuner.

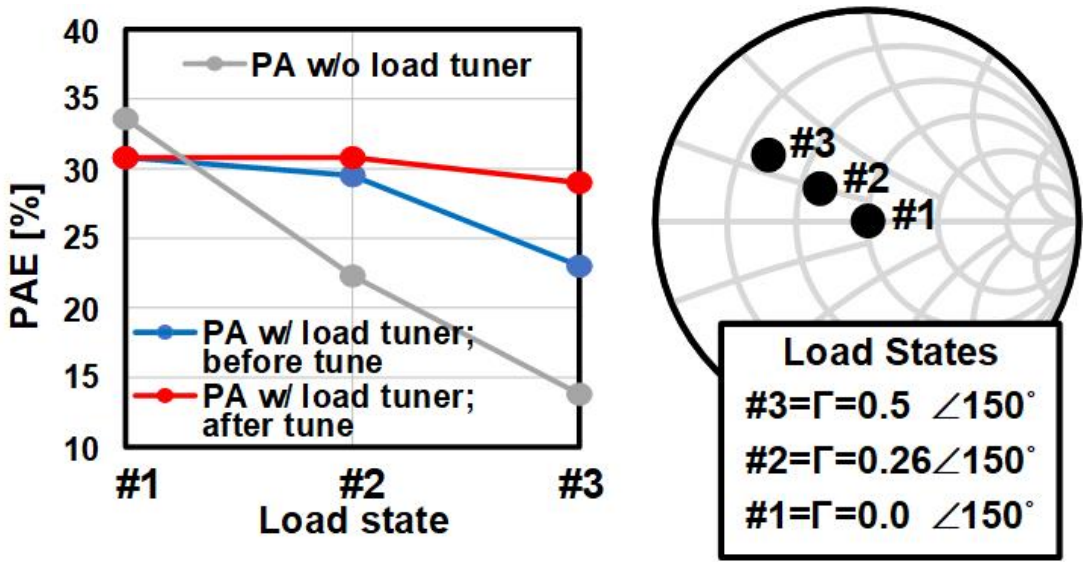

(a) (b)

Figure 4.8: Comparison of the PAs with and without load tuner: (a) Simulated PAE, and (b) load variation conditions used in PAE simulation.

range. This impedance range is the target impedance to be transformed from the optimum impedance of the PA. The first starting point is the brown-colored impedance, a conjugate of Z_{OPT}. Then draw the impedance trajectory of the C_S as being grey-colored. Here, the first-dimensional impedance variation range is decided. By modeling the transformer to

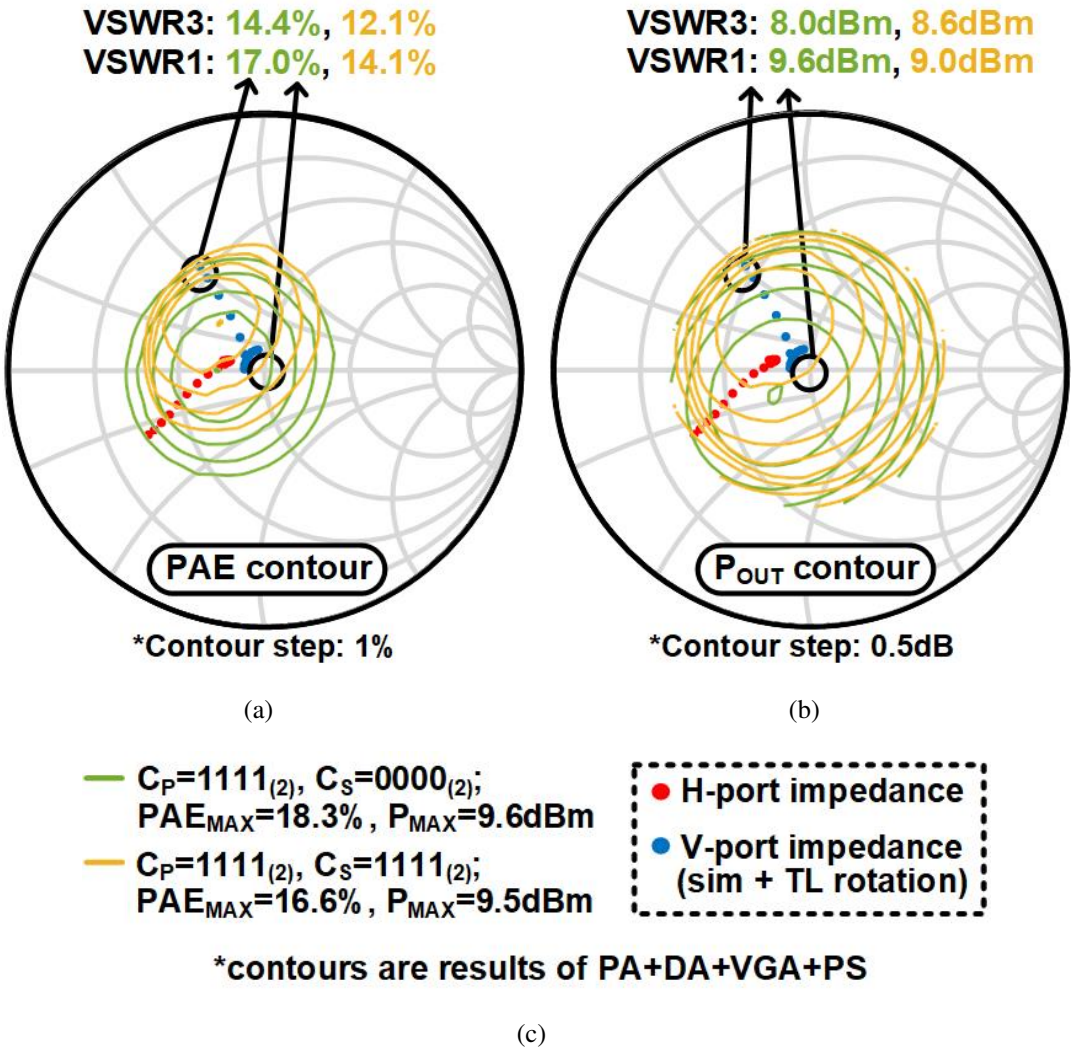

Figure 4.9: Measured PA and load tuner performances: (a) PAE with various load values, (b) output power of the PA with various load values, and (c) legend.

an equivalent circuit as shown in Figure. 4.6, draw the impedance change trajectories from the $C_{S,MAX}$, $C_{S,MIN}$. Then the black arrow, which denotes the impedance trajectory by the shunt variable capacitor, C_P, draws the second-dimensional impedance tuning range. From the above trajectories, the required variable capacitors and transformer values are decided. The Figure. 4.7(b) shows the simulated tuned impedance points seen at the output of the output matching network.

Figure. 4.6 depicts the designed power amplifier (PA) and load tuner, where the CCC technique is employed to neutralize the parasitic capacitor, C_{ds}, and thereby suppress the reverse gain, leading to an increased power gain at the mm-wave band. For low-loss design, the load tuner is integrated with the output matching network, and the two variable

capacitors allow for two-dimensional load variation, which enables complex load control on the Smith chart. The switches are designed with 4 bits each, and C_S, located at the PA drain side, has a capacitance variation range of 120 fF to 300 fF and Q values from 75 to 15. Similarly, C_P, located at the load side, has a variable capacitance range of 60 fF to 160 fF with a Q value of 60 to 15.

The detailed design methodology for determining capacitance values is illustrated in Figure. 4.7(a). Impedance trajectories for nodes indicated by colored arrows are depicted, where the red and blue arrows represent the H- and V-port impedances of the dual-linearly polarized antenna or the required impedance variation range. This impedance range is the target impedance that needs to be transformed from the optimal impedance of the PA. Starting from the optimal impedance, Z_{OPT}, the impedance trajectory of C_S is drawn in gray to determine the first-dimensional impedance variation range. By modeling the transformer as an equivalent circuit, as shown in Figure. 4.6, impedance change trajectories are drawn from $C_{S,MAX}$ to $C_{S,MIN}$. The black arrow indicates the impedance trajectory by the shunt variable capacitor, C_P, and determines the second-dimensional impedance tuning range. Using these trajectories, the required variable capacitors and transformer values are determined. The simulated tuned impedance points at the output of the output matching network are shown in Figure. 4.7(b).

4.4 Circular Polarization Calibration

Circular polarization calibration is a critical issue in dual circularly polarized transmitters. High signal cross-polarization discrimination (XPD) can be achieved by controlling the amplitude and phase of the signals at the digital baseband (DBB). However, the circular polarization calibration becomes impossible if the amplitude and phase errors are unknown. To address this problem, a novel detector for polarization detection is proposed.

As shown in Figure. 4.10, the designed polarization calibration system consists of couplers at H- and V-paths, which mix the signals at the center of the line, and a single power detector that measures the mixed signal power at the output of the load tuner. The amplitude and phase differences between the H- and V-paths are measured sequentially. In the amplitude measurement mode, only one path is driven, and the power detector measures the signal power to determine the amplitude of each signal path and the amplitude offset between the two paths. In the phase detection mode, both paths are driven with the same amplitude, which is calibrated in the amplitude measurement step. The mixed signal at the output of the couplers is measured by the power detector, while the phase difference between the two input signals is swept. The amplitude of the summed signals changes by the vector sum relationship, with the amplitude becoming maximum when the

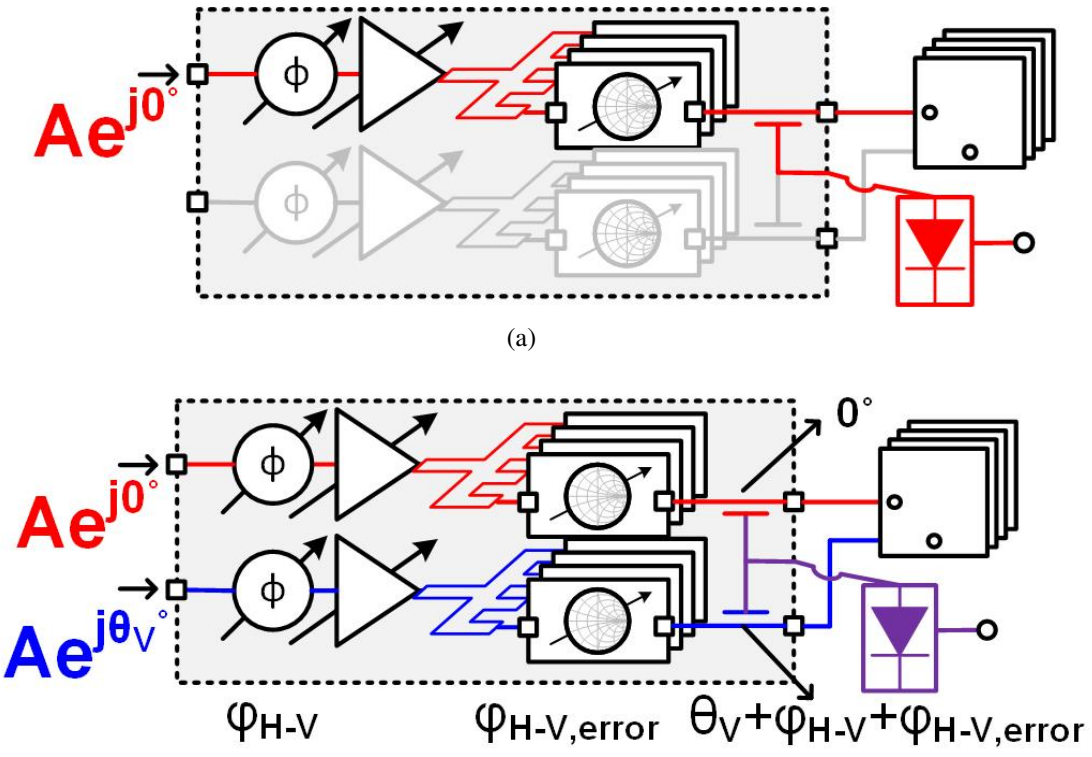

(a)

(b)

Figure 4.10: Description of (a) amplitude detection in H- and V-paths, and (b) phase detection in H- and V-paths.

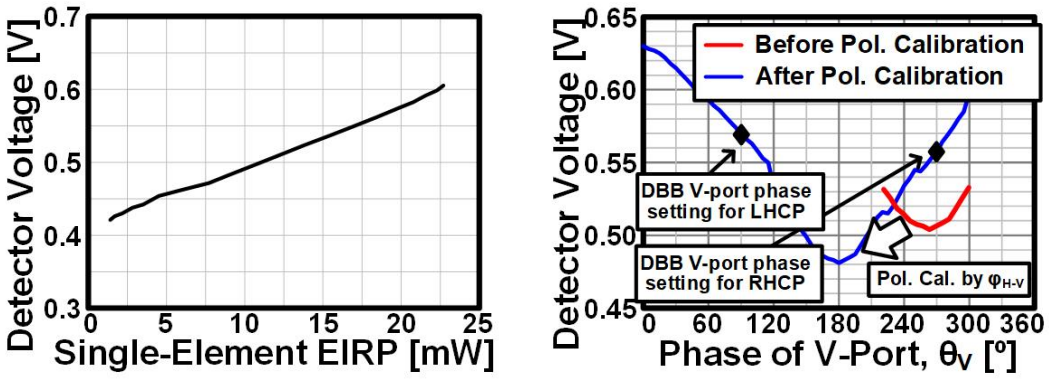

(a) (b)

Figure 4.11: Measured results of (a) amplitude with swept EIRP in amplitude detection mode, and (b) phases in phase detection mode.

phase difference is 0° and minimum when the phase difference is 180°. This step enables the phase offset between the two paths to be determined and rejected in the DBB control.

In order to validate this method, the amplitudes and phases were measured while

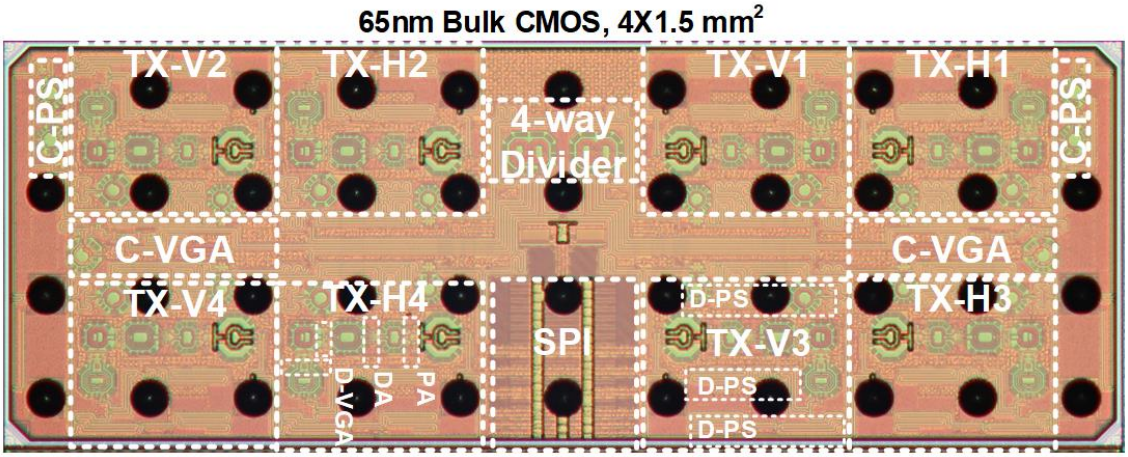

Figure 4.12: Die micrograph of the fabricated BFIC.

sweeping the input power and phase between the H- and V-paths, respectively. The measured results are presented in Figure. 4.11. Figure. 4.11(a) illustrates the detected single-path power with the swept power. Figure. 4.11(b) displays the measured phase with the swept input phase difference. The blue curve represents the on-wafer measurement result, which indicates no phase offset and displays a minimum measured amplitude at 180°. On the other hand, the red curve shows the measured detector outputs with an intentional phase offset using the phase shifter. This intentional phase offset implies that the phase error between the two paths must be calibrated in the DBB.

4.5 Measurement Results

A die micrograph of the BFIC fabricated with TSMC 65nm CMOS process is shown in Figure. 4.12, with a die size of 4×1.5 mm^2 integrating four dual paths on a single chip. The SPI is also integrated to control the amplifier's biases, while C-path RF blocks are also present on the die.

Figure. 4.13 depicts the manufactured 8×4-element phased array TX module, comprising eight BFICs to drive 32 dual linearly polarized patch antennas in the top layer view. The bottom view shows the implementation of an 8×4-element array with additional rows of dummy antennas to maintain a similar coupling between the edge and inner antennas.

The S-parameters of the fabricated BFIC with on-wafer measurement are shown in Figure. 4.14. Covering the full downlink band of the EESS, the single path of the TX achieves 24 dB gain.

The load tuner and circular polarization performance over the air were evaluated, and

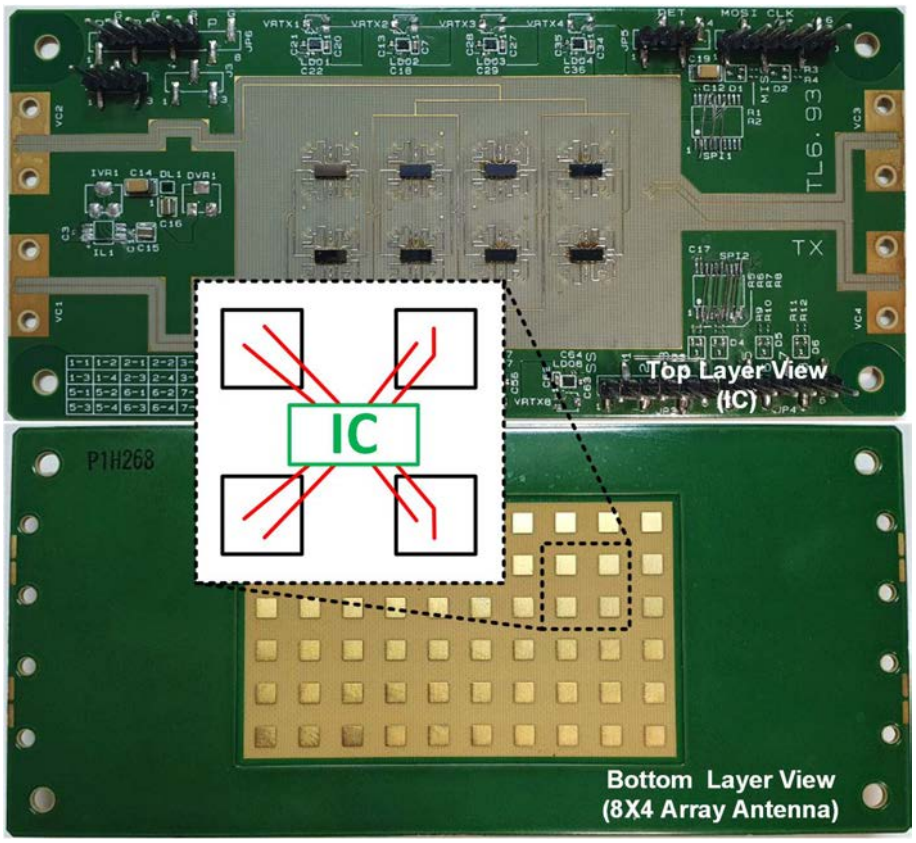

Figure 4.13: Photo of the fabricated phased array TX.

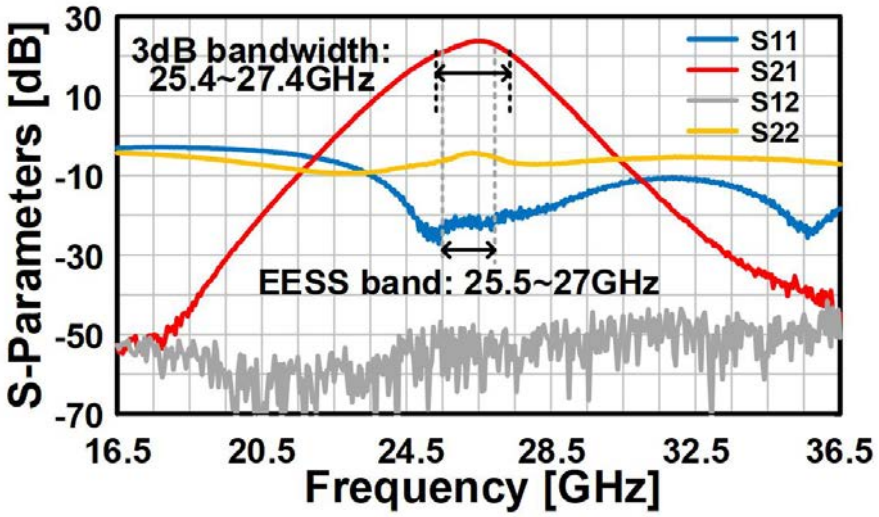

Figure 4.14: Measured S-parameters of the single path in the fabricated BFIC.

the drain efficiency and the XPD over the scan angle were measured, as shown in Figure. 4.15. The data were obtained at seven different scan angles, namely -50°, -40°, -20°,

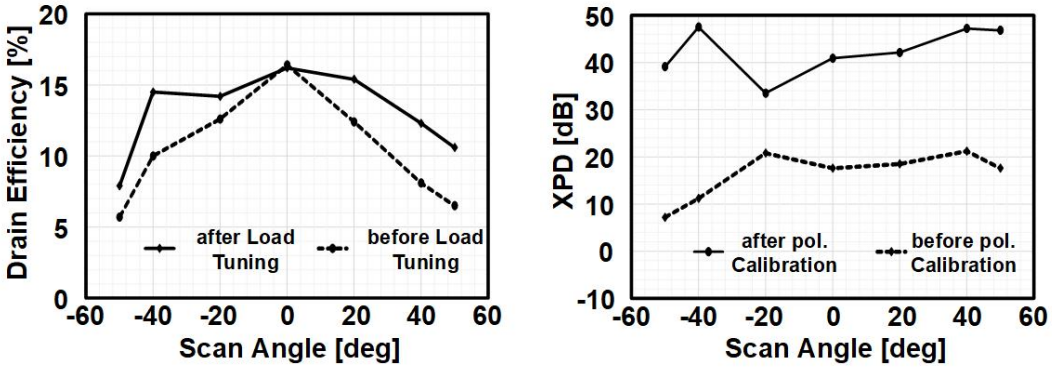

(a) (b)

Figure 4.15: Measured phased array TX performances over the beam steering angle with single tone signals: (a) TX efficiency, and (b) XPD.

0°, +20°, +40°, and +50°. The dashed line in Figure. 4.15(a) represents the measured drain efficiency of the TX before the beam steering. The optimum load tuning state was set for the highest drain efficiency, both before and after the load tuning, and the beam was then steered to retrieve the data. As shown in Figure. 4.15(a), the drain efficiency before the load tuning was very low, whereas the drain efficiency after the load adjustment significantly improved. At the -40° point, the drain efficiency was found to be 1.4 times higher than before.

It is worth noting that the load tuner must be differently controlled for the H- and V-path, as discussed in Figure. 4.4(b). As a result, the phase and amplitude by the load tuner setting also change. To compensate for these changes, circular polarization calibration was conducted after the load tuning. Figure. 4.15(b) presents the results before and after calibration. The dashed line represents the measured XPD before the calibration, which showed XPD values of less than 20 dB over the scan angles. However, after the calibration, the XPD was found to be at a very high level, with a maximum value of 47 dB at -40° beam angle and a minimum value of 33 dB at -20° beam angle. In terms of the increased step, the XPD was maximally recovered by 36.3 dB at -40° beam angle.

The discussion above describes the empirical verification of the fabricated phased array TX with a single tone. However, a more comprehensive evaluation is needed to fully assess the performance of the TX. Therefore, in addition to the single tone test, modulated signals are also used to evaluate the TX. The measurement setup for this test is depicted in Figure. 4.16, and the measurements are carried out over the air.

To generate the modulated signals, a Keysight M8195 arbitrary waveform generator (AWG) is used to generate dual circularly polarized signals. The upconverted signals are then fed into the fabricated phased-array TX. To control the biases and switches, a

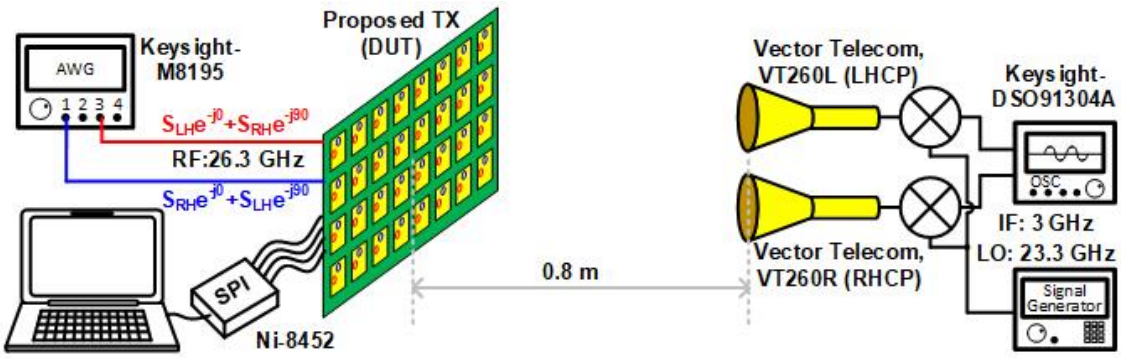

Figure 4.16: Measurement setup for over-the-air EVM measurement.

Modulation	16APSK	32APSK	64APSK
Constellation	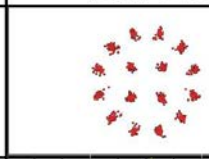	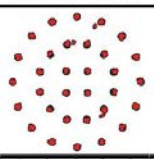	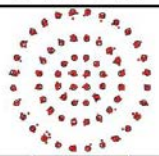
Spectrum	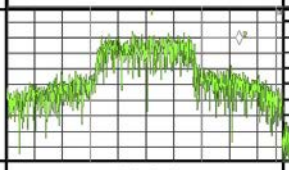	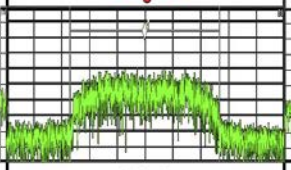	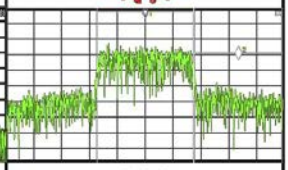
Bandwidth [MHz]	1000	100	200
EVM [dB]	-21.8	-30.2	-27.4

Figure 4.17: Measured EVM and constellations with various modulations.

python script and a Ni-8452 SPI module are employed. Two commercial-off-the-shelf circularly polarized antennas are located at a distance of 0.8 meters away from the TX. After down-converting the signal, a Keysight DSO91304A oscilloscope samples the signal at an intermediate frequency (IF) of 3 GHz. This setup enables a more comprehensive evaluation of the TX's performance using modulated signals.

In addition to the single-tone tests, the performance of the fabricated phased-array TX was also evaluated with modulated signals. The measurement setup for this test is illustrated in Figure. 4.16, and the measurements were performed OTA. The Keysight M8195 arbitrary waveform generator (AWG) generated dual circularly polarized signals, which were then upconverted and input into the phased-array TX. All the biases and switches were controlled using Python and the Ni-8452 SPI module. Two commercial-off-the-shelf circularly polarized antennas were located 0.8 meters away from the TX, and the downconverted signals were sampled by the Keysight DSO91304A oscilloscope at an intermediate frequency (IF) of 3 GHz.

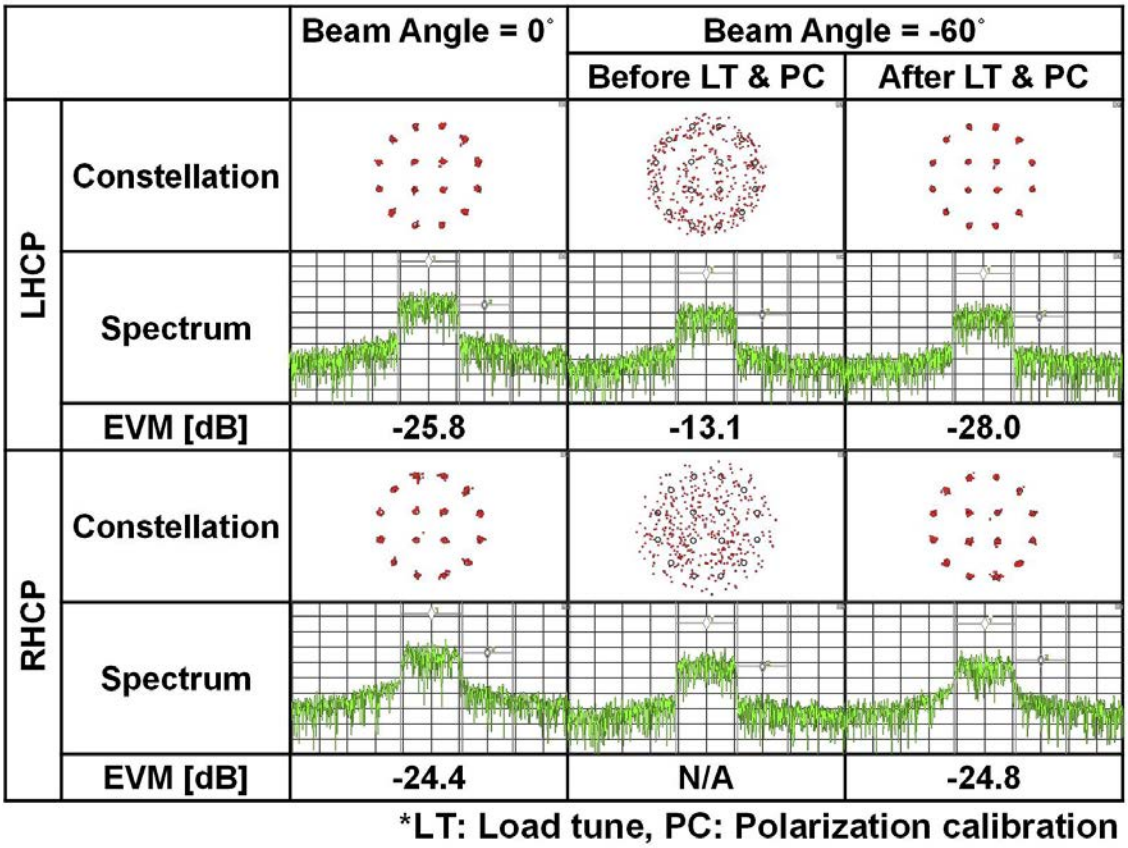

Figure 4.18: Measured EVM and constellations with dual circularly polarized signal under various beam angles.

The measured EVMs and constellations for different modulation schemes are shown in Figure. 4.17. With a 16-APSK signal and a symbol rate of 1 GBaud, an EVM of -21.8 dB was achieved, and a very clean constellation was observed. The TX was also tested with higher-order modulations. With a 32-APSK signal and a symbol rate of 100 MBaud, an EVM of -30.2 dB was achieved, and with a 64-APSK signal and a symbol rate of 200 MBaud, an EVM of -27.4 dB was achieved. All the measurements were performed at a 0° beam angle with single circularly polarized signals.

The EVMs with dual circularly polarized signals under various beam angles were also measured. The measured EVMs at different beam angles are shown in Figure. 4.18. For this measurement, both LHCP and RHCP signals were input simultaneously and measured at two RX points simultaneously. At the 0° beam angle, the LHCP and RHCP signals exhibited EVMs of -25.8 dB and -24.4 dB, respectively. However, at a -60° beam angle, critically contaminated constellations were observed, and the EVMs were -13.1 dB and -21.9 dB for LHCP and RHCP signals, respectively. To address this issue, load tuning and circular polarization calibration were conducted, and the EVMs were recovered to -28

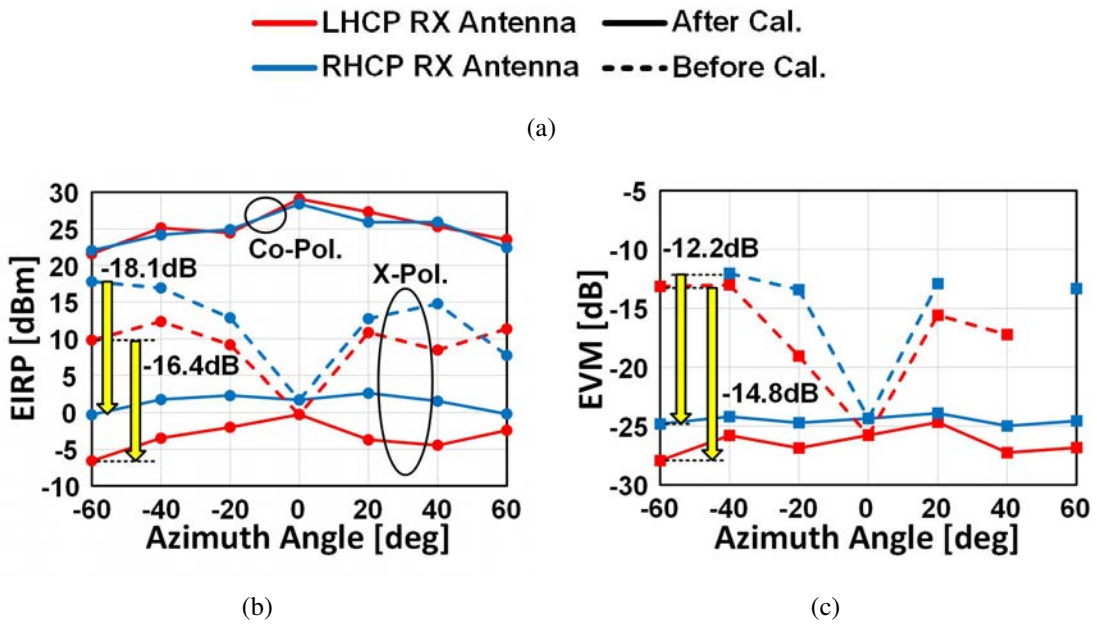

Figure 4.19: Measured phased array TX performances over the beam steering angle with modulated signals: (a) legend, (b) EIRP, and (c) EVM

dB and -24.8 dB for LHCP and RHCP signals, respectively, with clean constellations.

In addition, EVMs with dual circularly polarized signals were measured under various beam angle conditions, and the data are summarized in Figure. 4.19. The measured EIRP of the co-polarization and cross-polarization of the LHCP and RHCP signals is also presented in Figure. 4.19(b). Before the load tuning and calibration, the cross-polarization components for both LHCP and RHCP signals were very high. However, the proposed load tuner and polarization calibration technique successfully suppressed the cross-polarization components to a great extent. At the -60° beam angle, the cross-polarization EIRPs were suppressed by a maximum of -18.1 dB and -16.4 dB for RHCP and LHCP signals, respectively.

Similarly, the EVMs are presented in Figure. 4.19(c). As expected from Figure. 4.19(b), deadly bad EVMs were recorded over the beam steering before the load tuning and circular polarization calibration. However, after the load tuning and circular polarization calibration, the EVMs were reduced to below -24 dB. A maximum recovery of -12.2 dB and -14.8 dB of the EVM for the RHCP and LHCP signals were achieved, respectively.

4.6 Summary

The proposed Ka-band dual circularly polarized CMOS TX with load tuning and circular polarization calibration technique resulted in significant improvements in performance.

Specifically, the technique helped recover the TX efficiency by 40% from before calibration and improved the XPD by 36.3 dB. Additionally, the load tuner and circular polarization calibration circuit achieved -28 dB EVM with dual polarization, demonstrating the effectiveness of the proposed approach.

In this chapter, two key techniques were presented for the implementation of an LEO small satellite constellation. The first technique, the load tuner for the dual circularly polarized phased array TX, successfully increased the efficiency of the system at various scan angles. By achieving high efficiency, the need for redundant DC power to increase the output power was eliminated, resulting in a low power consumption design. The second technique, dual circular polarization calibration, allowed for the use of dual circular polarization to double the data rate. These two techniques are crucial for the successful implementation of an LEO small satellite constellation.

Chapter 5

Power-Efficient Circular Polarization Coupler

This chapter presents two power-saving techniques for addressing the challenges faced by small LEO satellites. The first technique involves a systematic array design for low-power consumption in the LEO satellite constellation. The second technique involves the use of a novel circular polarization coupler to save redundant DC power in a single circular polarization mode. In Section 5.1, the chapter discusses how DC power consumption can be saved with the proposed systematic design method, and reviews conventional circularly polarized phased arrays' circular polarization generation methodologies. Section 5.2 presents the implementation of the proposed active phased array and circular polarization coupler. Section 5.3 provides empirical results showing extremely saved DC power and excellent XPD with the circularly polarized signal by the proposed circular polarization coupler. Finally, Section 5.4 summarizes the chapter.

5.1 Introduction

5.1.1 Phased Array for Low Power Consumption

Power consumption has always been one critical key issue in satellite communication. Because the satellite solely relies on solar power as its energy source, which is not abundant in the space environment, the power consumption of each functional equipment must be carefully designed. This issue also applies to the phased array for LEO SATCOM too.

In the design of an active phased array, the number of elements, N, and the output power of a single element PA, P_{OUT}, are important design parameters. The number of elements, N, is related to the array gain, which determines the beam width or communi-

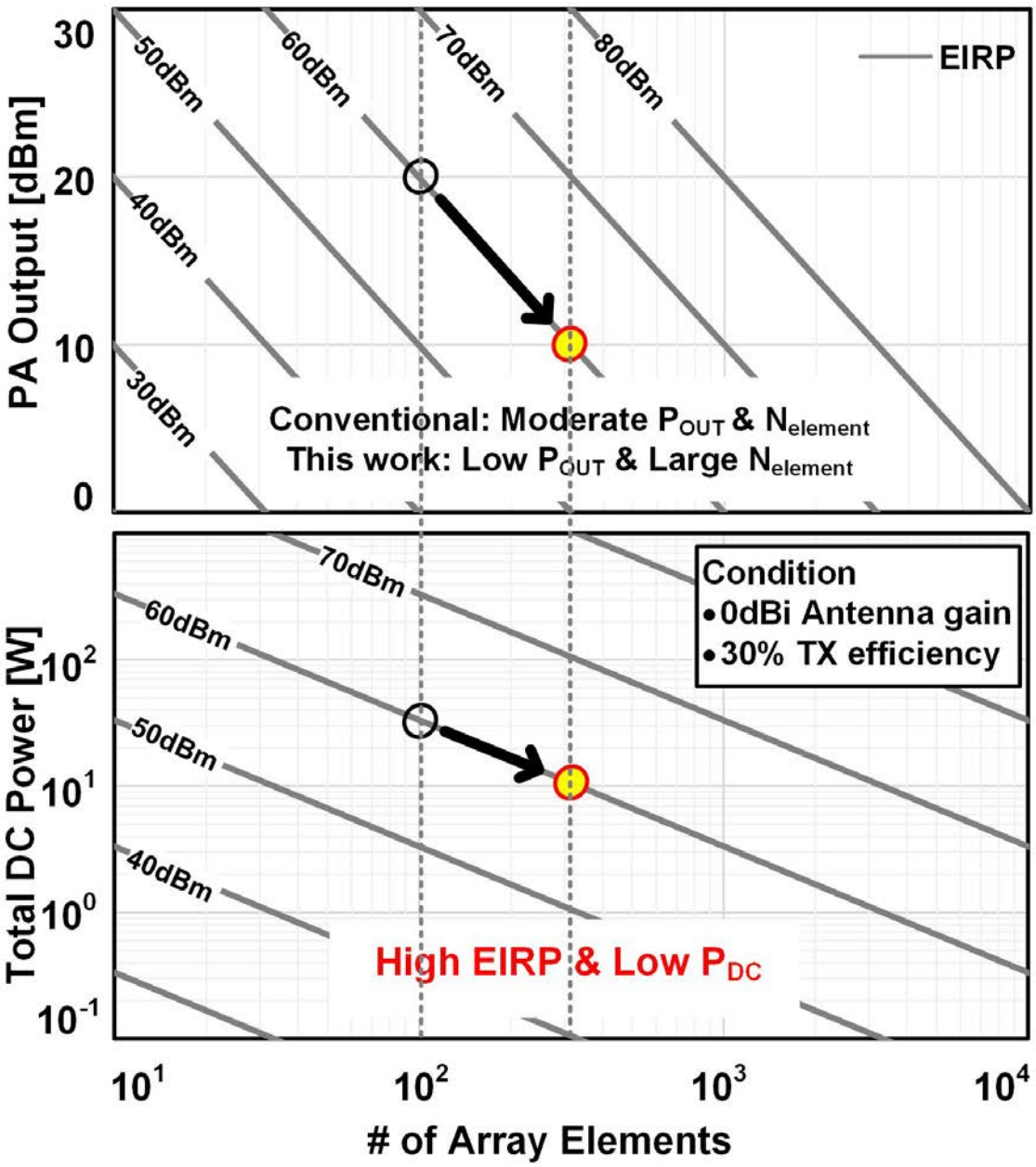

Figure 5.1: DC power consumption and EIRP of the phased array system over the number of elements.

cation coverage. The beam width is determined independently by the array shape and the number of elements. However, the important design parameters, such as EIRP and total DC power consumption, are determined by both the number of elements, N, and the output power of a single element PA, P_{OUT}. The relationship between these two parameters

and the EIRP can be represented by the equation:

$$EIRP\ [dBm] = P_{OUT}\ [dBm] + 20 \times \log_{10} N\ [dB]. \tag{5.1}$$

The EIRP must be determined by the communication link requirements, such as the required SNR and link distance. Thus, in the decision-making process for the number of elements, N, and the output power of a single element PA, P_{OUT}, the EIRP should be a fixed value. This fixed EIRP parameter is also helpful for the decision of the number of elements, N, and the output power of a single element PA, P_{OUT}, because according to Equation 5.1, only one parameter, the number of elements, N, needs to be considered in the further phased array design.

In Figure. 5.1, the relationship between the single element PA output power, P_{OUT}, and total DC power consumption is shown as a function of the number of elements, N. The illustration assumes a 0 dBi single element antenna gain and 30% TX efficiency for simplicity. A significant observation from the figure is that as the number of elements increases by a factor of 10, the single element PA output power, P_{OUT} decreases by -20 dB, while the total DC power consumption decreases by a factor of 10. This indicates that a low-power PA design with a larger array size can achieve lower DC power consumption. In other words, increasing the antenna gain can lead to a reduction in both the output power of the PA and DC power consumption. This observation is consistent with Equation 5.1.

If the antenna gain is excessively high, the beam width becomes narrower, which reduces the communication coverage area. However, this narrow coverage area is not a significant issue in either of the following two cases:

- The system should cover the entire globe.
- The system should communicate with only a single or a few ground stations.

In the first case, since the system already consists of satellite constellations, a narrow beamwidth is not a critical issue. Instead, narrower beams can increase the data rate by utilizing space-division multiplexing. In the second case, because the active phased array can quickly sweep the beam direction, the beam can be sustained for a long time over an orbit cycle.

5.1.2 Circular Polarization Generation and State-of-the-Arts

While Chapter 4 demonstrates the importance of circular polarization with high XPD in terms of signal coupling, this subsection highlights the significance of high XPD circular

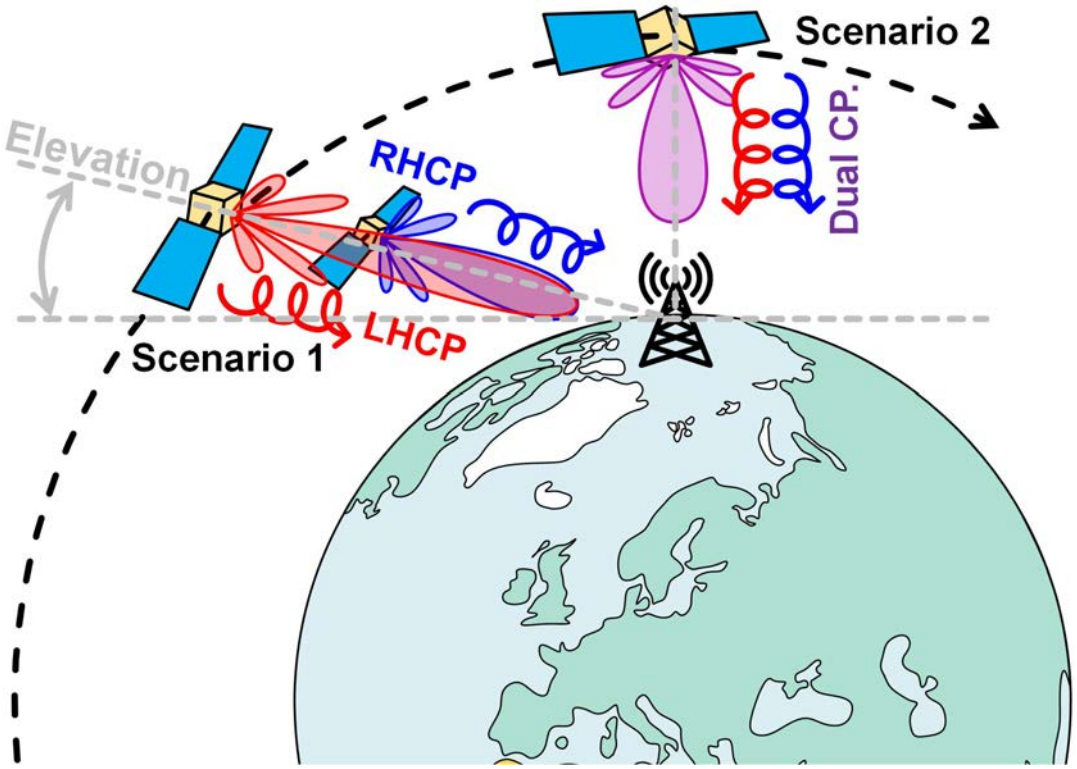

Figure 5.2: Two circular polarization scenarios in LEO SATCOM with different elevation angles.

polarization from a different perspective and provides a comparison of various circular polarization methodologies in the literature.

As discussed in Section 5.1.1, satellite-to-ground links can be categorized into two types: a satellite to multiple ground stations, and a satellite to a single ground station. In the case of multiple ground stations, the link distance between the satellite and each ground station does not vary much as several satellites are covering the globe at the same time. However, in the case of a single ground station, the link distance between the satellite and the ground station varies significantly, as shown in Figure. 5.2.

This thesis focuses on the satellite-to-a-single-ground-station case, which can be further divided into two categories:

- Scenario 1: Low elevation and long link distance.
- Scenario 2: High elevation and short link distance.

Scenario 1 refers to situations where the satellite is flying at a low elevation angle, resulting in a maximum link distance. At 10° elevation angle and 585 km orbit altitude, the distance in Scenario 1 is approximately 1900 km, which is more than three times the

minimum link distance of 585 km. This distance difference results in a more than 10 dB loss difference in free space loss, as shown in Equation 2.35. In Scenario 1, to improve the survivability against higher free space loss, the satellite can switch its transmitting mode to a single polarization mode. This is because dual circularly polarized signals may suffer from signal degradation due to not only low XPD but also low received signal level.

On the other hand, in Scenario 2, the satellite is flying at a high elevation angle of 90°, resulting in a shorter link distance. In this scenario, the satellite can switch its transmitting mode to dual circular polarization mode for greater data throughput. As the link distance in Scenario 2 is much shorter than that in Scenario 1, and the received power at the ground station is larger, degraded XPD due to dual circular polarization is more durable.

The importance of high XPD circular polarization is evident in both scenarios, but it is particularly crucial for scenario 2 where dual circular polarization is expected to be utilized. In this case, the XPD of the circular polarization plays a critical role in achieving high data throughput. On the other hand, scenario 1 operates with a single circular polarization, but the XPD is still relevant because other satellite systems may use opposite polarization types in the same frequency band, necessitating a high XPD for polarization division multiplexing. Thus, it can be concluded that achieving a high XPD for circular polarization is a key factor for the successful implementation of SATCOM using satellite constellations in both scenarios.

Numerous designs for SATCOM phased arrays have been proposed in literature [6, 8, 74–83]. While these designs employ various methods to generate circular polarization, they can be broadly classified into three categories: using circularly polarized antennas, reusing the phase shifters (PSs) and variable gain amplifiers (VGAs) in the beamformer, and mixing circular polarization signals in the digital baseband (DBB). These methodologies are well summarized in Figure. 5.3.

The first method employs circularly polarized antennas, which is the simplest way to generate circularly polarized signals. Dual circular polarization can be supported by driving the left-hand circular polarized (LHCP) and right-hand circular polarized (RHCP) feeding ports of the antennas. Moreover, by turning off the unused single circular polarization path, either LHCP or RHCP, significant power can be saved. However, this method has a critical disadvantage: the cross-polarization discrimination (XPD) is inherently low due to the large process variations in the printed circuit board (PCB). Calibration for the low XPD is not possible, which is a significant drawback for generating high XPD circularly polarized signals.

The second methodology involves reusing the PSs and VGAs in the beamformer with dual linearly polarized antennas. By feeding the same signal into the horizontal (H) and vertical (V) paths and adjusting the phase and amplitude in the beamformer, quadrature

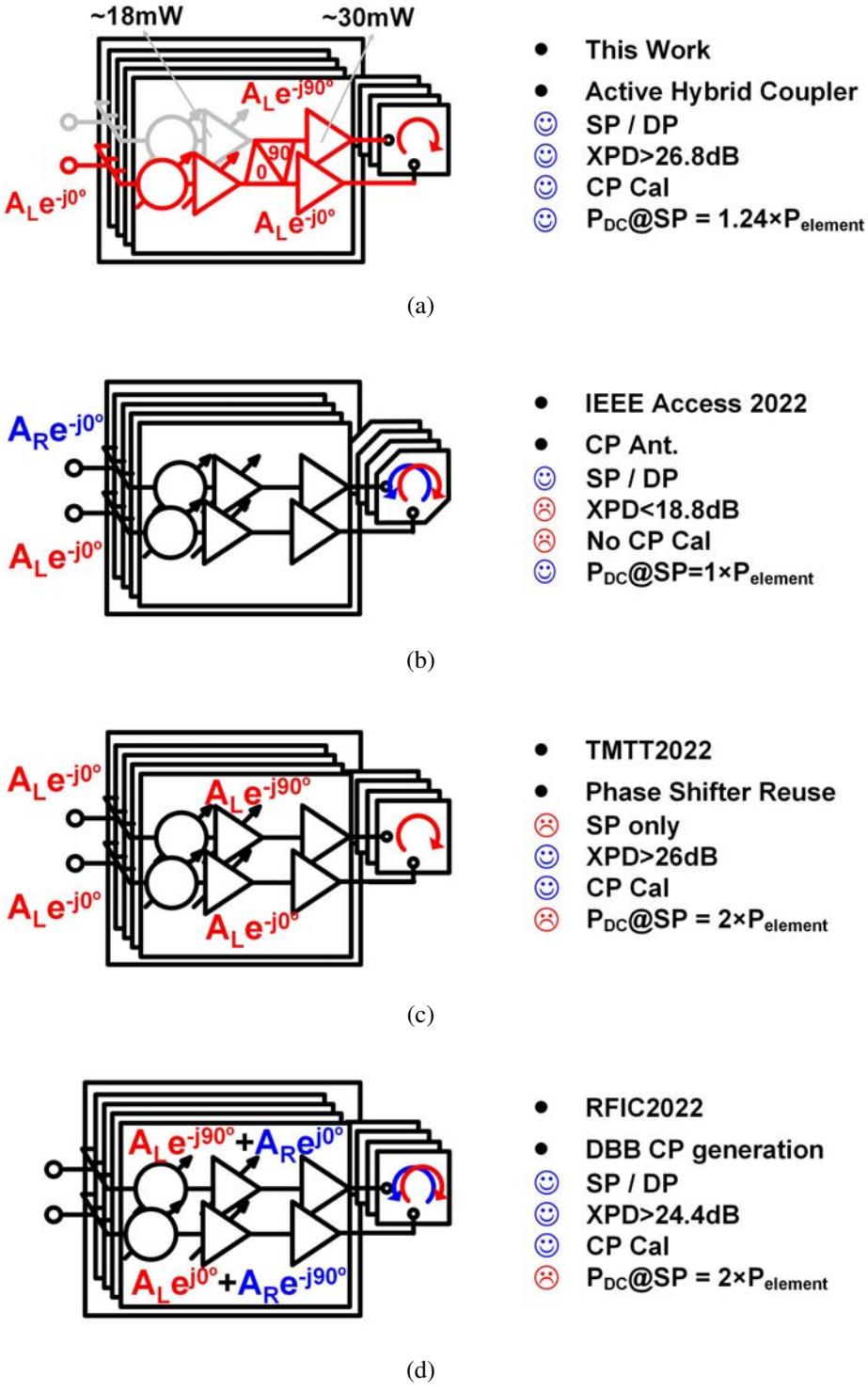

Figure 5.3: Block diagrams and their advantages and disadvantages: (a) proposed architecture [5], (b) circularly polarized antenna [6], (c) phase shifter reuse [7], and (d) DBB generation [8].

signals in the H- and V-polarizations can be generated, resulting in a circularly polarized signal. Since this method inherently has PSs and VGAs, the deteriorated XPD can be calibrated to achieve a high XPD. However, this method also has critical disadvantages. Dual circular polarization cannot be generated since two different signals are fed into the H and V paths, and their phase must be shifted in opposite directions, i.e., one in plus quadrature and the other in minus quadrature. Additionally, power consumption is twice that of the circular polarization generation using circularly polarized antennas.

The third methodology generates dual circularly polarized signals in the DBB. Unlike the method that reuses the beamformer, this approach can shift the phase of the two different signals in opposite directions, enabling dual circular polarization. Furthermore, with the flexible waveform generation feature of the DBB, calibration of the deteriorated XPD is possible, leading to very high XPD. However, this method also suffers from doubled power consumption in a single circular polarization mode.

In this thesis, a new method of circular polarization is proposed. By generating a quadrature signal using a proposed active quadrature coupler immediately preceding the power amplifier (PA), significant advantages can be gained. First, by turning off all preceding stages before the PAs, power consumption in single circular polarization mode can be greatly reduced, e.g., 76% of the DC power is reduced in Figure. 5.3(a). Second, combined with the DBB circular polarization method, dual circular polarization is also possible. Finally, with the circular polarization calibration feature in the active quadrature coupler, the deteriorated XPD can be calibrated even if there is a drop in the XPD, offering superior performance.

5.2 Circuit Implementation

5.2.1 Proposed Dual CP Phased Array TX

Figure. 5.4 depicts the architecture of the designed Ka-band dual circularly polarized active phased-array transmitter. The transmitter consists of 256-element antennas integrated into a TX, which is driven by 64 BFICs. Each BFIC integrates eight channels of the TX, with two individual channels comprising a dual-polarized channel, resulting in four dual-polarized channels in an IC. In each dual-polarized channel, there are two PAs, one active quadrature coupler, a D-VGA, and a D-PS for the H- and V-path RF blocks. Each H- and V-path is independently driven by 4-way lumped-element Wilkinson power dividers further driven by the C-VGA and CPS. The H-path inputs of the IC are all driven from a single H-path input and 64-way power divider, as are the V-path inputs. The proposed BFIC includes a low dropout regulator (LDO) for each dual-polarized channel, bandgap

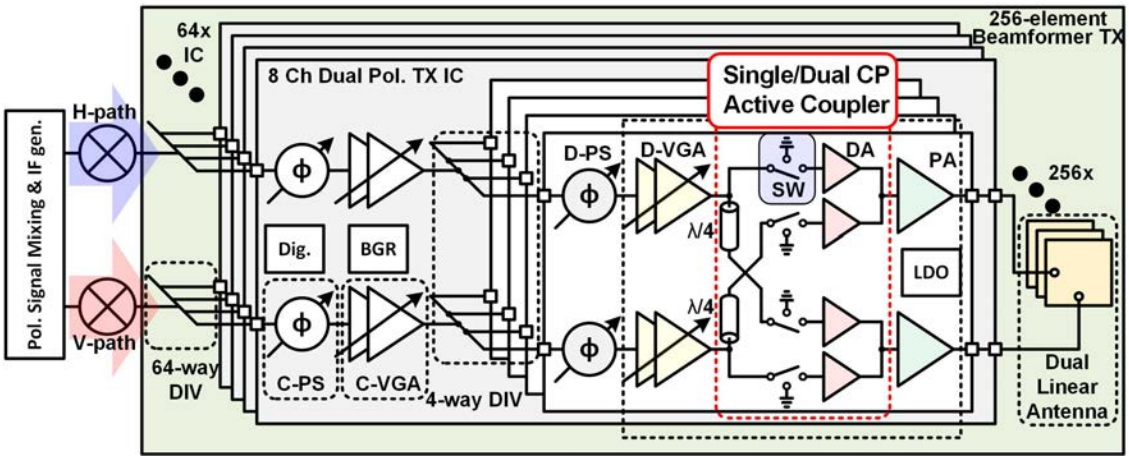

Figure 5.4: Block diagram of the proposed Ka-band dual circularly polarized active phased array TX.

references, and digital controls for bias control.

5.2.2 Circular Polarization Coupler

One of the key components in the proposed BFIC is the active quadrature coupler for circular polarization generation. A simplified block diagram of the proposed active quadrature coupler is shown in Figure. 5.5, along with conventional hybrid couplers for comparison of hybrid coupler performance. Conventional hybrid couplers, which come in distributed and lumped-element types, provide 90° true phase shift necessary for polarization generation. However, they lack calibration features, making them susceptible to process variation. Additionally, the conventional quadrature hybrid coupler requires four quarter-wavelength transmission lines, which are bulky. Even the lumped-element hybrid couplers, which use transformers, are large and difficult to integrate into a crowded RF system layout.

In contrast, the proposed active quadrature coupler generates a 90° phase shift using a pair of quarter-wavelength transmission lines, with amplitude and phase calibration achieved by deploying DAs at the end of the lines. The coupler area is primarily determined by the quarter-wavelength lines, allowing for flexible layouts that can be fit to adjacent sensitive RF blocks. Despite its many advantages, the active quadrature coupler has one disadvantage: it provides not 90° phase shift, but rather 90° time delay. As a result, the phase may differ from the 90° phase at the upper and lower limits of the signal frequency band. To evaluate the amount of phase difference from a frequency offset under

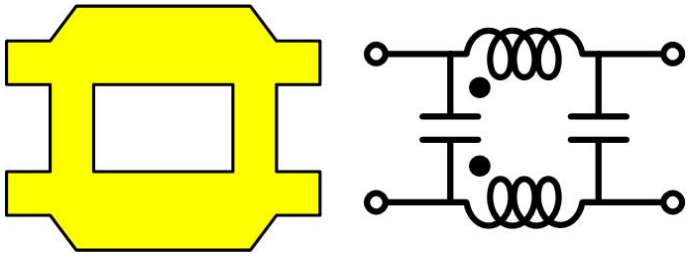

(a)

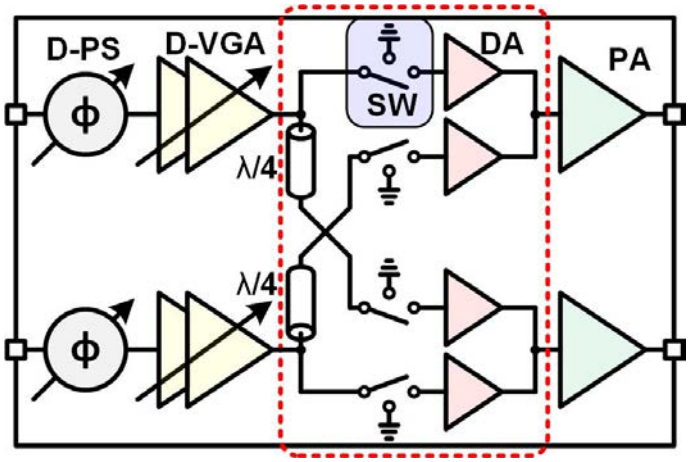

(b)

Figure 5.5: Two different types of the hybrid coupler: (a) conventional distributed and lumped-element hybrid coupler, and (b) proposed active quadrature coupler.

a fixed time delay condition, the following expressions are used:

$$\phi_C = -\frac{t_C}{\omega_C} \tag{5.2}$$

$$\Delta\phi = \phi_C \times \left(1 + \frac{\Delta\omega}{\omega_C}\right), \tag{5.3}$$

where ϕ_C is the phase delay at the center frequency, t_C is the time delay, ω_C is the center frequency, $\Delta\omega$ is the frequency offset from the center frequency, and $\Delta\phi$ is the phase shift at a frequency offset under time delay t_C. For example, in the EESS downlink band case, $\Delta\omega$=+0.75 GHz at the upper limit frequency from a center frequency of ω_C=26.25 GHz. With ϕ_C=-90°, $\Delta\phi$=-90-2.5° at the upper limit frequency. Similarly, the phase offset at the lower limit frequency, $\Delta\omega$=-0.75 GHz, is $\Delta\phi$=-90+2.5°. This ±2.5° phase offset is negligible in terms of cross-polarization discrimination (XPD) as shown in Figure. 4.3. Without the gain error, the ±2.5° phase offset provides more than 32 dB XPD. Thus the only disadvantage of the proposed active quadrature coupler is not the disadvantage anymore. The pros and cons are summarized in Table. 5.1.

Table 5.1: Comparison of various circular polarization generation methodologies.

	Conventional hybrid couplers	Proposed active hybrid coupler
Advantages	90° true phase shift	$\lambda/4$ lines: 90° shift, $\lambda/4$-shunt stub (∞-Z) gain & phase calibration (DAs) Compact and flexible layout
Disadvantages	No calibration feature Huge and fixed layout	90° time delay

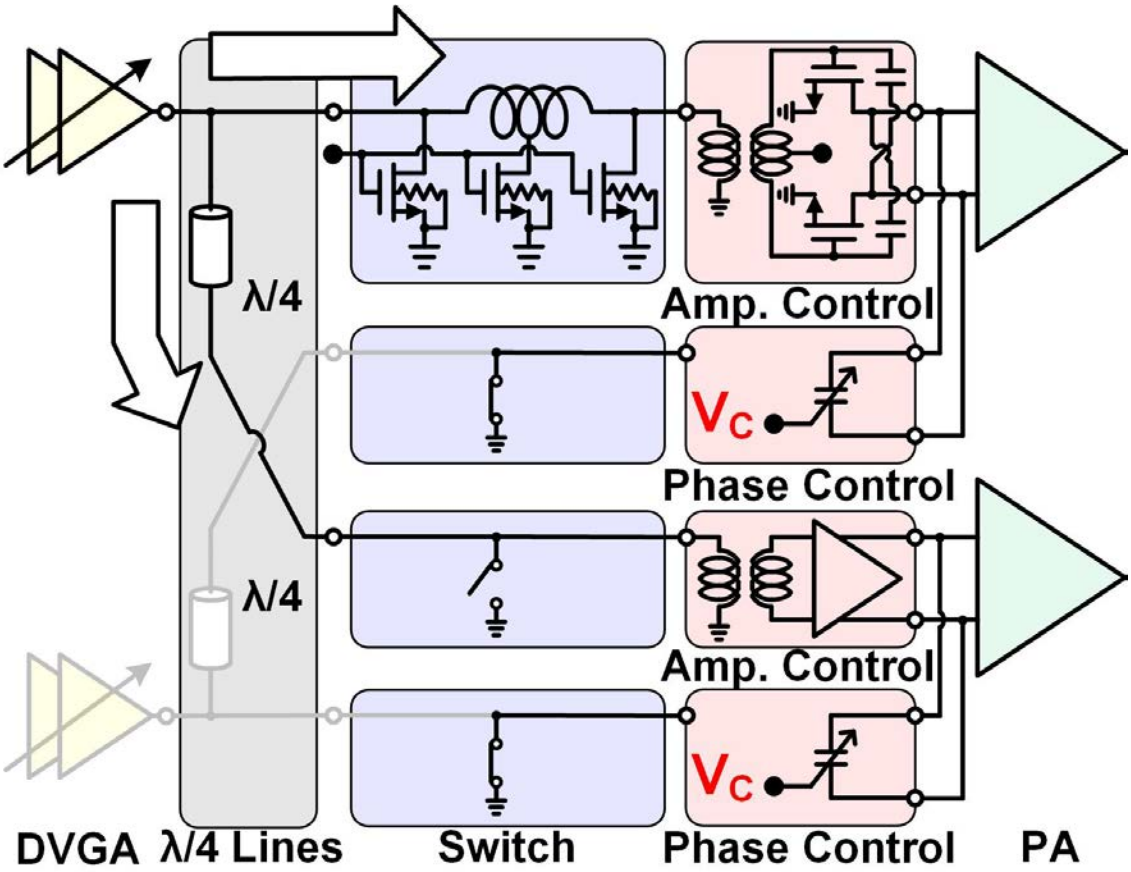

Figure 5.6: Block diagram of the proposed active quadrature coupler.

Figure. 5.6 illustrates in detail how the proposed active quadrature coupler works for a single circular polarization mode. To save DC power consumption, the lower D-VGA and all the preceding stages of the lower D-VGA are turned off. After the signal passes through the upper D-VGA, it is split into two paths. One path is directly connected to an RF shunt switch, while the other path goes through the quarter-wavelength line before

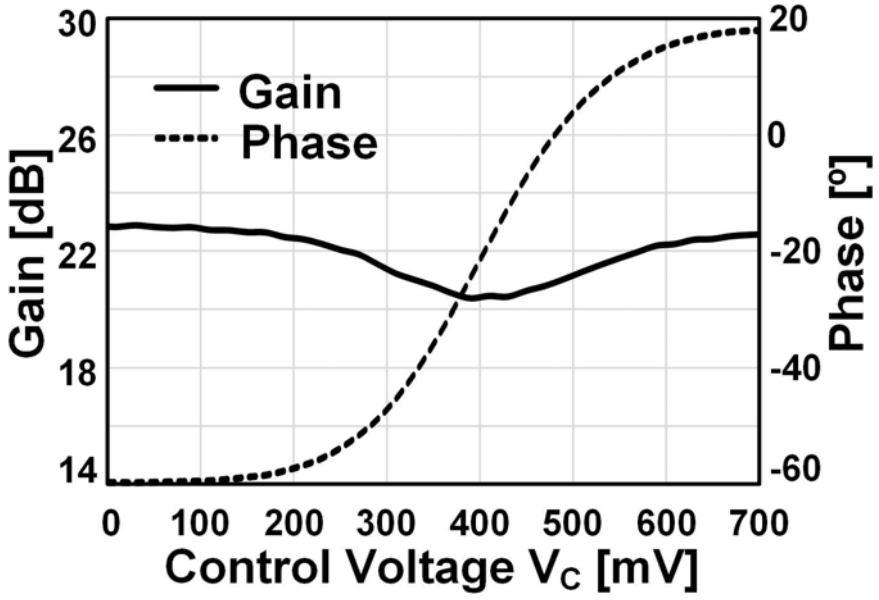

Figure 5.7: Measured amplitude and phase of the proposed active quadrature coupler.

being connected to an RF shunt switch. This quarter-wavelength difference generates the required 90° phase shift. The RF switches then pass the signals to the next stage, while the RF switches connected to the lower D-VGA are shunted. The signals then pass through DAs, which act as VGA to compensate for the gain difference in the H- and V-ports of the antenna. The DA consists of a common source differential amplifier with gate-drain capacitance neutralization capacitors. The DAs that are connected to the lower D-VGA without signals act as PSs for phase compensation for the H- and V-ports of the antenna. The proposed active quadrature coupler provides reduced power consumption and a circular polarization calibration feature.

The amplitude and phase measurements of the uppermost path in Figure. 5.6 are presented in Figure. 5.7. By adjusting the bias of the DA, the DA in the signal path behaves like a VGA, and the DA in the non-signal path behaves like a phase shifter. In Figure. 5.7, the phase control bias of the upper path is varied. While the gain only changes by 3 dB, the phase shifts by 80°.

To further investigate the gain and phase errors between the two signal paths in Figure. 5.6, the lower D-VGA and all the paths connected to it are turned off. The measured gain and phase errors as a function of frequency are shown in Figure. 5.8(a). As indicated by the dashed lines, the two error curves are far from the zero offset lines for both gain and phase. However, after calibration (indicated by the solid lines), the two error curves are almost parallel to the zero offset lines for gain and phase. Furthermore, the gain and phase measurements can be presented as XPD plots, as shown in Figure. 5.8(b). Before

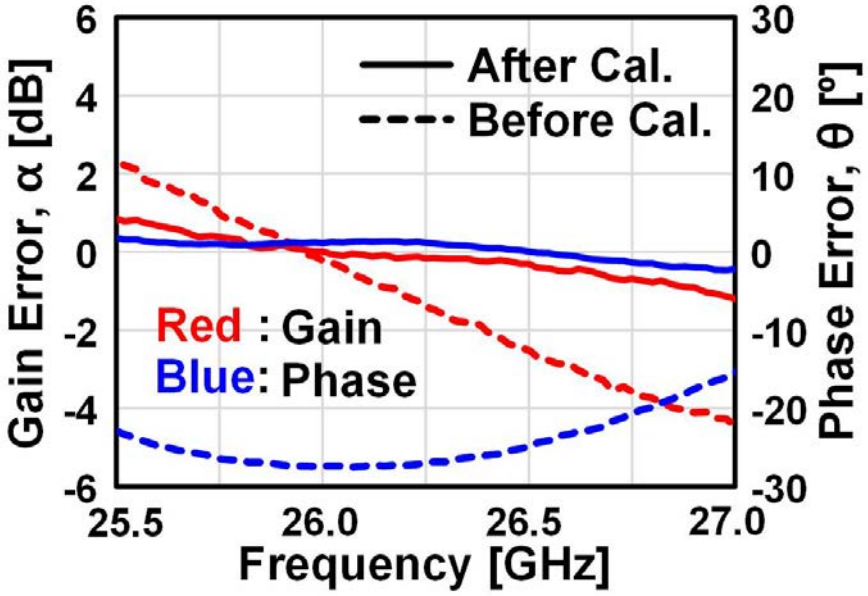

(a)

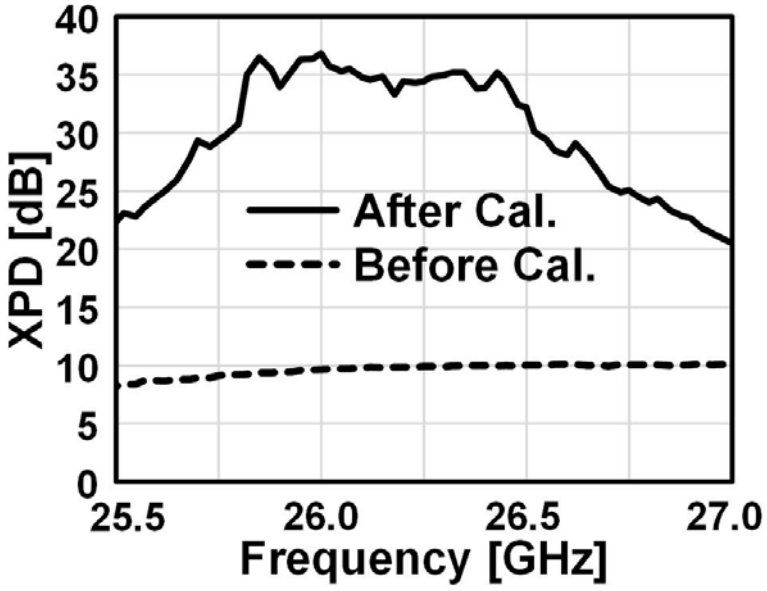

(b)

Figure 5.8: Measured results of the proposed active quadrature coupler: (a) gain error and phase error, and (b) XPD before and after calibration.

calibration, the XPD is below 10 dB, but after calibration, more than 20 dB of XPD is achieved. The maximum XPD improvement achieved is 27.2 dB at 25.8 GHz.

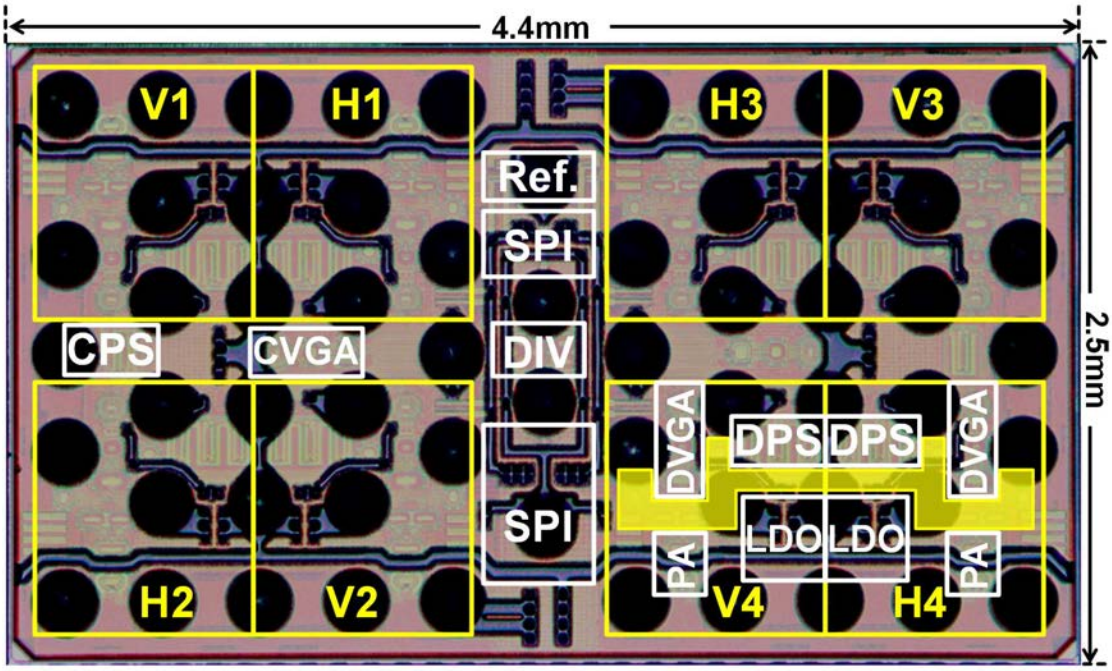

Figure 5.9: Micrograph of the proposed Ka-band dual circularly polarized active phased array TX RFIC.

5.3 Measurement Results

Figure. 5.9 depicts a micrograph of the fabricated BFIC. The IC is manufactured using TSMC CMOS 65nm process, and its size is 4.4 mm × 2.5 mm. The IC integrates four dual-polarized channels, SPI for biases and digital control, LDOs for each channel, and bandgap references.

In channels V4 and H4 of Figure. 5.9, the area allocated for the proposed active quadrature couplers is highlighted in yellow. As shown in the figure, the coupler is laid out to fit adjacent RF blocks for saving layout area.

Before implementing the BFICs in the phased array, the BFICs are mounted onto an evaluation board to measure non-OTA performances. The fabricated evaluation board is shown in Figure. 5.10. The evaluation board has two inputs for the H- and V-paths and eight outputs for the four H- and four V-ports.

The S-parameters of a single path on the evaluation board in Figure. 5.10 are shown in Figure. 5.11. The input and output ports are well-matched with under 10 dB return loss. The gain covers the full downlink band of the EESS. Although the measured S-parameters include long input and output line effects, the measured performances show that the frequency characteristics are well-controlled and properly modeled.

The BFICs depicted in Figure. 5.9 were integrated into a Ka-band dual circularly

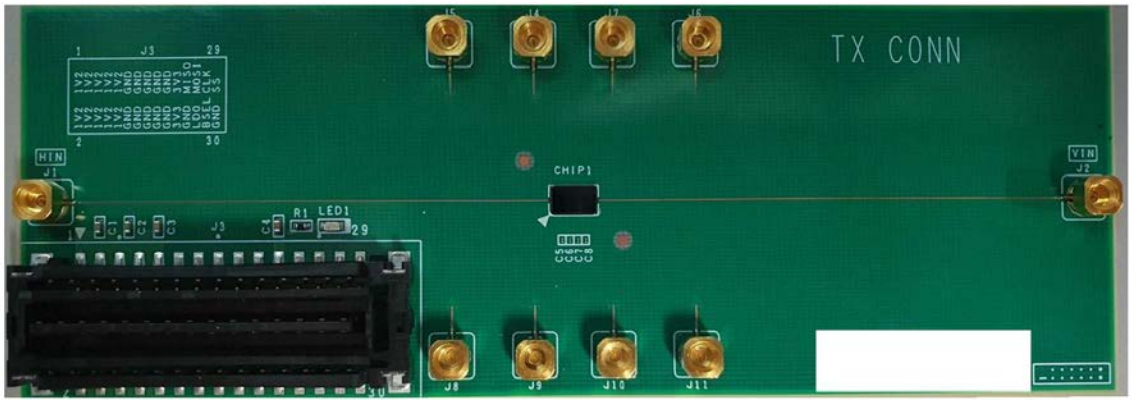

Figure 5.10: Evaluation board for a single path in the proposed Ka-band dual circularly polarized active phased array TX RFIC.

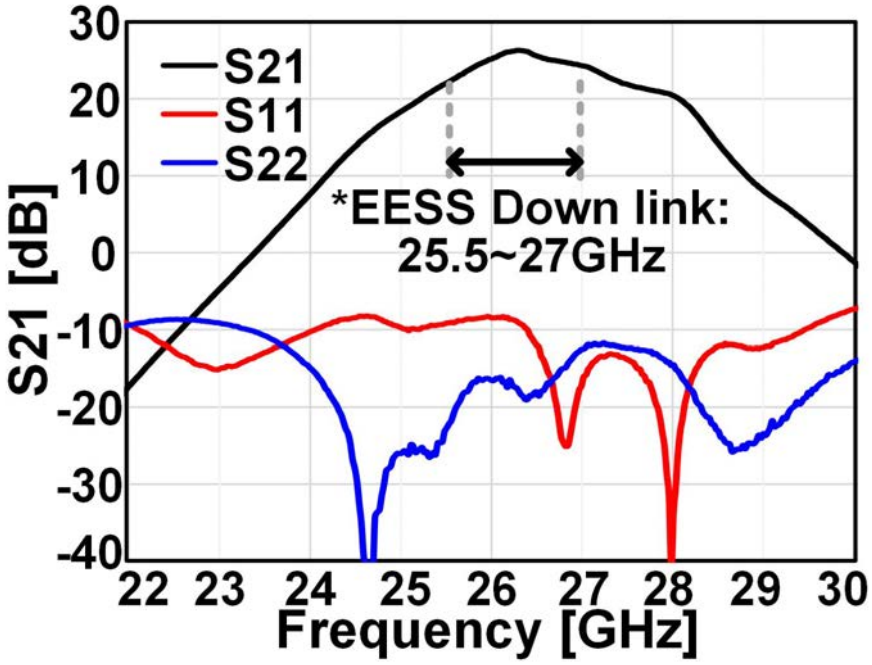

Figure 5.11: Measured S-parameters from evaluation board.

polarized active phased-array TX, as illustrated in Figure. 5.12 and Figure. 5.13. The 64 BFICs were soldered onto the front side of the phased-array TX and were driven by two 64-way T-junction dividers for each H-port and V-port. To efficiently manage the phased-array TX, the 64 ICs were divided into four sections, forming four sub-arrays. Each sub-array was powered separately and controlled via SPI interfaces. Given that the phased array needs to withstand the vibrations experienced during rocket launches, the connectors for power supply and SPI controls were chosen as floating connectors.

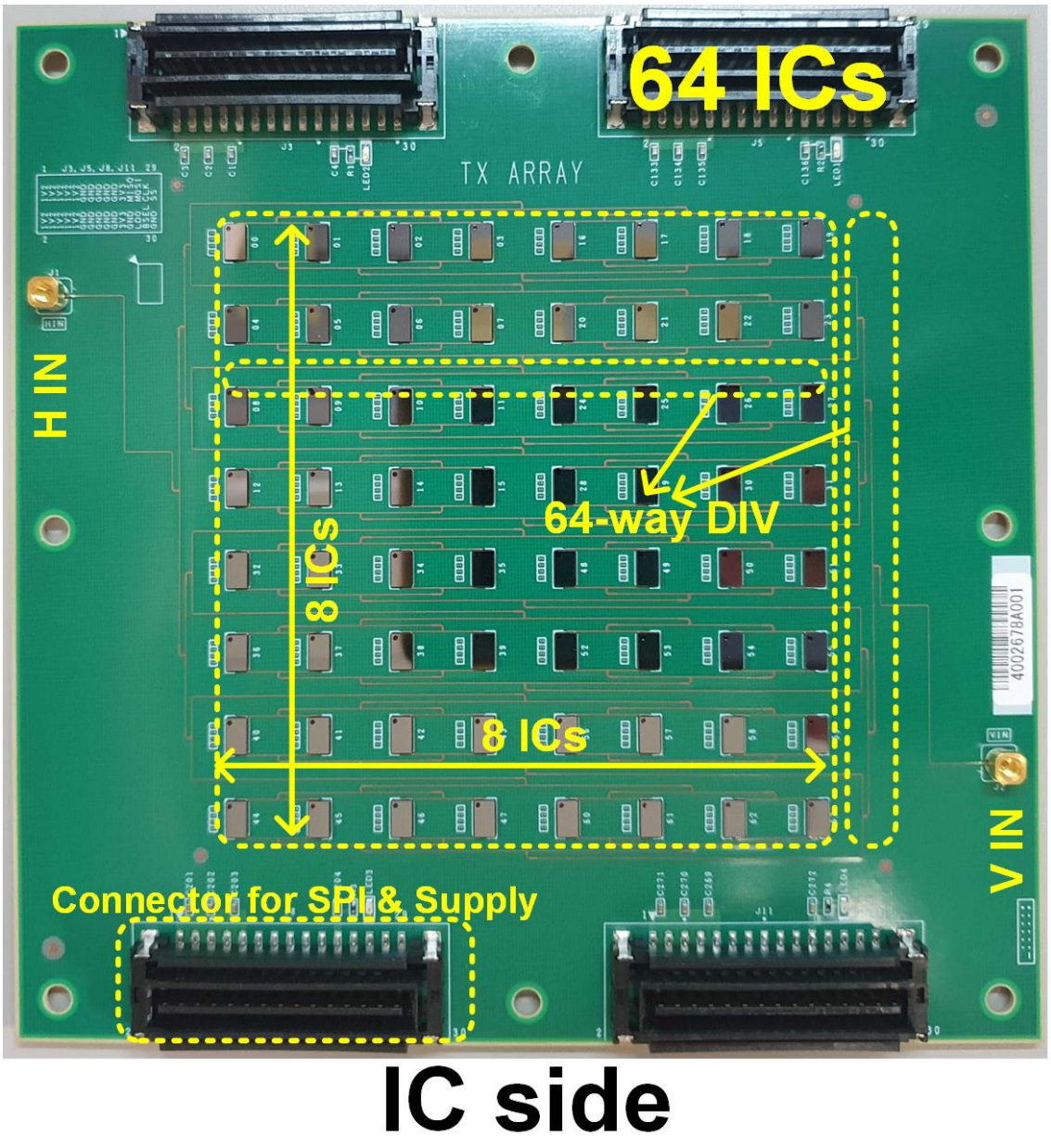

Figure 5.12: Front-side view of the fabricated Ka-band dual circularly polarized active phased array TX

Surface-mount SMPM connectors were implemented for the input port interface.

On the rear side of the phased-array TX, a 256-element antenna array is implemented with a single row of dummy antennas to reduce frequency characteristic differences between edge and inner antennas. The antenna arrays are arranged in a 16×16 array and spaced at $0.94\times\frac{\lambda}{2}$=0.52 mm at 27 GHz to avoid grating lobes at the maximum frequency of the EESS downlink band. As indicated by the solid black box, each 2×2 dual linearly

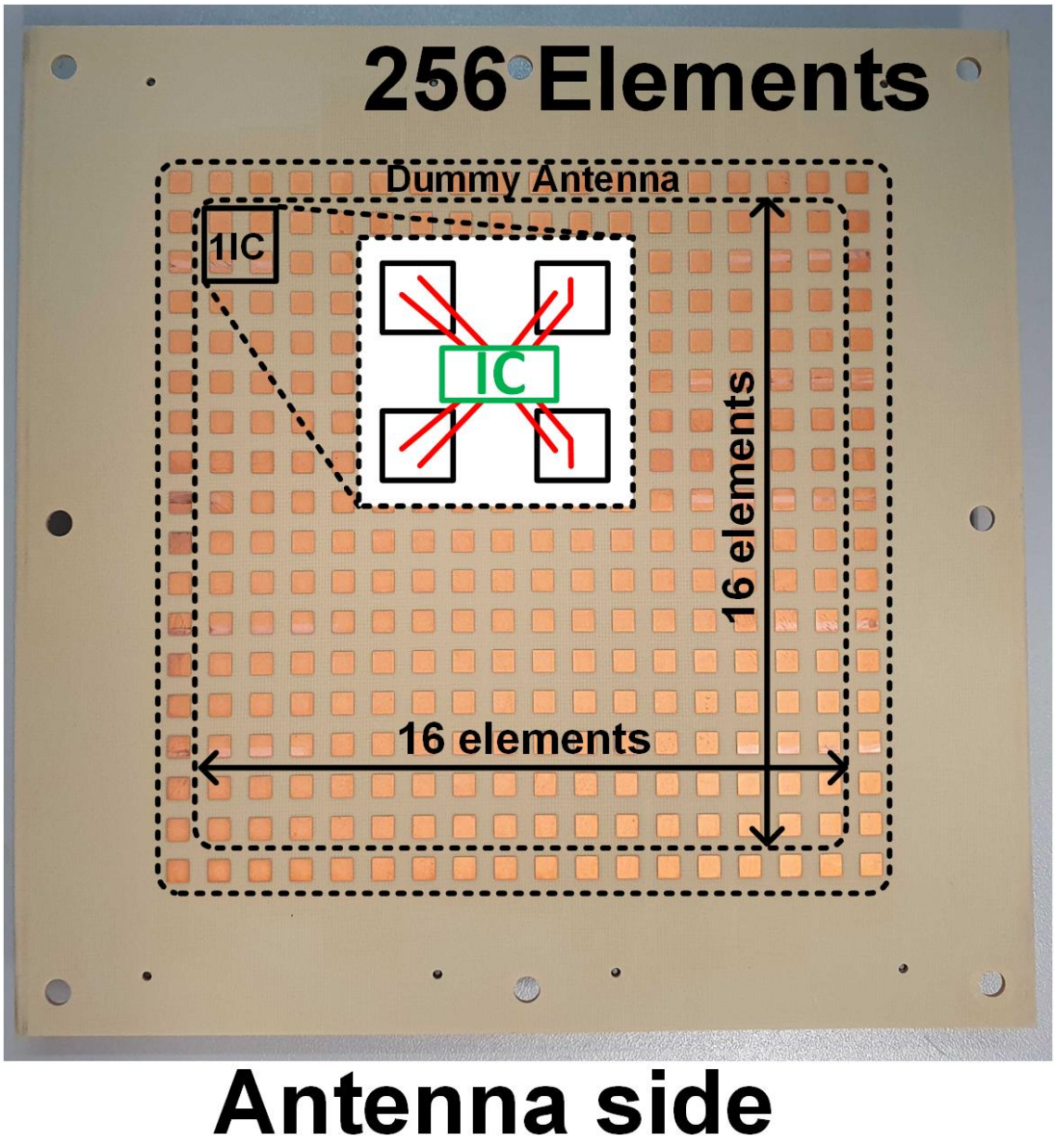

Figure 5.13: Back-side view of the fabricated Ka-band dual circularly polarized active phased array TX

polarized antenna is driven by a single BFIC. To ensure vibration resistance during rocket launch, floated connectors are used for power supply and SPI control, while surface-mount SMPM connectors are used for the input port interface.

Figure. 5.14 illustrates the measured EIRP and DC power consumption performances over swept input power under two different single polarization generation modes: the proposed single circular polarization generation mode and the conventional single circular

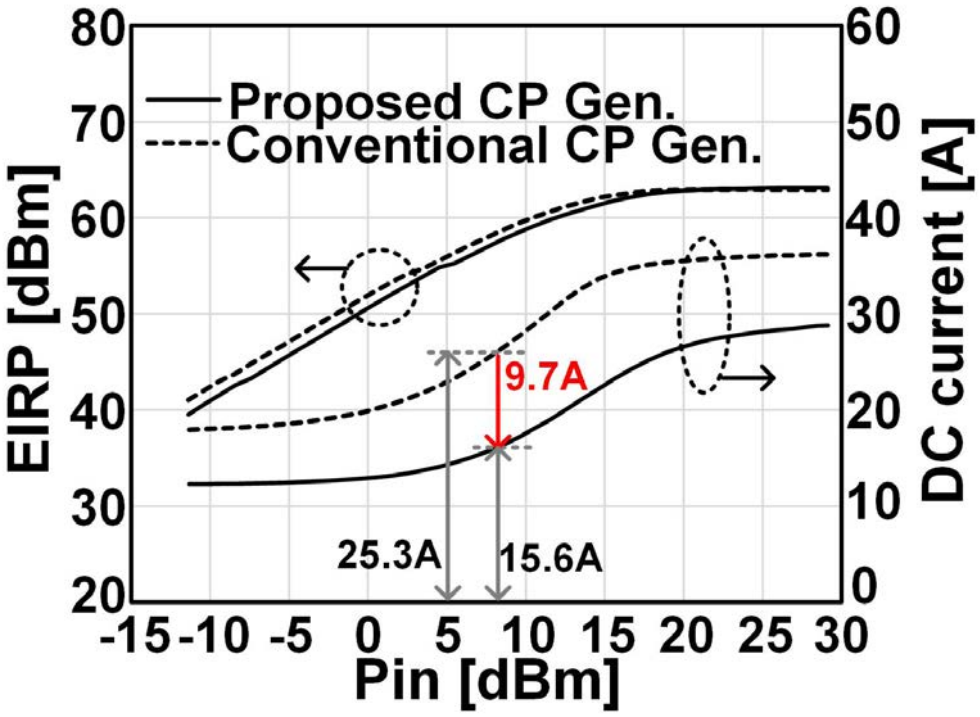

Figure 5.14: Measured EIRP versus swept input power.

polarization mode [7, 8, 83]. The proposed mode utilizes the active quadrature coupler, while the conventional mode employs both H- and V-paths as shown in Figure. 5.3(c) and 5.3(d). As depicted in Figure. 5.14, the gain of the proposed mode is 2 dB lower than the conventional mode, but both modes exhibit the same saturated EIRP. However, the proposed mode exhibits a significant improvement in DC power consumption. At the 6 dB back-off point from the saturated power level, the DC current consumption is reduced by 9.7 A from 25.3 A. Although the PA dominates the total DC power consumption of the TX, in mm-wave CMOS design, a large number of amplifier stages are required to overcome the high loss of the CMOS devices, making the PAs less dominant in total TX DC power consumption.

After measuring the EIRP with a single tone, the beam patterns of the circularly polarized RX horn antenna are measured in Figure. 5.15. The beam patterns are measured at beam directions set to [-50°, -45°, -30°, 0°, 30°, 45°, 50°], and the curves for each beam direction are distinguished by different colors. As shown in the figure, the circularly polarized radiated signals result in clean and well-defined beam patterns, demonstrating that the proposed Ka-band dual circularly polarized active phased-array TX steers the beam accurately.

In addition, the circularly polarized signals' Cross Polarization Discrimination (XPD)

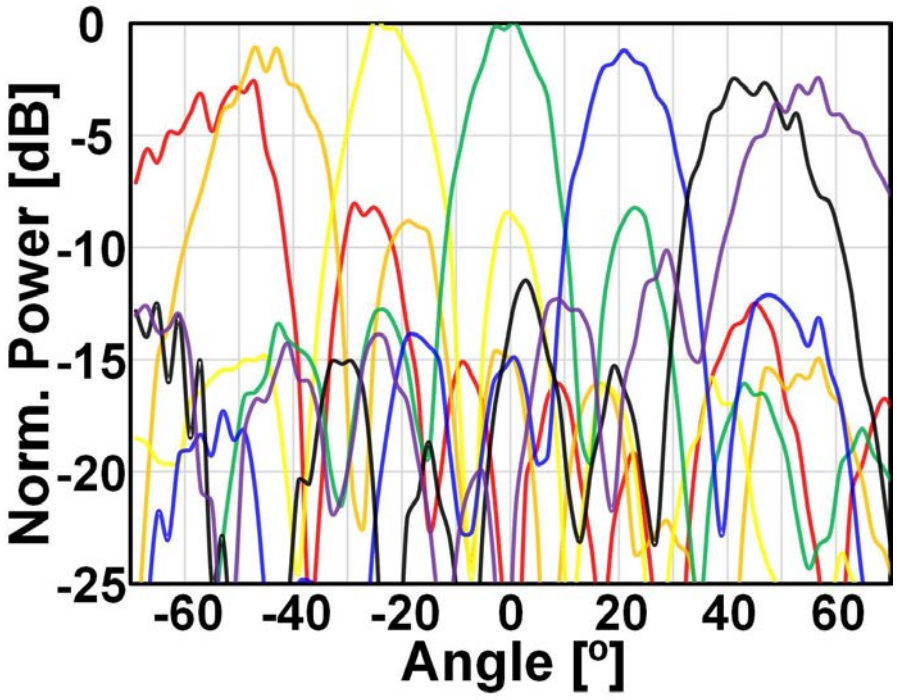

Figure 5.15: Measured beam pattern with circularly polarized signals.

is also measured using a commercially available circularly polarized RX horn antenna during the beam pattern measurements shown in Figure. 5.15. The XPD is determined by measuring the co- and cross-polarized signals and taking the difference between the two signal components. The measured XPD results in Figure. 5.16 are obtained after calibrating the circular polarization using the proposed active quadrature coupler. The results show that the XPD is consistently higher than 30 dB across the entire range of beam steering, with a maximum XPD of 44 dB.

To provide more details, Figure. **??** shows the beam pattern of the co-polarized and cross-polarized signals at 0° beam angle before and after calibration using the proposed active quadrature coupler. The calibration significantly reduces the cross-polarized signal, while there is almost no effect on the co-polarized signal. The solid line with black color represents the beam pattern of the co-polarized signal, the gray dashed line denotes the beam pattern of the cross-polarized signal before calibration, and the black dashed line represents the beam pattern of the cross-polarized signal after calibration. The XPD of the signal at 0° beam angle before calibration is only 16.9 dB, while after calibration, it achieved 43.2 dB of XPD, demonstrating that the proposed active quadrature coupler accurately calibrates the deteriorated XPD.

The TX is not only evaluated with single-tone measurements, but also with modulated

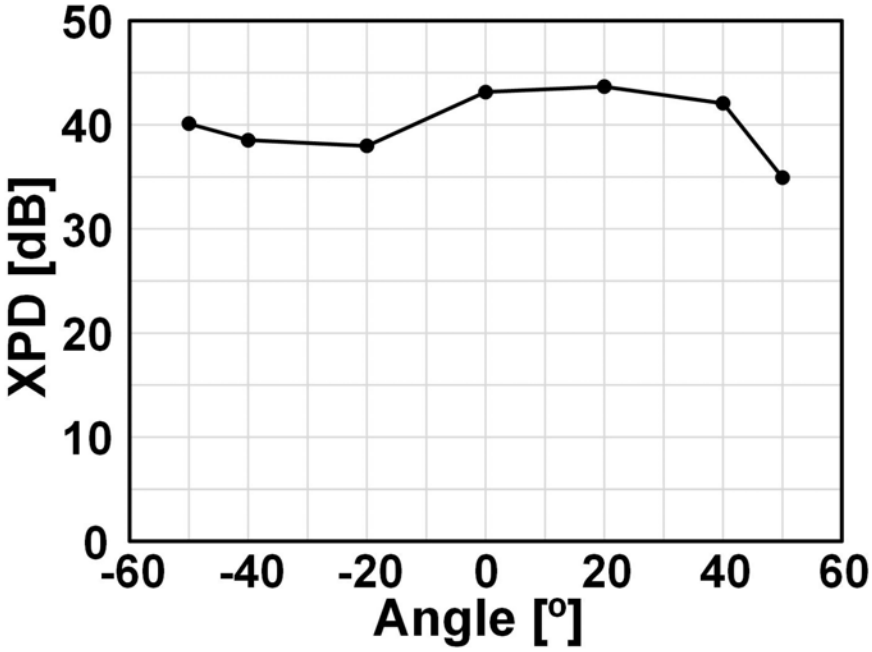

Figure 5.16: Measured XPD over the air.

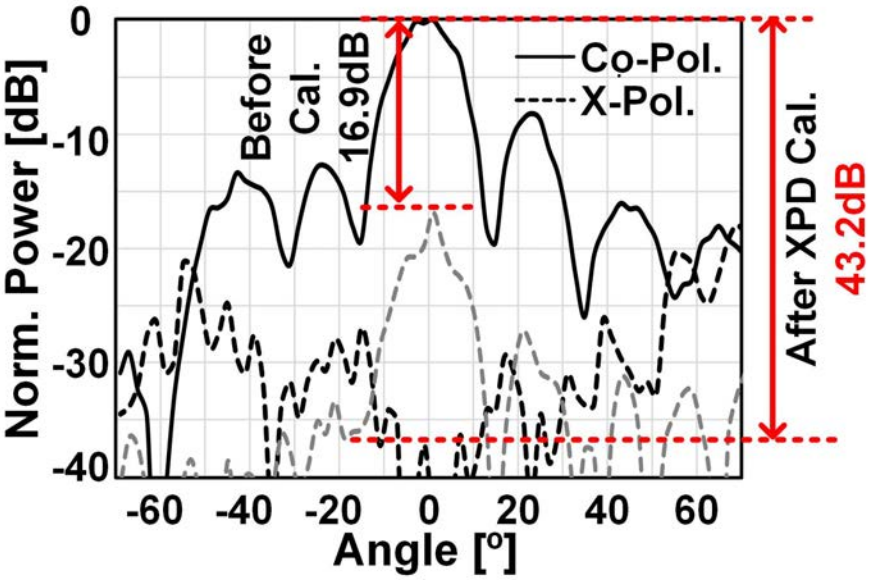

Figure 5.17: Measured pattern of the co-polarized and cross-polarized signals at 0° beam angle.

signals transmitted through free space. Figure. 5.18 shows the measurement setup for the OTA evaluation. The Keysight M8195A arbitrary waveform generator (AWG) generates dual circularly polarized modulated signals, which are upconverted by commercial-off-

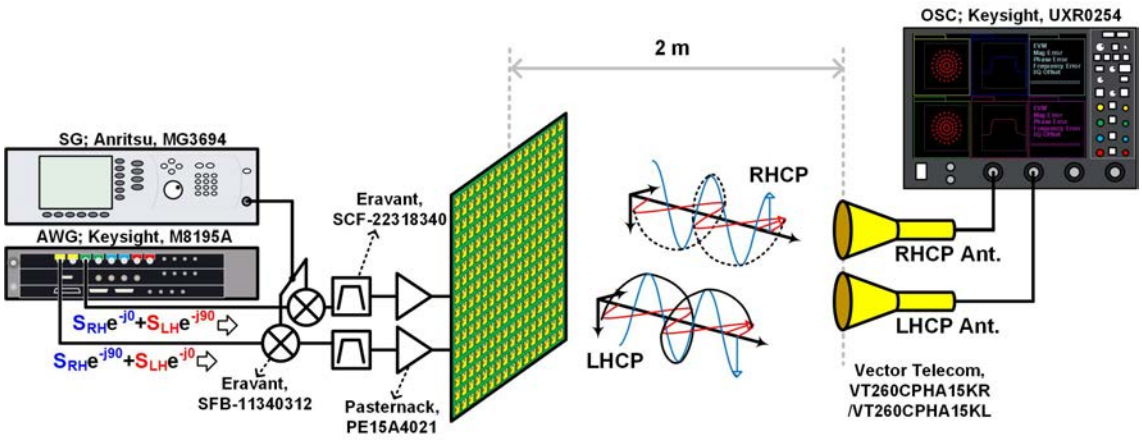

Figure 5.18: Measurement setup for over-the-air measurement.

Single Polarization	64-Element Single CP OTA Meas. with 2GBaud Symbol Rate			
	Modulation	QPSK	32APSK	256APSK
	Constellation	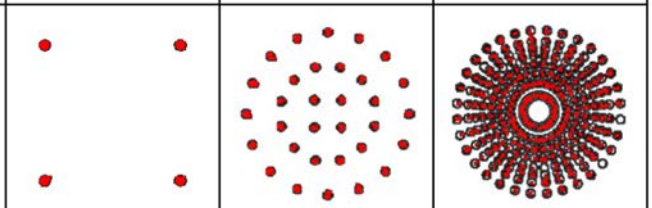		
	Spectrum	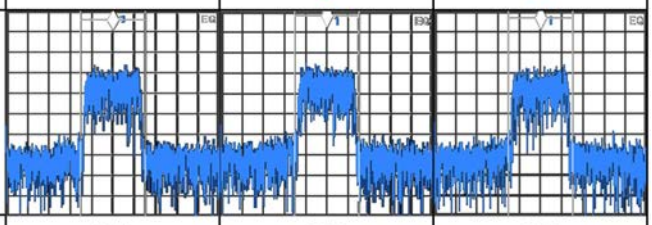		
	ACPR [dB]	35	33	33
	EVM [dB]	-33.7	-32.4	-32.3

Figure 5.19: Measured EVMs with various modulations under single circular polarization mode.

the-shelf mixers and an Anritsu MG3694 signal generator (SG). The external commercial-off-the-shelf power amplifiers (PAs) amplify the power level to drive the device under test (DUT). The DUT is controlled by Python to access the serial peripheral interface (SPI) for switches and bias settings. Two commercial-off-the-shelf circularly polarized horn antennas are placed 2 meters away from the DUT to receive the dual circularly polarized signals. The received signals are then sampled and demodulated by the Keysight UXR0254 oscilloscope.

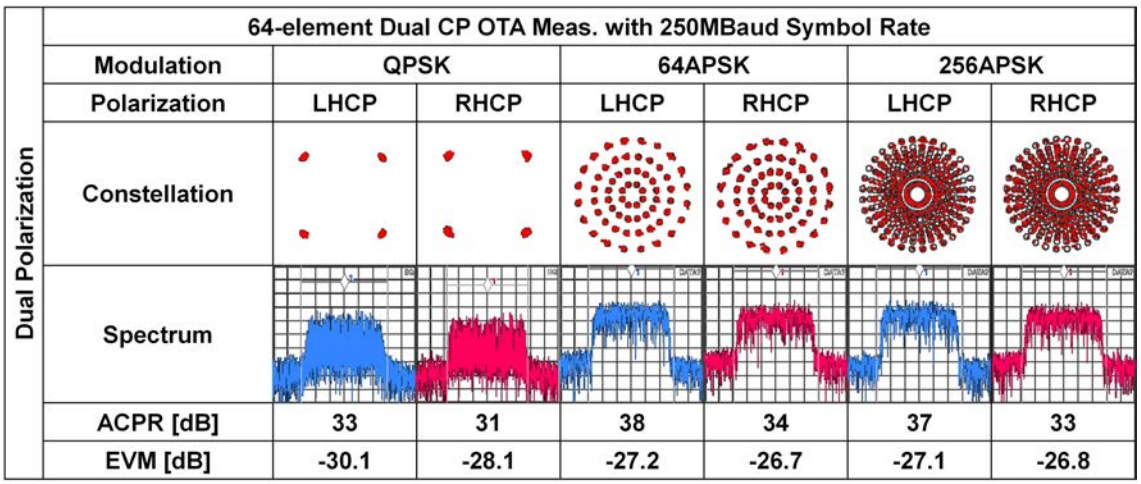

Figure 5.20: Measured EVMs with various modulations under dual circular polarization mode.

Figure. 5.19 presents the measured EVM and constellation data with various modulation schemes at a 2 Gbaud symbol rate, using single circular polarization mode. A 64-element sub-array is utilized for EVM measurement. The results demonstrate that the proposed phased-array TX supports high-order modulation schemes such as 256-APSK, achieving a low EVM of -32.3 dB with a clean spectrum and constellation.

Figure. 5.20 illustrates the EVM results obtained under the dual circularly polarized transmitting mode, where both LHCP and RHCP signals are generated and demodulated simultaneously. The results show that high-order modulation schemes are supported with -27.1 dB and -26.8 dB of EVMs achieved for 256-APSK modulation. However, an important observation needs to be discussed. Although the ACPRs of the signals are achieved at around 35 dB level, the EVMs of the signals are around -27 dB level. Normally, the absolute value of the ACPR becomes the absolute value of the EVM. However, the roughly 12 dB difference between the measured ACPR and the absolute value of the EVM is abnormal and is attributed to the coupling between the LHCP and RHCP signals due to the imperfect XPD in both signals. Despite the higher than expected EVM values, the measured data demonstrate the ability of the proposed Ka-band dual circularly polarized active phased-array TX and the proposed active quadrature coupler to support mm-wave dual circular polarization.

Finally Figure. 5.21 illustrates the benchmark of the phased-array TXs in literature with EIRP versus DC power consumption [6, 7, 19, 21, 28, 77, 83–87]. Almost the phased-array TXs in the literature follow one trend line in EIRP over the DC power consumption curve. This is because the phased-array TXs in the literature focused on maximum PA efficiency design, not efficiency phased array system design. In this work,

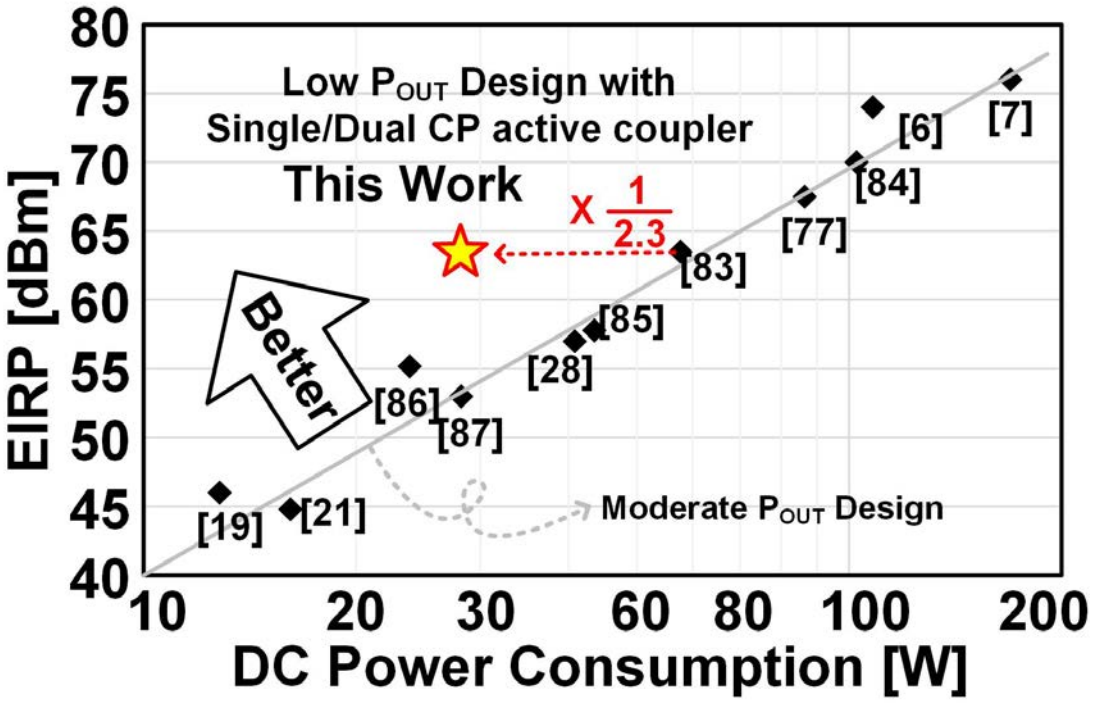

Figure 5.21: Benchmark of the EIRP and DC power consumption of the phased-array TXs in literature.

by taking advantage of the array antenna gain, High EIRP under low DC power consumption is achieved.

5.4 Summary

This chapter discussed two power-saving techniques that aim to overcome the challenges encountered by small LEO satellites. The first technique introduces a systematic array design that reduces power consumption in the LEO satellite constellation. The second technique proposes a novel circular polarization coupler that helps to save redundant DC power in a single circular polarization mode.

Using the two techniques, the proposed system was able to achieve over 35 dB XPD over the scan angle with a single tone and -27.1 dB of dual circularly polarized signal EVM. Additionally, the proposed active quadrature coupler resulted in a 32.3% reduction in DC current consumption. Compared to similar phased-array TXs in the literature, the proposed system was able to achieve the same level of EIRP while consuming only 1/2.3 of the DC power.

The results obtained in this chapter demonstrate that the proposed Ka-band dual cir-

cularly polarized active phased-array TX has achieved high XPD and low-power performances, making it an ideal candidate for the phased-array TX used in LEO small satellite constellations, significantly enhancing their power capabilities.

Chapter 6

Conclusion and Future Work

6.1 Specification Comparison

Figure. 6.1 shows achieved data rate and target data rate comparison. This work successfully drove 256 APSK under dual circular polarization transmitting mode with around 27 dB EVM. However, lack of wide band technique for dual circular polarization made bandwidth is narrower than as targeted. The Symbol rate used in this work is 0.25 GBaud which is as low as one 1/16 times. Throughout the previous discussion, the proposed dual circular polarization technique and circular polarization generation technique are proved prominent techniques for improving the XPD for dual circular polarization, although their bandwidth is small.

Next target specification is to achieve 250 W of DC power consumption with single

Modulation	256APSK	
Polarization	LHCP	RHCP
Constellation		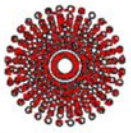
Spectrum	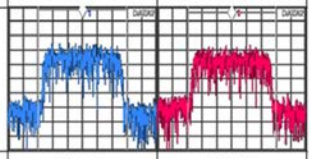	
EVM [dB]	27.1	26.8
Symbol Rate	0.25 GBaud	
Link Speed	4 Gbps	

⇨

Symbol Rate	4 GBaud
Link Speed	64 Gbps

Figure 6.1: Comparison of achieved data rate and target data rate.

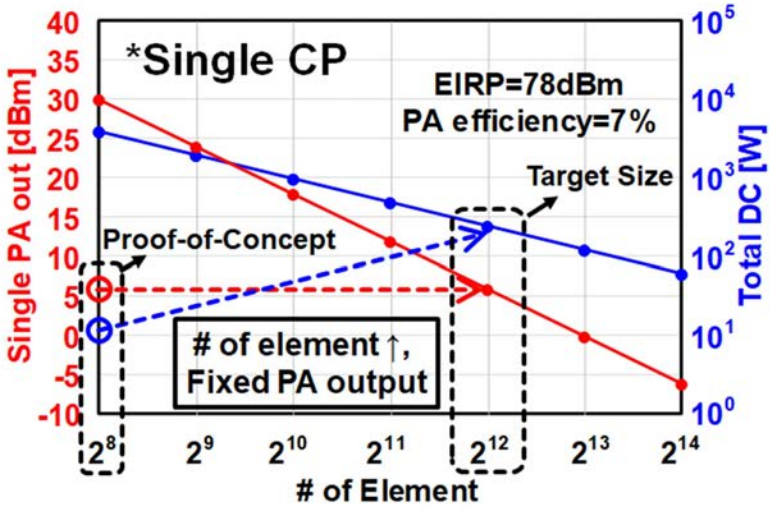

Figure 6.2: Comparison of achieved DC consumption and target DC consumption.

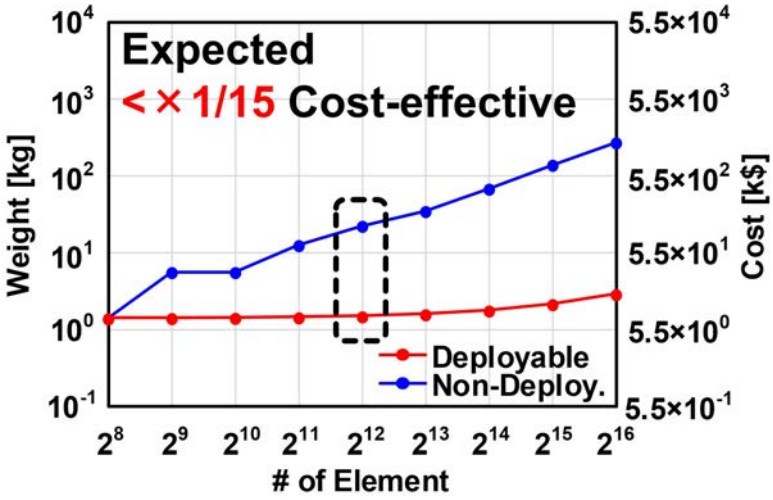

Figure 6.3: Comparison of achieved fabrication cost and target fabrication cost.

circular polarization. Figure. 6.2 illustrates where this work research level is. Two red and blue curves show single power amplifiers output power and total power consumption of the phased array, respectively, over the different number of the elements. With the increasing number of the elements, the total power consumption decreases. In previous chapters, target array size is set to 4096-element. This work implemented 64-element array for the proof-of-concept demonstrating proposed folding method and concept work appropriately. The proof-of-concept phased array achieved 6 dBm single PA power and 15.3 A total array power consumption. By fixing the single PA power and increasing only the number of the elements, 245 W of total array power consumption is expected under

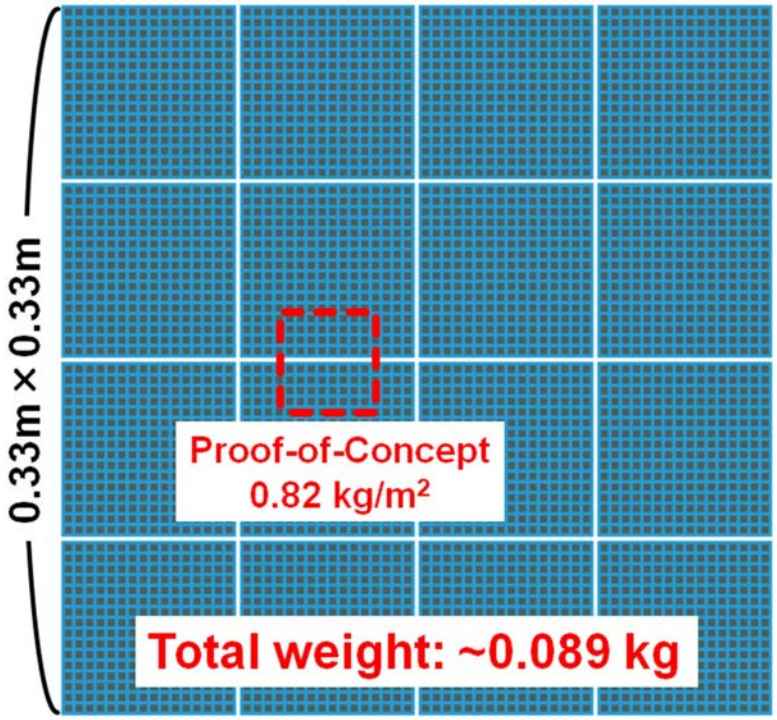

Figure 6.4: Comparison of implemented array size and target implementation size.

48 dBW EIRP.

The fabrication cost or TX weight was one another important design target. The red and blue curves in Figure. 6.3 are weight or cost values over the number of the elements for deployable antenna and non-deployable antenna as visited in previous chapters. The red curve is drawn based on measured areal mass of the 64-element array proof-of-concept. As the target is set 0.1kg, The future 4096-element array is expected achieve less than 0.1 kg weight. Figure. 6.4 illustrate how big the proof-of-concept TX is and where the research level is. Based on the measured areal mass, 0.82 kg/m^2, total weight is 0.089 kg.

Lastly, the efficiency over the beam steering angle is the design target of this work. Figure. 6.5 shows how well the TX efficiency over scan angle is achieved. Before the proposed mmWave load tuning, efficiency drops a lot over the scan angle. However with the proposed mmWave load tuner, their efficiency improved above the 15 % level over the beam scan angle except for -50°. This is because unloaded Q of load tuner is designed bad at -50° setting. The results depict that the proposed technique successfully achieved 15 % of efficiency over scan angle except for -50°.

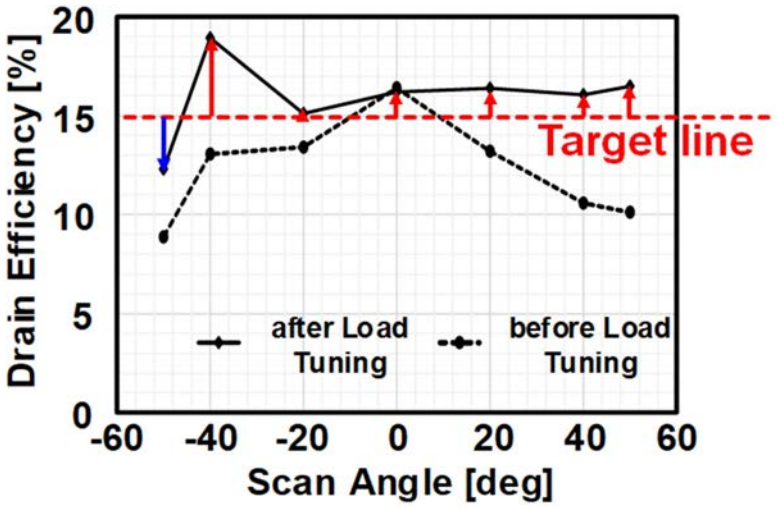

Figure 6.5: Achieved TX efficiency over swept beam angle.

6.2 Conclusion

The application of the LEO small satellite constellation for SATCOM has made significant and widespread contributions to society in various locations worldwide. This paper discusses two representative systems of this constellation: the EESS and the high data rate SATCOM internet. The former provides global monitoring, benefiting early detection and preparation for terrestrial disasters, pollution, and other harmful phenomena on earth. The latter is capable of handling the ever-increasing demand for high data rates and providing seamless connectivity, anytime and anywhere.

To fully leverage the advantages of the SATCOM using LEO small satellite constellation, the design of the transmitter (TX) must fulfill three fundamental requirements: high data throughput, low cost, and low power consumption. Achieving high data throughput is critical for the LEO small satellite SATCOM to keep up with the explosive increase in data demands from both EESS and the high data rate SATCOM internet. Additionally, low cost is a crucial consideration in the construction of the satellite constellation. The third crucial requirement is low-power consumption, as the trend towards smaller satellite bodies for cost reduction makes it necessary to minimize power consumption.

To achieve the aforementioned research objectives of high data throughput, low cost, and low power consumption for the SATCOM using the LEO small satellite constellation, several challenges must be addressed. These challenges include implementing dual circular polarization, utilizing Ka-band frequency, utilizing CMOS technology, utilizing phased array technology, and developing deployable large-size antennas.

This dissertation presents several key techniques and solutions to achieve the high data

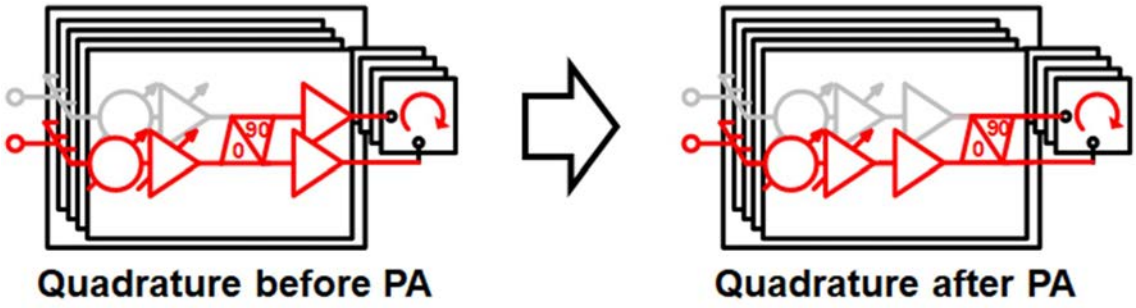

Figure 6.6: A further efficiency improvement method at single circular polarization mode.

throughput, low cost, and low power consumption for the realization of SATCOM using the LEO small satellite constellation. These include the load tuner, circular polarization coupler, and systematic array design for low-power phased-array TX. Additionally, it discusses the implementation of dual circular polarization and Ka-band CMOS phased-array TX to achieve a higher data rate while maintaining low cost and power consumption. Lastly, a new deployable phased array is presented and analyzed, which enhances space efficiency and reduces costs.

In summary, this dissertation presents various techniques and solutions to achieve high data throughput, low cost, and low power consumption for the implementation of the SATCOM utilizing LEO small satellite constellations.

6.3 Future Research

6.3.1 Near Future

As discussed in the previous section, there are some issues not solved yet. For short-term future work, the issues are summarized below.

1. Resolve the EIRP and sidelobe level (SLL) degradation in Figure. 3.14.
2. Increase XPD bandwidth to 4GBaud to support 4 GBaud 256-APSK signal.
3. Improve single circular polarization coupler: -38% → -50%.
4. Implement 4096-element Ka-band dual circularly polarized CMOS deployable active phased array:
   - 1/16 stow rate phased-array TX.
   - Mechanical deformation calibration.

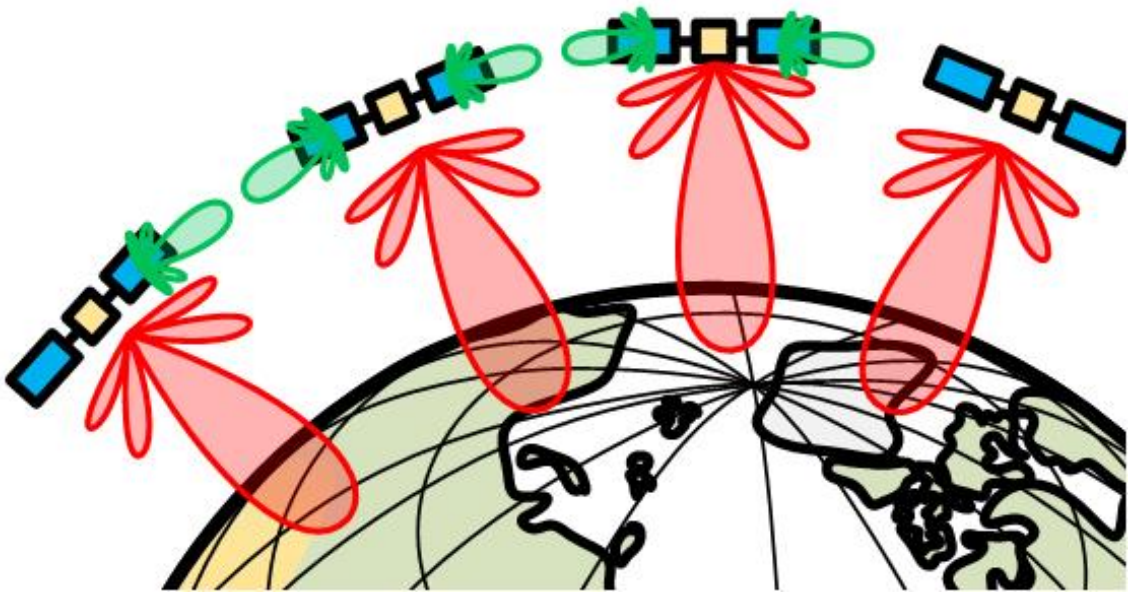

Figure 6.7: The concept of the future LEO small satellite constellation: full connections of ground and satellites including inter-satellite, satellite-ground links.

As discussed in Chapter. 3, there are EIRP and SLL drop in beam pattern results. First step for the short-term future work is to resolve this drop. As next step, widening bandwidth for XPD is required to achieve 4 GBaud bandwidth. The efficiency also can be improved in a large amount with the method shown in Figure. 6.6. Lastly, implementation of the 4096-element phased array is required. With the 4096-element phased array, 1/16 stow rate can be evaluated and mechanical deformation test also can be conducted.

6.3.2 Inter-Satellite Link

In this thesis, only satellite-to-ground communication links are discussed. However, to realize the satellite constellation, not only the satellite-to-ground links but also inter-satellite links are essential as shown in Figure. 6.7. While the work in this thesis focused on requirements for satellite-to-ground links and is well-described, the requirements for inter-satellite links differ from satellite-to-ground links.

The first crucial issue is that an extremely narrow beam angle is required. The LEO satellites fly near the earth surface and parallel to each other satellites, many of the satellites will be captured by a beam from a satellite. The arrival of the beam from unwanted satellites will interrupt communication. If the narrower beam requirement issue is not solved, frequency division multiplexing is required, thus wasting the redundant frequency resources. The second is, although the first issue is solved, the accurate beam control to a wanted satellite with an extremely narrow beam angle.

To overcome the issued aforementioned, not only the much larger size of the array antenna is required but also elaborate gain control between the elements to synthesize the beam shape. In addition to that, a larger array will consume a lot of power. A much more power-efficient design is necessary.

6.3.3 Fast Beam Switching

To avoid frequent satellite handover and ensure smooth communication with fast-moving ground stations, it is essential to have a phased array with a narrower beamwidth that can quickly switch beam direction. One possible solution is to use multi-bank digital control logic, which can store digital control bits for multiple beam directions in different banks. This allows for quick hard-wire control to switch beam direction, without the need for time-consuming hand-shake algorithms. However, this approach assumes that the digital control uses a serial to parallel interface, which may introduce some delay.

Another approach is to use element location marking for each beamforming integrated circuit (BFIC), and use two hard-wires to send analog signals for θ and ϕ beam direction information. The BFICs have ID recognition pads with the same number of bits as the number of BFICs, e.g., for 64 BFICs, six ID recognition pads are required. Each chip digitizes the analog beam direction information and determines the correct phase and amplitude control sets based on the ID bits and digitized beam direction information. This approach only requires the analog beam direction information to be sent, enabling instant beam switching.

6.3.4 Radiation-Hardened Design

In the space environment, radiation including α and γ rays pose significant dangers to electronic circuits, especially phased arrays, which can experience uneven radiation exposure across their area. The degradation of phased-array function, such as beam steering and beam direction, can be a serious problem and can shorten the lifespan of the SATCOM TX, which is important for reducing the number of launches and lowering costs.

Therefore, a careful investigation of the effect of radiation on RF/analog circuits, specifically phased arrays, is necessary. While there have been numerous studies on γ-ray effects on RX phased arrays [88, 89], research on TX phased arrays and α-ray effects is scarce.

In addition to the effects of radiation on circuits, modeling of the radiated circuits is also important, whether at the behavioral or spice-level. Developing a circuit model is essential for successfully addressing radiation-related issues.

After all the technical issues addressed above are solved, the next challenge is the implementation of the radiation-hardened architecture. Either the sense of the radiation effect and amount or the feed input control for correcting the deteriorated performance is required to realize the radiation-hardened phased array system.

6.3.5 Process, Voltage, and Temperature-Insensitive Design

Phased array BFICs are in high demand for constructing inter-satellite and satellite-to-ground links using large-scale phased arrays. However, mass production of the BFICs presents a challenge due to the need for high yield from a wafer. The yield is dependent on process variations in the wafer and lot. To reduce the circuit's susceptibility to process variation, an appropriate feedback system is necessary. Analog feedback is easily implemented in low-frequency analog design due to their adequate feedback speed, but full feedback with mm-wave signals is nearly impossible because silicon transistors cannot support enough feedback gain at mm-wave frequencies.

Supply voltage distribution can be uneven in a large array due to the high current consumption. Even small line resistance can result in a large supply voltage drop. The current flows in a two-dimensional field, leading to uneven current distribution. Designing the supply distribution and power management units with high power efficiency is crucial for mitigating the uneven supply voltage drop.

In addition to dangerous radiation effects, dynamically changing temperature in the space environment is another challenge when building a large phased array system. In space, thermal energy transfer occurs only through the radiation of electromagnetic waves. Areas exposed to sunlight receive a significant amount of thermal energy, resulting in extremely high temperatures, while shaded areas experience extremely low temperatures. This huge temperature difference across the large array causes different performance changes by different elements, resulting in degraded phased array performance.

6.3.6 Integrating all Techniques

To achieve a high data throughput, low-cost, and low-power SATCOM phased array for LEO small satellite constellations, all the aforementioned techniques must be integrated seamlessly. While this thesis has discussed individual techniques, the future advanced phased array systems for LEO small satellite constellations will require the integration of these techniques in a synergistic manner. Only by combining the advancements made in the areas of BFIC mass production, process variation reduction, efficient power management, and thermal management, can a reliable and high-performance phased array be

realized for the LEO small satellite constellation. Therefore, it is crucial to continue researching and developing these areas of study to advance the field of SATCOM phased array systems for LEO small satellite constellations.

Bibliography

[1] T. G. Roberts. Space launch to low earth orbit: How much does it cost? [Online]. Available: https://aerospace.csis.org/data/space-launch-to-low-earth-orbit-how-much-does-it-cost/

[2] D. You, Y. Takahashi, S. Takeda, M. Moritani, H. Hagiwara, S. Koike, H. Lee, Y. Wang, Z. Li, J. Pang, A. Shirane, H. Sakamoto, and K. Okada, "A ka-band 16-element deployable active phased array transmitter for satellite communication," in *2021 IEEE MTT-S International Microwave Symposium (IMS)*, 2021, pp. 799–802.

[3] S. R. Seiler, G. Bazzan, K. Fuchi, E. J. Alanyak, A. S. Gillman, G. W. Reich, P. R. Buskohl, S. Pallampati, D. Sessions, D. Grayson, and G. H. Huff, "Physical reconfiguration of an origami-inspired deployable microstrip patch antenna array," in *2017 IEEE International Symposium on Antennas and Propagation USNC/URSI National Radio Science Meeting*, 2017, pp. 2359–2360.

[4] W. F. Moulder, R. N. Das, A. C. Maccabe, L. A. Bowen, E. M. Thompson, and P. J. Bell, "Rigid-flexible antenna array (rfaa) for lightweight deployable apertures," in *2020 14th European Conference on Antennas and Propagation (EuCAP)*, 2020, pp. 1–5.

[5] D. You, X. Fu, X. Wang, Y. Gao, W. Wang, J. Sakamaki, H. Herdian, S. Kato, M. Ide, Y. Zhang, A. A. Fadila, Z. Li, C. Wang, Y. Wang, J. Sudo, M. Higaki, N. Kawaguchi, M. Nitta, S. Inoue, T. Eishima, T. Tomura, J. Pang, H. Sakai, K. Okada, and A. Shirane, "19.4 a small-satellite-mounted 256-element ka-band cmos phased-array transmitter achieving 63.8dbm eirp under 26.6w power consumption using single/dual circular polarization active coupler," in *2023 IEEE International Solid- State Circuits Conference (ISSCC)*, 2023, pp. 298–300.

[6] X. Luo, J. Ouyang, Z.-H. Chen, Y. Yan, L. Han, Z. Wu, T. Yu, and K. Zheng, "A scalable ka-band 1024-element transmit dual-circularly-polarized planar phased array for satcom application," *IEEE Access*, vol. 8, pp. 156 084–156 095, 2020.

[7] K. K. W. Low, S. Zihir, T. Kanar, and G. M. Rebeiz, "A 27–31-ghz 1024-element ka-band satcom phased-array transmitter with 49.5-dbw peak eirp, 1-db ar, and ±70° beam scanning," *IEEE Transactions on Microwave Theory and Techniques*, vol. 70, no. 3, pp. 1757–1768, 2022.

[8] D. You, Y. Wang, X. Fu, H. Herdian, X. Wang, A. Fadila, H. Lee, M. Ide, S. Kato, Z. Li, J. Pang, A. Shirane, and K. Okada, "A ka- band dual circularly polarized cmos transmitter with adaptive scan impedance tuner and active xpd calibration technique for satellite terminal," in *2022 IEEE Radio Frequency Integrated Circuits Symposium (RFIC)*, 2022, pp. 15–18.

[9] C. Marcu, D. Chowdhury, C. Thakkar, J.-D. Park, L.-K. Kong, M. Tabesh, Y. Wang, B. Afshar, A. Gupta, A. Arbabian, S. Gambini, R. Zamani, E. Alon, and A. M. Niknejad, "A 90 nm cmos low-power 60 ghz transceiver with integrated baseband circuitry," *IEEE Journal of Solid-State Circuits*, vol. 44, no. 12, pp. 3434–3447, 2009.

[10] A. Binaie, S. Ahasan, A. Dascurcu, M. B. Dastjerdi, R. Garg, M. Johnson, A. Galioglu, A. Natarajan, and H. Krishnaswamy, "A scalable 60ghz 4-element mimo transmitter with a frequency-domain-multiplexing single-wire interface and harmonic-rejection-based de-multiplexing," in *2020 IEEE Radio Frequency Integrated Circuits Symposium (RFIC)*, 2020, pp. 1–4.

[11] B. Razavi, Z. Soe, A. Tham, J. Chen, D. Dai, M. Lu, A. Khalil, H. Ma, I. Lakkis, and H. Law, "A low-power 60-ghz cmos transceiver for wigig applications," in *2013 Symposium on VLSI Circuits*, 2013, pp. C300–C301.

[12] K. Okada, K. Kondou, M. Miyahara, M. Shinagawa, H. Asada, R. Minami, T. Yamaguchi, A. Musa, Y. Tsukui, Y. Asakura, S. Tamonoki, H. Yamagishi, Y. Hino, T. Sato, H. Sakaguchi, N. Shimasaki, T. Ito, Y. Takeuchi, N. Li, Q. Bu, R. Murakami, K. Bunsen, K. Matsushita, M. Noda, and A. Matsuzawa, "A full 4-channel 6.3gb/s 60ghz direct-conversion transceiver with low-power analog and digital baseband circuitry," in *2012 IEEE International Solid-State Circuits Conference*, 2012, pp. 218–220.

[13] V. Vidojkovic, V. Szortyka, K. Khalaf, G. Mangraviti, S. Brebels, W. van Thillo, K. Vaesen, B. Parvais, V. Issakov, M. Libois, M. Matsuo, J. Long, C. Soens, and P. Wambacq, "A low-power radio chipset in 40nm lp cmos with beamforming for 60ghz high-data-rate wireless communication," in *2013 IEEE International Solid-State Circuits Conference Digest of Technical Papers*, 2013, pp. 236–237.

[14] Y. Wang, B. Liu, H. Liu, A. T. Narayanan, J. Pang, N. Li, T. Yoshioka, Y. Terashima, H. Zhang, D. Tang, M. Katsuragi, D. Lee, S. Choi, R. Wu, K. Okada, and A. Matsuzawa, "A 100mw 3.0 gb/s spectrum efficient 60 ghz bi-phase ook cmos transceiver," in *2017 Symposium on VLSI Circuits*, 2017, pp. C298–C299.

[15] K. Dasgupta, S. Daneshgar, C. Thakkar, S. Kang, A. Chakrabarti, S. Yamada, N. Narevsky, D. Choudhury, J. E. Jaussi, and B. Casper, "A 60-ghz transceiver and baseband with polarization mimo in 28-nm cmos," *IEEE Journal of Solid-State Circuits*, vol. 53, no. 12, pp. 3613–3627, 2018.

[16] T. Sowlati, S. Sarkar, B. G. Perumana, W. L. Chan, A. Papio Toda, B. Afshar, M. Boers, D. Shin, T. R. Mercer, W.-H. Chen, A. Grau Besoli, S. Yoon, S. Kyriazidou, P. Yang, V. Aggarwal, N. Vakilian, D. Rozenblit, M. Kahrizi, J. Zhang, A. Wang, P. Sen, D. Murphy, A. Sajjadi, A. Mehrabani, E. Kornaros, K. Low, K. Kimura, V. Roussel, H. Xie, and V. Kodavati, "A 60-ghz 144-element phased-array transceiver for backhaul application," *IEEE Journal of Solid-State Circuits*, vol. 53, no. 12, pp. 3640–3659, 2018.

[17] B. Sadhu, A. Valdes-Garcia, J.-O. Plouchart, H. Ainspan, A. K. Gupta, M. Ferriss, M. Yeck, M. Sanduleanu, X. Gu, C. W. Baks, D. Liu, and D. Friedman, "A 250-mw 60-ghz cmos transceiver soc integrated with a four-element aip providing broad angular link coverage," *IEEE Journal of Solid-State Circuits*, vol. 55, no. 6, pp. 1516–1529, 2020.

[18] M. Boers, B. Afshar, I. Vassiliou, S. Sarkar, S. T. Nicolson, E. Adabi, B. G. Perumana, T. Chalvatzis, S. Kavvadias, P. Sen, W. L. Chan, A. H.-T. Yu, A. Parsa, M. Nariman, S. Yoon, A. G. Besoli, C. A. Kyriazidou, G. Zochios, J. A. Castaneda, T. Sowlati, M. Rofougaran, and A. Rofougaran, "A 16tx/16rx 60 ghz 802.11ad chipset with single coaxial interface and polarization diversity," *IEEE Journal of Solid-State Circuits*, vol. 49, no. 12, pp. 3031–3045, 2014.

[19] K. Kibaroglu, M. Sayginer, and G. M. Rebeiz, "A low-cost scalable 32-element 28-ghz phased array transceiver for 5g communication links based on a 2×2 beamformer flip-chip unit cell," *IEEE Journal of Solid-State Circuits*, vol. 53, no. 5, pp. 1260–1274, 2018.

[20] L. Wu, H. F. Leung, A. Li, Z. Hong, Y. Qin, and H. C. Luong, "A 4-element 60-ghz cmos phased-array receiver with transformer-based hybrid-mode mixing and closed-loop beam-forming calibration," in *2013 Symposium on VLSI Circuits*, 2013, pp. C296–C297.

[21] J. Pang, Z. Li, R. Kubozoe, X. Luo, R. Wu, Y. Wang, D. You, A. A. Fadila, R. Saengchan, T. Nakamura, J. Alvin, D. Matsumoto, B. Liu, A. T. Narayanan, J. Qiu, H. Liu, Z. Sun, H. Huang, K. K. Tokgoz, K. Motoi, N. Oshima, S. Hori, K. Kunihiro, T. Kaneko, A. Shirane, and K. Okada, "A 28-ghz cmos phased-array beamformer utilizing neutralized bi-directional technique supporting dual-polarized mimo for 5g nr," *IEEE Journal of Solid-State Circuits*, vol. 55, no. 9, pp. 2371–2386, 2020.

[22] H.-T. Kim, B.-S. Park, S.-S. Song, T.-S. Moon, S.-H. Kim, J.-M. Kim, J.-Y. Chang, and Y.-C. Ho, "A 28-ghz cmos direct conversion transceiver with packaged 2×4 antenna array for 5g cellular system," *IEEE Journal of Solid-State Circuits*, vol. 53, no. 5, pp. 1245–1259, 2018.

[23] B. Sadhu, Y. Tousi, J. Hallin, S. Sahl, S. K. Reynolds, Ö. Renström, K. Sjögren, O. Haapalahti, N. Mazor, B. Bokinge *et al.*, "A 28-ghz 32-element trx phased-array ic with concurrent dual-polarized operation and orthogonal phase and gain control for 5g communications," *IEEE Journal of Solid-State Circuits*, vol. 52, no. 12, pp. 3373–3391, 2017.

[24] J.-L. Kuo, Y.-F. Lu, T.-Y. Huang, Y.-L. Chang, Y.-K. Hsieh, P.-J. Peng, I.-C. Chang, T.-C. Tsai, K.-Y. Kao, W.-Y. Hsiung, J. Wang, Y. A. Hsu, K.-Y. Lin, H.-C. Lu, Y.-C. Lin, L.-H. Lu, T.-W. Huang, R.-B. Wu, and H. Wang, "60-ghz four-element phased-array transmit/receive system-in-package using phase compensation techniques in 65-nm flip-chip cmos process," *IEEE Transactions on Microwave Theory and Techniques*, vol. 60, no. 3, pp. 743–756, 2012.

[25] H. Krishnaswamy and H. Hashemi, "A fully integrated 24ghz 4-channel phased-array transceiver in 0.13m cmos based on a variable-phase ring oscillator and pll architecture," in *2007 IEEE International Solid-State Circuits Conference. Digest of Technical Papers*, 2007, pp. 124–591.

[26] T.-S. Chu and H. Hashemi, "True-time-delay-based multi-beam arrays," *IEEE Transactions on Microwave Theory and Techniques*, vol. 61, no. 8, pp. 3072–3082, 2013.

[27] K. Khalaf, K. Vaesen, S. Brebels, G. Mangraviti, M. Libois, C. Soens, W. Van Thillo, and P. Wambacq, "A 60-ghz 8-way phased-array front-end with t/r switching and calibration-free beamsteering in 28-nm cmos," *IEEE Journal of Solid-State Circuits*, vol. 53, no. 7, pp. 2001–2011, 2018.

[28] J. D. Dunworth, A. Homayoun, B.-H. Ku, Y.-C. Ou, K. Chakraborty, G. Liu, T. Segoria, J. Lerdworatawee, J. W. Park, H.-C. Park, H. Hedayati, D. Lu, P. Monat, K. Douglas, and V. Aparin, "A 28ghz bulk-cmos dual-polarization phased-array transceiver with 24 channels for 5g user and basestation equipment," in *2018 IEEE International Solid - State Circuits Conference - (ISSCC)*, 2018, pp. 70–72.

[29] A. Natarajan, A. Komijani, X. Guan, A. Babakhani, and A. Hajimiri, "A 77-ghz phased-array transceiver with on-chip antennas in silicon: Transmitter and local lo-path phase shifting," *IEEE Journal of Solid-State Circuits*, vol. 41, no. 12, pp. 2807–2819, 2006.

[30] J. Pang, R. Wu, Y. Wang, M. Dome, H. Kato, H. Huang, A. Tharayil Narayanan, H. Liu, B. Liu, T. Nakamura, T. Fujimura, M. Kawabuchi, R. Kubozoe, T. Miura, D. Matsumoto, Z. Li, N. Oshima, K. Motoi, S. Hori, K. Kunihiro, T. Kaneko, A. Shirane, and K. Okada, "A 28-ghz cmos phased-array transceiver based on lo phase-shifting architecture with gain invariant phase tuning for 5g new radio," *IEEE Journal of Solid-State Circuits*, vol. 54, no. 5, pp. 1228–1242, 2019.

[31] A. G. Roy, O. Inac, A. Singh, T. Mukatel, O. Brandelstein, T. W. Brown, S. Abughazaleh, J. S. Hayden, B. Park, G. Bachmanek, T.-Y. J. Kao, J. Hagn, S. Dalmia, D. Shoham, B. Davis, I. Fisher, R. Sover, A. Freiman, B. Xiao, B. Singh, and J. Jensen, "A 37-40 ghz phased array front-end with dual polarization for 5g mimo beamforming applications," in *2019 IEEE Radio Frequency Integrated Circuits Symposium (RFIC)*, 2019, pp. 251–254.

[32] Y. Wang, R. Wu, J. Pang, D. You, A. A. Fadila, R. Saengchan, X. Fu, D. Matsumoto, T. Nakamura, R. Kubozoe, M. Kawabuchi, B. Liu, H. Zhang, J. Qiu, H. Liu, W. Deng, N. Oshima, K. Motoi, S. Hori, K. Kunihiro, T. Kaneko, A. Shirane, and K. Okada, "A 39ghz 64-element phased-array cmos transceiver with built-in calibration for large-array 5g nr," in *2019 IEEE Radio Frequency Integrated Circuits Symposium (RFIC)*, 2019, pp. 279–282.

[33] M. Johnson, A. Dascurcu, K. Zhan, A. Galioglu, N. K. Adepu, S. Jain, H. Krishnaswamy, and A. S. Natarajan, "Code-domain multiplexing for shared if/lo interfaces in millimeter-wave mimo arrays," *IEEE Journal of Solid-State Circuits*, vol. 55, no. 5, pp. 1270–1281, 2020.

[34] M.-Y. Huang and H. Wang, "A mm-wave wideband mimo rx with instinctual array-based blocker/signal management for ultralow-latency communication," *IEEE Journal of Solid-State Circuits*, vol. 54, no. 12, pp. 3553–3564, 2019.

[35] N. S. Mannem, M.-Y. Huang, T.-Y. Huang, and H. Wang, "A reconfigurable hybrid series/parallel doherty power amplifier with antenna vswr resilient performance for mimo arrays," *IEEE Journal of Solid-State Circuits*, vol. 55, no. 12, pp. 3335–3348, 2020.

[36] M. Kalantari, H. Shirinabadi, A. Fotowat-Ahmadi, and C. P. Yue, "4.7 a single-antenna w-band fmcw radar front-end utilizing adaptive leakage cancellation," in *2020 IEEE International Solid- State Circuits Conference - (ISSCC)*, 2020, pp. 88–90.

[37] H. Jia, L. Kuang, W. Zhu, Z. Wang, F. Ma, Z. Wang, and B. Chi, "A 77 ghz frequency doubling two-path phased-array fmcw transceiver for automotive radar," *IEEE Journal of Solid-State Circuits*, vol. 51, no. 10, pp. 2299–2311, 2016.

[38] D. Guermandi, Q. Shi, A. Dewilde, V. Derudder, U. Ahmad, A. Spagnolo, I. Ocket, A. Bourdoux, P. Wambacq, J. Craninckx, and W. Van Thillo, "A 79-ghz 2×2 mimo pmcw radar soc in 28-nm cmos," *IEEE Journal of Solid-State Circuits*, vol. 52, no. 10, pp. 2613–2626, 2017.

[39] A. Townley, P. Swirhun, D. Titz, A. Bisognin, F. Gianesello, R. Pilard, C. Luxey, and A. M. Niknejad, "A 94-ghz 4tx–4rx phased-array fmcw radar transceiver with antenna-in-package," *IEEE Journal of Solid-State Circuits*, vol. 52, no. 5, pp. 1245–1259, 2017.

[40] [Online]. Available: http://www.itrs2.net/itrs-reports.html.

[41] N. Saito, T. Tsukizawa, N. Shirakata, T. Morita, K. Tanaka, J. Sato, Y. Morishita, M. Kanemaru, R. Kitamura, T. Shima, T. Nakatani, K. Miyanaga, T. Urushihara, H. Yoshikawa, T. Sakamoto, H. Motozuka, Y. Shirakawa, N. Yosoku, A. Yamamoto, R. Shiozaki, and K. Takinami, "A fully integrated 60-ghz cmos transceiver chipset based on wigig/ieee 802.11ad with built-in self calibration for mobile usage," *IEEE Journal of Solid-State Circuits*, vol. 48, no. 12, pp. 3146–3159, 2013.

[42] M. Boers, I. Vassiliou, S. Sarkar, S. Nicolson, E. Adabi, B. Afshar, B. Perumana, T. Chalvatzis, S. Kavadias, P. Sen, W. L. Chan, A. Yu, A. Parsa, M. Nariman, S. Yoon, A. G. Besoli, C. Kyriazidou, G. Zochios, N. Kocaman, A. Garg, H. Eberhart, P. Yang, H. Xie, H. J. Kim, A. Tarighat, D. Garrett, A. Blanksby, M. K. Wong, D. P. Thirupathi, S. Mak, R. Srinivasan, A. Ibrahim, E. Sengul, V. Roussel, P.-C. Huang, T. Yeh, M. Mese, J. Castaneda, B. Ibrahim, T. Sowlati, M. Rofougaran, and

A. Rofougaran, "20.2 a 16tx/16rx 60ghz 802.11ad chipset with single coaxial interface and polarization diversity," in *2014 IEEE International Solid-State Circuits Conference Digest of Technical Papers (ISSCC)*, 2014, pp. 344–345.

[43] T. Sowlati, S. Sarkar, B. Perumana, W. L. Chan, B. Afshar, M. Boers, D. Shin, T. Mercer, W.-H. Chen, A. P. Toda, A. G. Besoli, S. Yoon, S. Kyriazidou, P. Yang, V. Aggarwal, N. Vakilian, D. Rozenblit, M. Kahrizi, J. Zhang, A. Wang, P. Sen, D. Murphy, M. Mikhemar, A. Sajjadi, A. Mehrabani, B. Ibrahim, B. Pan, K. Juan, S. Xu, C. Guan, G. Geshvindman, K. Low, N. Kocaman, H. Eberhart, K. Kimura, I. Elgorriaga, V. Roussel, H. Xie, L. Shi, and V. Kodavati, "A 60ghz 144-element phased-array transceiver with 51dbm maximum eirp and ±60° beam steering for backhaul application," in *2018 IEEE International Solid - State Circuits Conference - (ISSCC)*, 2018, pp. 66–68.

[44] Q. Gu, *RF System Design Of Transceivers For Wireless Communications*. Spring Street, NY, USA: Springer, 2005.

[45] B. Razavi, *RF Microelectronics*, 2nd ed. Castleton, NY, USA: Michelle Housley, 2011.

[46] T. K. Roy, M. F. Pervej, and M. Morshed, "Performance comparison of three optimized alternative pulse shaping filters with the raised cosine filter for wireless applications," in *2015 International Conference on Computer and Information Engineering (ICCIE)*, 2015, pp. 9–12.

[47] "Fixed radio systems; point-to-point and point-to-multipoint equipment; use of circular polarization in multipoint systems; part 1: Systems aspects," Europian Telecommunications Standards Institute, Sophia Antipolis, France, Tech. Rep. TR 102 031-1, January 2006. [Online]. Available: https://www.etsi.org/deliver/etsi_tr/102000_102099/10203101/01.01.01_60/tr_10203101v010101p.pdf

[48] T. J. L. J. S. Hollis and L. C. Jr., "Polarization theory," in *Microwave Antenna Measurements*, T. J. L. J. S. Hollis and J. L. C. Jr., Eds. Atlanta, GA, USA: Scientific-Atlanta, Inc, 1985, pp. 1–50.

[49] "Dvb-s2x," Tech. Rep. ETSI EN 302 307-2, 4 2021. [Online]. Available: https://www.etsi.org/deliver/etsi_en/302300_302399/30230702/01.03.01_20/en_30230702v010301a.pdf

[50] K. Ikeya, H. Sakamoto, H. Nakanishi, H. Furuya, T. Tomura, R. Ide, R. Iijima, Y. Iwasaki, K. Ohno, K. Omoto, T. Furuya, T. Hayashi, M. Kato, S. Koide,

M. Kurosaki, Y. Nakatsuka, S. Okuyama, R. Kashiyama, J. Nakamura, W. Nio, T. Tsunemitsu, Y. Yamazaki, K. Taga, B. Hohmann, T. Amamoto, T. Chubachi, S. Tamura, H. Okada, A. Watanabe, N. Kawabata, T. Hori, H. Ito, T. Kuratomi, Y. Shimoda, N. Hidaka, K. Watanabe, A. Torisaka, and M. Yamazaki, "Significance of 3u cubesat origamisat-1 for space demonstration of multifunctional deployable membrane," *Acta Astronautica*, vol. 173, pp. 363–377, 2020. [Online]. Available: https://www.sciencedirect.com/science/article/pii/S0094576520302204

[51] "Propagation data and prediction methods required for the design of earth-space telecommunication systems," Tech. Rep. P.618-13, 12 2017. [Online]. Available: https://www.itu.int/rec/R-REC-P.618/

[52] "Characteristics of precipitation for propagation modeling," Tech. Rep. P.837-7, 6 2017. [Online]. Available: https://www.itu.int/rec/R-REC-P.837

[53] "Specific attenuation model for rain for use in prediction methods," Tech. Rep. P.838-3, 3 2005. [Online]. Available: https://www.itu.int/rec/R-REC-P.838

[54] "Rain height model for prediction methods," Tech. Rep. P.839-4, 9 2013. [Online]. Available: https://www.itu.int/rec/R-REC-P.839

[55] "Rain height model for prediction methods," Tech. Rep. P.1511-2, 8 2019. [Online]. Available: https://www.itu.int/rec/R-REC-P.1511

[56] A. Fikes, O. S. Mizrahi, and A. Hajimiri, "A framework for array shape reconstruction through mutual coupling," *IEEE Transactions on Microwave Theory and Techniques*, vol. 69, no. 10, pp. 4422–4436, 2021.

[57] A. C. Fikes, M. Gal-Katziri, O. S. Mizrahi, D. E. Williams, and A. Hajimiri, "Frontiers in flexible and shape-changing arrays," *IEEE Journal of Microwaves*, vol. 3, no. 1, pp. 349–367, 2023.

[58] J. A. Caripidis Troccola, M. Carvalho, M. R. Islam, and J. L. Volakis, "Deployable tightly coupled dipole reflectarray for small satellites," in *2022 IEEE International Symposium on Antennas and Propagation and USNC-URSI Radio Science Meeting (AP-S/URSI)*, 2022, pp. 163–164.

[59] M. Carvalho and J. L. Volakis, "Deployable rigid-flexible tightly coupled dipole array (rf-tcda)," *IEEE Open Journal of Antennas and Propagation*, vol. 2, pp. 1184–1193, 2021.

[60] T. Chen, O. R. Bilal, R. Lang, C. Daraio, and K. Shea, "Autonomous deployment of a solar panel using elastic origami and distributed shape-memory-polymer actuators," *Phys. Rev. Appl.*, vol. 11, p. 064069, Jun 2019. [Online]. Available: https://link.aps.org/doi/10.1103/PhysRevApplied.11.064069

[61] D. You, D. Awaji, A. Shirane, H. Sakamoto, and K. Okada, "A flexible element antenna for ka-band active phased array satcom transceiver," in *2020 IEEE Asia-Pacific Microwave Conference (APMC)*, 2020, pp. 991–993.

[62] X. Wang, D. You, X. Fu, H. Lee, Z. Li, D. Awaji, J. Pang, A. Shirane, H. Sakamoto, and K. Okada, "A flexible implementation of ka-band active phased array for satellite communication," in *2022 IEEE/MTT-S International Microwave Symposium - IMS 2022*, 2022, pp. 753–756.

[63] S.-E. Adami, P. Proynov, G. S. Hilton, G. Yang, C. Zhang, D. Zhu, Y. Li, S. P. Beeby, I. J. Craddock, and B. H. Stark, "A flexible 2.45-ghz power harvesting wristband with net system output from 24.3 dbm of rf power," *IEEE Transactions on Microwave Theory and Techniques*, vol. 66, no. 1, pp. 380–395, 2018.

[64] M. Wagih, G. S. Hilton, A. S. Weddell, and S. Beeby, "Broadband millimeter-wave textile-based flexible rectenna for wearable energy harvesting," *IEEE Transactions on Microwave Theory and Techniques*, vol. 68, no. 11, pp. 4960–4972, 2020.

[65] X. He and M. M. Tentzeris, "In-package additively manufactured sensors for bend prediction and calibration of flexible phased arrays and flexible hybrid electronics," in *2021 IEEE MTT-S International Microwave Symposium (IMS)*, 2021, pp. 327–330.

[66] K. Hu, G. Soto–Valle, Y. Cui, and M. M. Tentzeris, "Flexible and scalable additively manufactured tile-based phased arrays for satellite communication and 50 mm wave applications," in *2022 IEEE/MTT-S International Microwave Symposium - IMS 2022*, 2022, pp. 691–694.

[67] M. Gal-Katziri, A. Fikes, and A. Hajimiri, "Flexible active antenna arrays," *npj Flexible Electronics*, vol. 6, no. 1, p. 85, Oct 2022. [Online]. Available: https://doi.org/10.1038/s41528-022-00218-z

[68] S. Mano and T. Katagi, "A method for measuring amplitude and phase of each radiating element of a phased array antenna," *Electronics and Communications in Japan, Part I: Communications*, vol. 65, pp. 58–65, 1982.

[69] C. R. Chappidi and K. Sengupta, "A 26-42 GHz Broadband, Back-off Efficient and Vswr Tolerant CMOS Power Amplifier Architecture for 5G Applications," in *2019 Symposium on VLSI Circuits*, 2019, pp. C22–C23.

[70] K. Hausmair, S. Gustafsson, C. Sánchez-Pérez, P. N. Landin, U. Gustavsson, T. Eriksson, and C. Fager, "Prediction of Nonlinear Distortion in Wideband Active Antenna Arrays," *IEEE Transactions on Microwave Theory and Techniques*, vol. 65, no. 11, pp. 4550–4563, 2017.

[71] S. Hu, S. Kousai, and H. Wang, "A Compact Broadband Mixed-Signal Power Amplifier in Bulk CMOS With Hybrid Class-G and Dynamic Load Trajectory Manipulation," *IEEE Journal of Solid-State Circuits*, vol. 52, no. 6, pp. 1463–1478, 2017.

[72] S. Kousai, K. Onizuka, J. Wadatsumi, T. Yamaguchi, Y. Kuriyama, and M. Nagaoka, "Polar Antenna Impedance Detection and Tuning for Efficiency Improvement in a 3G/4G CMOS Power Amplifier," *IEEE Journal of Solid-State Circuits*, vol. 49, no. 12, pp. 2902–2914, 2014.

[73] N. S. Mannem, M.-Y. Huang, T.-Y. Huang, S. Li, and H. Wang, "24.2 A Reconfigurable Series/Parallel Quadrature-Coupler-Based Doherty PA in CMOS SOI with VSWR Resilient Linearity and Back-Off PAE for 5G MIMO Arrays," in *2020 IEEE International Solid- State Circuits Conference - (ISSCC)*, 2020, pp. 364–366.

[74] K. K. W. Low, G. M. Rebeiz, S. Zihir, and T. Kanar, "A Reconfigurable Dual-Polarized 1024-Element Ka-Band SATCOM Transmit Phased-Array with Large Scan Volume and +48 dBW EIRP," in *2021 IEEE MTT-S International Microwave Symposium (IMS)*, 2021, pp. 638–640.

[75] G. Gültepe and G. M. Rebeiz, "A 256-element dual-beam dual-polarization ku-band phased-array with 5 db/k g/t for simultaneous multi-satellite reception," in *2021 IEEE MTT-S International Microwave Symposium (IMS)*, 2021, pp. 629–631.

[76] S. Rasti Boroujeni, M. H. Mazaheri, S. Ituah, A. Wyrzykowska, S. Ziabakhsh, A. Palizban, G. Chen, A. El-Gouhary, K. Fereidani, M.-R. Nezhad-Ahmadi, and S. Safavi-Naeini, "A high-efficiency 27–30-ghz 130-nm bi-cmos transmitter front end for satcom phased arrays," *IEEE Transactions on Microwave Theory and Techniques*, vol. 69, no. 11, pp. 4977–4985, 2021.

[77] W. M. Abdel-Wahab, H. Al-Saedi, E. H. Mirza Alian, M. Raeis-Zadeh, A. Ehsandar, A. Palizban, N. Ghafarian, G. Chen, H. Gharaee, M. R. Nezhad-Ahmadi, and S. Safavi Naeini, "A modular architecture for wide scan angle phased array antenna

for k/ka mobile satcom," in *2019 IEEE MTT-S International Microwave Symposium (IMS)*, 2019, pp. 1076–1079.

[78] G. Gultepe, K. Low, Q. Ma, and G. M. Rebeiz, "A 1024-element k-band commercial satcom user terminal with a g/t of 10.2 db/k and two simultaneous beams," in *2022 IEEE International Symposium on Phased Array Systems Technology (PAST)*, 2022, pp. 01–04.

[79] O. Kazan, Z. Hu, A. Alhamed, and G. M. Rebeiz, "A 5-33 ghz 8-channel transmit beamformer with peak power of 14 dbm for x/ku/ka-band satcom applications," in *2022 IEEE International Symposium on Phased Array Systems Technology (PAST)*, 2022, pp. 1–4.

[80] K. K. W. Low, T. Kanar, S. Zihir, and G. M. Rebeiz, "A 17.7–20.2-ghz 1024-element k-band satcom phased-array receiver with 8.1-db/k g/t, ±70° beam scanning, and high transmit isolation," *IEEE Transactions on Microwave Theory and Techniques*, vol. 70, no. 3, pp. 1769–1778, 2022.

[81] K. K. W. Low, G. M. Rebeiz, S. Zihir, and T. Kanar, "A reconfigurable dual-polarized 1024-element ka-band satcom transmit phased-array with large scan volume and +48 dbw eirp," in *2021 IEEE MTT-S International Microwave Symposium (IMS)*, 2021, pp. 638–640.

[82] G. Gültepe, S. Zihir, T. Kanar, and G. M. Rebeiz, "A dual-polarized 1024-element ku-band satcom phased-array with embedded transmit filter and >10 db/k g/t," in *2021 IEEE MTT-S International Microwave Symposium (IMS)*, 2021, pp. 858–860.

[83] K. K. Wei Low, A. Nafe, S. Zihir, T. Kanar, and G. M. Rebeiz, "A scalable circularly-polarized 256-element ka-band phased-array satcom transmitter with ±60° beam scanning and 34.5 dbw eirp," in *2019 IEEE MTT-S International Microwave Symposium (IMS)*, 2019, pp. 1064–1067.

[84] B. Sadhu, A. Paidimarri, W. Lee, M. Yeck, C. Ozdag, Y. Tojo, J.-O. Plouchart, X. Gu, Y. Uemichi, S. Chakraborty, Y. Yamaguchi, N. Guan, and A. Valdes-Garcia, "A 24-to-30ghz 256-element dual-polarized 5g phased array with fast beam-switching support for >30,000 beams," in *2022 IEEE International Solid- State Circuits Conference (ISSCC)*, vol. 65, 2022, pp. 436–438.

[85] Y. Yin, B. Ustundag, K. Kibaroglu, M. Sayginer, and G. M. Rebeiz, "Wideband 23.5–29.5-ghz phased arrays for multistandard 5g applications and carrier aggrega-

tion," *IEEE Transactions on Microwave Theory and Techniques*, vol. 69, no. 1, pp. 235–247, 2021.

[86] J. Pang, Z. Li, X. Luo, J. Alvin, R. Saengchan, A. A. Fadila, K. Yanagisawa, Y. Zhang, Z. Chen, Z. Huang *et al.*, "A cmos dual-polarized phased-array beamformer utilizing cross-polarization leakage cancellation for 5g mimo systems," *IEEE Journal of Solid-State Circuits*, vol. 56, no. 4, pp. 1310–1326, 2021.

[87] K. Kibaroglu, M. Sayginer, T. Phelps, and G. M. Rebeiz, "A 64-element 28-ghz phased-array transceiver with 52-dbm eirp and 8–12-gb/s 5g link at 300 meters without any calibration," *IEEE Transactions on Microwave Theory and Techniques*, vol. 66, no. 12, pp. 5796–5811, 2018.

[88] X. Fu, Y. Wang, D. You, X. Wang, A. A. Fadila, Y. Zhang, S. Kato, C. Wang, Z. Li, J. Pang, A. Shirane, and K. Okada, "A 3.4mw/element radiation-hardened ka-band cmos phased-array receiver utilizing magnetic-tuning phase shifter for small satellite constellation," in *2022 IEEE International Solid- State Circuits Conference (ISSCC)*, vol. 65, 2022, pp. 90–92.

[89] X. Fu, D. You, X. Wang, M. Ide, Y. Zhang, J. Sakamaki, A. A. Fadila, Z. Li, Y. Wang, J. Sudo, M. Higaki, S. Inoue, T. Eishima, T. Tomura, J. Pang, H. Sakai, K. Okada, and A. Shirane, "A 2.95mw/element ka-band cmos phased-array receiver utilizing on-chip distributed radiation sensors in low-earth-orbit small satellite constellation," in *2023 IEEE International Solid- State Circuits Conference (ISSCC)*, 2023, pp. 18–20.

Appendix A

Publication List

A.1 Journal Papers

- **Dongwon You**, Xi Fu, Hans Herdian, Xiaolin Wang, Yasuto Narukiyo, Ashbir Avia Fadila, Hojun Lee, Michihiro Ide, Senna Kato, Zhengli, Yun Wang, Daisuke Awaji, Jian Pang, Hiraku Sakamoto, Kenichi Okada, and Atsushi Shirane, "A Ka-Band 64-element Deployable Active Phased-Array TX on a Flexible Hetero Segmented Liquid Crystal Polymer for Small-Satellites," in IEEE Microwave and Wireless Technology Letters, vol. 33, no. 6, pp. 903-906, June 2023.

- **Dongwon You**, Xiaolin Wang, Hans Herdian, Xi Fu, Hojun Lee, Michihiro Ide, Carrel da Gomez, Zheng Li, Jill Mayeda, Daisuke Awaji, Jian Pang, Hiraku Sakamoto, Kenichi Okada, and Atsushi Shirane "A Ka-Band 64-element Deployable Active Phased Array Transmitter on a Flexible Hetero Segmented Liquid Crystal Polymer for Small-Satellites," in IEEE Access, vol. 11, pp. 69522-69535, 2023.

- **Dongwon You**, Xi Fu, Xiaolin Wang, Yuan Gao, Wenqian Wang, Jun Sakamaki, Hans Herdian, Sena Kato, Michihiro Ide, Yuncheng Zhang, Ashbir Aviat Fadila, Zheng Li, Chun Wang, Yun Wang, Jumpei Sudo, Makoto Higaki, Nahoka Kawaguchi, Masaya Nitta, Soichiro Inoue, Takashi Eishima, Takashi Tomura, Jian ann, Hiroyuki Sakai, Kenichi Okada, and Atsushi Shirane, "A Small-Satellite-Mounted 256-Element Ka-Band CMOS Phased-Array Transmitter Achieving 63.8dBm EIRP Under 26.6W Power Consumption Using Single/Dual Circular Polarization Active Coupler," IEEE Journal of Solid-State Circuits (JSSC). (To be Submitted)

- **Dongwon You**, Yuta Takahashi, Shinji Takeda, Motoki Moritani, Haruki Hagiwara, Shuhei Koike, Hojun Lee, Yun Wang, Zheng Li, Jian Pang, Hiraku Sakamoto, Kenichi Okada, and Atsushi Shirane, "A Ka-Band 16-Element Deployable Active

Phased Array Transmitter for Satellite Communication," IEEE Transaction on Microwave Theory and Techniques (TMTT). (To be Submitted)

- **Dongwon You**, Xi Fu, Hans Herdian, Xiaolin Wang, Yasuto Narukiyo, Ashbir Avia Fadila, Hojun Lee, Michihiro Ide, Senna Kato, Zhengli, Yun Wang, Daisuke Awaji, Jian Pang, Hiraku Sakamoto, Kenichi Okada, and Atsushi Shirane, "A Ka-Band 64-element Deployable Active Phased-Array TX on a Flexible Hetero Segmented Liquid Crystal Polymer for Small-Satellites," IEEE Transaction on Microwave Theory and Techniques (TMTT). (To be submitted)

A.2 International Conferences and Workshops

- **Dongwon You**, Xi Fu, Xiaolin Wang, Yuan Gao, Wenqian Wang, Jun Sakamaki, Hans Herdian, Sena Kato, Michihiro Ide, Yuncheng Zhang, Ashbir Aviat Fadila, Zheng Li, Chun Wang, Yun Wang, Jumpei Sudo, Makoto Higaki, Nahoka Kawaguchi, Masaya Nitta, Soichiro Inoue, Takashi Eishima, Takashi Tomura, Jian ann, Hiroyuki Sakai, Kenichi Okada, and Atsushi Shirane, "A Small-Satellite-Mounted 256-Element Ka-Band CMOS Phased-Array Transmitter Achieving 63.8dBm EIRP Under 26.6W Power Consumption Using Single/Dual Circular Polarization Active Coupler," 2023 IEEE International Solid-State Circuits Conference (ISSCC), San Francisco, CA, Feb. 2023.

- **Dongwon You**, Yun Wang, Xi Fu, Hans Herdian, Xiaolin Wang, Ashbir Fadila, Hojun Lee, Michihiro Ide, Sena Kato, Zheng Li, Jian Pang, Atsushi Shirane, and Kenichi Okada, "A Ka-Band Dual Circularly Polarized CMOS Transmitter with Adaptive Scan Impedance Tuner and Active XPD Calibration Technique for Satellite Terminal," 2022 IEEE Radio Frequency Integrated Circuits Symposium (RFIC), 2022.

- **Dongwon You**, Yuta Takahashi, Shinji Takeda, Motoki Moritani, Haruki Hagiwara, Shuhei Koike, Hojun Lee, Yun Wang, Zheng Li, Jian Pang, Hiraku Sakamoto, Atsushi Shirane, and Kenichi Okada, "A Ka-Band 16-Element Deployable Active Phased Array Transmitter for Satellite Communication," 2021 IEEE MTT-S International Microwave Symposium (IMS), 2021.

- **Dongwon You**, Daisuke Awaji, Atsushi Shirane, Hiraku Sakamoto, and Kenichi Okada, "A Flexible Element Antenna for Ka-Band Active Phased Array SATCOM Transceiver," 2020 IEEE Asia-Pacific Microwave Conference (APMC), 2020

A.3 Domestic Conferences and Workshops

- **Dongwon You**, Yuta Takahashi, Shinji Takeda, Motoki Moritani, Haruki Hagiwara, Shuhei Koike, Hojun Lee, Yun Wang, Zheng Li, Jian Pang, Atsushi Shirane, Hiraku Sakamoto and Kenichi Okada, "A Ka-Band 16-Element Deployable Active Phased Array Transmitter for Satellite Communication," 2022 Large Scale Integration System Workshop, 2022.

- **Dongwon You**, Yun Wang, Xi Fu, Atsushi Shirane, and Kenichi Okada, "A Ka-Band Dual Circularly Polarized CMOS Transmitter Enabled with Adaptive Impedance Tuner and Cross Polarization Calibration for Satellite Terminal," 2022 Institute of Electronics, Information and Communication Engineers Conference Archives (IEICE Conference Archives), 2022.

- **Dongwon You**, Yun Wang, Atsushi Shirane, and Kenichi Okada, "A Ka-Band Intermodulation-Interference-Tolerant Receiver Design for Earth Station in Satellite Communication," 2019 Institute of Electronics, Information and Communication Engineers Conference Archives (IEICE Conference Archives), 2019.

A.4 Co-Author

A.4.1 Journals and Letters

- Zheng Li, Jian Pang, Yi Zhang, Yudai Yamazaki, Qiaoyu Wang, Peng Luo, Weichu Chen, Yijing Liao, Minzhe Tang, Yun Wang, Xi Fu, **Dongwon You**, Naoki Oshima, Shinichi Hori, Jeehoon Park, Kazuaki Kunihiro, Atsushi Shirane, Kenichi Okada, "A 39-GHz CMOS Bidirectional Doherty Phased- Array Beamformer Using Shared-LUT DPD With Inter-Element Mismatch Compensation Technique for 5G Base Station," in IEEE Journal of Solid-State Circuits, vol. 58, no. 4, pp. 901-914, April 2023.

- Michihiro Ide, Atsushi Shirane, Kiyoshi Yanagisawa, **Dongwon You**, Jian Pang, Kenichi Okada, "A 28-GHz Phased-Array Relay Transceiver for 5G Network Using Vector-Summing Backscatter with 24-GHz Wireless Power and LO Transfer," in IEEE Journal of Solid-State Circuits, vol. 57, no. 4, pp. 1211-1223, April 2022.

- Yun Wang, **Dongwon You**, Xi Fu, Takeshi Nakamura, Ashbir Aviat Fadila, Teruki Someya, Atsuhiro Kawaguchi, Junjun Qiu, Jian Pang, Kiyoshi Yanagisawa, Bangan Liu, Yuncheng Zhang, Haosheng Zhang, Rui Wu, Shunichiro Masaki, Daisuke

Yamazaki, Atsushi Shirane, Kenichi Okada, "A Ka-Band SATCOM Transceiver in 65-nm CMOS With High-Linearity TX and Dual-Channel Wide-Dynamic-Range RX for Terrestrial Terminal," in IEEE Journal of Solid-State Circuits, vol. 57, no. 2, pp. 356-370, Feb. 2022.

- Jian Pang, Zheng Li, Xueting Luo, Joshua Alvin, Rattanan Saengchan, Ashbir Aviat Fadila, Kiyoshi Yanagisawa, Yi Zhang, Zixin Chen, Zhongliang Huang, Xiaofan Gu, Rui Wu, Yun Wang, **Dongwon You**, Bangan Liu, Zheng Sun, Yuncheng Zhang, Hongye Huang, Naoki Oshima, Keiichi Motoi, Shinichi Hori, Kazuaki Kunihiro, Tomoya Kaneko, Atsushi Shirane, Kenichi Okada, "A CMOS Dual-Polarized Phased-Array Beamformer Utilizing Cross-Polarization Leakage Cancellation for 5G MIMO Systems," in IEEE Journal of Solid-State Circuits, vol. 56, no. 4, pp. 1310-1326, April 2021.

- Yun Wang, Rui Wu, Jian Pang, **Dongwon You**, Ashbir Aviat Fadila, Rattanan Saengchan, Xi Fu, Daiki Matsumoto, Takeshi Nakamura, Ryo Kubozoe, Masaru Kawabuchi, Bangan Liu, Haosheng Zhang, Junjun Qiu, Hanli Liu, Naoki Oshima, Keiichi Motoi, Shinichi Hori, Kazuaki Kunihiro, Tomoya Kaneko, Atsushi Shirane, Kenichi Okada, "A 39-GHz 64-Element Phased-Array Transceiver with Built-In Phase and Amplitude Calibrations for Large-Array 5G NR in 65-nm CMOS," in IEEE Journal of Solid-State Circuits, vol. 55, no. 5, pp. 1249-1269, May 2020.

- Jian Pang, Zheng Li, Ryo Kubozoe, Xueting Luo, Rui Wu, Yun Wang, **Dongwon You**, Ashbir Aviat Fadila, Rattanan Saengchan, Takeshi Nakamura, Joshua Alvin, Daiki Matsumoto, Bangan Liu, Aravind Tharayil Narayanan, Junjun Qiu, Hanli Liu, Zheng Sun, Hongye Huang, Korkut Kaan Tokgoz, Keiichi Motoi, Naoki Oshima, Shinichi Hori, Kazuaki Kunihiro, Tomoya Kaneko, Atsushi Shirane, Kenichi Okada, "A 28-GHz CMOS Phased-Array Beamformer Utilizing Neutralized Bi-Directional Technique Supporting Dual-Polarized MIMO for 5G NR," in IEEE Journal of Solid-State Circuits, vol. 55, no. 9, pp. 2371-2386, Sept. 2020.

A.4.2 Conferences

- Xi Fu, **Dongwon You**, Xiaolin Wang, Michihiro Ide, Yuncheng Zhang, Jun Sakamaki, Ashibir Aviat Fadila, Zheng Li, Yun Wang, Jumpei Sudo, Makoto Higaki, Soichiro Inoue, Takashi Eishima, Takashi Tomura, Jian Pang, Hiroyuki Sakai, Kenichi Okada, Atsushi Shirane, "A 2.95mW/element Ka-Band CMOS Phased-Array Receiver Utilizing On-Chip Distribution Radiation Sensors in Low-Earth-Orbit Small

Satellite Constellation," IEEE International Solid-State Circuits Conference (ISSCC), San Francisco, CA, Feb. 2023

- Xi Fu, Yun Wang, **Dongwon You**, Xiaolin Wang, Ashbir Aviat Fadila, Yi Zhang, Sena Kato, Chun Wang, Zheng Li, Jian Pang, Atsushi Shirane, Kenichi Okada, "A 3.4mW/element Radiation-Hardened Ka-Band CMOS Phased-Array Receiver Utilizing Magnetic-Tuning Phase Shifter for Small Satellite Constellation," IEEE International Solid-State Circuits Conference (ISSCC), San Francisco, CA, Feb. 2022

- Xiaolin Wang, **Dongwon You**, Xi Fu, Hojun Lee, Zheng Li, Daisuke Awaji, Jian Pang, Atsushi Shirane, Hiraku Sakamoto, and Kenichi Okada, "A Flexible Implementation of Ka-Band Active Phased Array for Satellite Communication," 2022 IEEE/MTT-S International Microwave Symposium (IMS), Denver, CO, USA, 2022.

- Zheng Li, Jian Pang, Yi Zhang, Yudai Yamazaki, Qiaoyu Wang, Peng Luo, Weichu Chen, Yijing Liao, Minzhe Tang, Xi Fu, **Dongwon You**, Naoki Oshima, Shinichi Hori, Kazuaki Kunihiro, Atsushi Shirane, Kenichi Okada, "A 39-GHz CMOS Bi-Directional Doherty Phased-Array Beamformer Using Shared-LUT DPD with Inter-Element Mismatch Compensation Technique for 5G Base-Station," 2022 IEEE Symposium on VLSI Technology and Circuits (VLSI Technology and Circuits), Honolulu, HI, USA, 2022

- Michihiro Ide, Yuasa Keito, Kato Sena, **Dongwon You**, Ashbir Aviat Fadila, Jian Pang, Atsushi Shirane, Kenichi Okada, "A 28-GHz Phased-Array Relay Transceiver for 5G Network Using Vector-Summing Backscatter with 24-GHz Wireless Power and LO Transfer," 2021 Symposium on VLSI Circuits, 2021.

- Jian Pang, Zheng Li, Xueting Luo, Joshua Alvin, Kiyoshi Yanagisawa, Yi Zhang, Zixin Chen, Zhongliang Huang, Xiaofan Gu, Weichu Chen, Yun Wang, **Dongwon You**, Zheng Sun, Yuncheng Zhang, Hongye Huang, Naoki Oshima, Kenichi Motoi, Shinichi Hori, Kazuaki Kunihiro, Tomoya Kaneko, Atsushi Shirane, Kenichi Okada, "A Fast-Beam-Switching 28-GHz Phased-Array Transceiver Supporting Cross-Polarization Leakage Self-Cancellation," 2021 Symposium on VLSI Circuits (VLSI), 2021.

- Yun Wang, **Dongwon You**, Xi Fu, Takeshi Nakamura, Ashbir Aviat Fadila, Teruki Someya, Atsuhiro Kawaguchi, Jian Pang, Kiyoshi Yanagisawa, Bangan Liu, Yuncheng Zhang, Haosheng Zhang, Rui Wu, Atsushi Shirane, Shunichiro Masaki, Daisuke

Yamazaki, Kenichi Okada, "A CMOS Ka-Band SATCOM Transceiver with ACI-Cancellation Enhanced Dual-Channel Low-NF Wide-Dynamic-Range RX and High-Linearity TX," 2020 IEEE Radio Frequency Integrated Circuits Symposium (RFIC), 2020.

- Jian Pang, Zheng Li, Xueting Luo, Joshua Alvin, Rattanan Saengchan, Ashbir Aviat Fadila, Kiyoshi Yanagisawa, Yi Zhang, Zixin Chen, Zhongliang Huang, Xiaofan Gu, Rui Wu, Yun Wang, **Dongwon You**, Bangan Liu, Zheng Sun, Yucheng Zhang, Hongye Huang, Naoki Oshima, Keiichi Motoi, Shinichi Hori, Kazuaki Kunihiro, Tomoya Kaneko, Atsushi Shirane, Kenichi Okada, "A 28-GHz CMOS Phased-Array Beamformer Supporting Dual-Polarized MIMO with Cross-Polarization Leakage Cancellation," 2020 IEEE Symposium on VLSI Circuits (VLSI), 2020.

- Zheng Li, Jian Pang, Ryo Kubozoe, Xueting Luo, Rui Wu, Yun Wang, **Dongwon You**, Ashbir Aviat Fadila, Joshua Alvin, Bangan Liu, Zheng Sun, Hongye Huang, Atsushi Shirane, Kenichi Okada, "A 28GHz CMOS Differential Bi-Directional Amplifier for 5G NR," 2020 25th Asia and South Pacific Design Automation Conference (ASP-DAC), 2020.

- Jian Pang, Zheng Li, Ryo Kubozoe, Xueting Luo, Rui Wu, Yun Wang, **Dongwon You**, Ashbir Aviat Fadila, Rattanan Saengchan, Takeshi Nakamura, Joshua Alvin, Daiki Matsumoto, Aravind Tharayil Narayanan, Bangan Liu, Junjun Qiu, Hanli Liu, Zheng Sun, Hongye Huang, Korkut Kaan Tokgoz, Keiichi Motoi, Naoki Oshima, Shinichi Hori, Kazuaki Kunihiro, Tomoya Kaneko, Atsushi Shirane, Kenichi Okada, "21.1 A 28GHz CMOS Phased-Array Beamformer Utilizing Neutralized Bi-Directional Technique Supporting Dual-Polarized MIMO for 5G NR," 2019 IEEE International Solid-State Circuits Conference - (ISSCC), 2019.

- Yun Wang, Rui Wu, Jian Pang, **Dongwon You**, Ashbir Aviat Fadila, Rattanan Saengchan, Xi Fu, Daiki Matsumoto, Takeshi Nakamura, Ryo Kubozoe, Masaru Kawabuchi, Bangan Liu, Haosheng Zhang, Junjun Qiu, Hanli Liu, Wei Deng, Naoki Oshima, Keiichi Motoi, Shinichi Hori, Kazuaki Kunihiro, Tomoya Kaneko, Atsushi Shirane, Kenichi Okada, "A 39GHz 64-Element Phased-Array CMOS Transceiver with Built-in Calibration for Large-Array 5G NR," 2019 IEEE Radio Frequency Integrated Circuits Symposium (RFIC), 2019.

- Yun Wang, **Dongwon You**, Xi Fu, Takeshi Nakamura, Ashbir Aviat Fadila, Teruki Someya, Atsuhiro Kawaguchi, Atsushi Shirane, Kenichi Okada, "An Adjacent-Channel-Interference Tolerant Receiver for Ka-Band Satellite Communication," 2020

Institute of Electronics, Information and Communication Engineers Conference Archives (IEICE Conference Archives), 2020.

- Yun Wang, **Dongwon You**, Rattanan Saengchan, Atsushi Shirane, Kenichi Okada, "A 39 GHz CMOS Phased-Array Transmitter for 5G NR with LOFT Auto-Cancellation," 2019 Institute of Electronics, Information and Communication Engineers Conference Archives (IEICE Conference Archives), Osaka, Japan, 2019.

- Rattanan Saengchan, Jian Pang, **Dongwon You**, Fadila Ashbir Aviat, Joshua Alvin, and Rui Wu, "A High-Accuracy Calibration Circuit for Large-Sized 5G Phased-Array Transceiver," 2019 Institute of Electronics, Information and Communication Engineers Conference Archives (IEICE Conference Archives), Osaka, Japan, 2019.

- Jian Pang, Zheng Li, Ryo Kubozoe, Xueting Luo, Rui Wu, Yun Wang, **Dongwon You**, Ashbir Aviat Fadila, Rattanan Saengchan, Takeshi Nakamura, Joshua Alvin, Daiki Matsumoto, Aravind Tharayil Narayanan, Bangan Liu, Junjun Qiu, Hanli Liu, Zheng Sun, Hongye Huang, Atsushi Shirane, Kenichi Okada, "A 28GHz CMOS Bi-Directional Phased-Array Beamformer for 5G NR Supporting Dual-Polarized MIMO," 2019 Institute of Electronics, Information and Communication Engineers Conference Technical Report (IEICE Tech. Rep.), Osaka, Japan, 2019.